Department of Electrical and Computer Engineering

A Novel Digital Image Processing Technique to Detect Power Transformers Internal Faults using Frequency Response Analysis Polar Plot Signature

Omar Maqbul Aljohani

This thesis is presented for the Degree of
Doctor of Philosophy
of
Curtin University

February 2017

Declaration

To the best of my knowledge and belief this thesis contains no material previously published by any other person except where due acknowledgment has been made. This thesis contains no material which has been accepted for the award of any other degree or diploma in any university.

Omar Maqbul ALJOHANI
Signature:

Date:
16/02/2017

ABSTRACT

The power transformer is a significant asset in any electrical power transmission and distribution network. A reliable condition monitoring scheme must therefore be adopted to avoid any catastrophic failure to this asset. This is especially true because the global fleet of power transformers commenced service more than three decades ago and, due to their age, are now more prone to imminent failure.

One of the most critical types of failure within the power transformer is a mechanical fault. This can be prevented by applying a proper condition monitoring technique. Frequency Response Analysis (FRA) is one such technique and is widely accepted as the most reliable method for detecting transformer mechanical deformation. However, although the FRA measurement technique is well developed, interpretation of the FRA signature remains a challenge. This is because there is not yet a widely accepted and published interpretation standard, and a highly specialised person must be brought in to carry out the interpretation. This can lead to inconsistency in interpretation, because the same FRA signature can be interpreted differently by different experts. Furthermore, the current FRA technique is not able to detect incipient and minor winding deformation. This is another major drawback of using the FRA technique, because mechanical deformation is highly progressive in nature and a problem can quickly become serious without exhibiting any warning.

This research introduces a new application, which aims to improve the current approach to interpretation of the FRA signature. In contrast to current FRA practice — which relies mainly on the magnitude of the measured FRA signature, paying little attention to the measured phase angle — the newly proposed application integrates both magnitude and phase angle into one polar plot that encompasses most characteristics of the measured response signal. Various Digital Image Processing (DIP) techniques are implemented to enhance detection accuracy of incipient mechanical faults, and to automate and standardise the FRA interpretation.

Dedication

To the loving memory of my father, Maqbul Rashed Aljohani
To my source of tenderness in life, my mother, Nora Juber Aljohani
To my love forever, my wife, Hanouf Abdullah Alghamdi
To the wonderful future, my sons, Nawaf and Abdulelah
To the pretty flowers of my life, my daughters, Loujain and Sadeem
With eternal love and appreciation, I am honoured to dedicate this work to you

Acknowledgements

Praise be to almighty Allah and his bounty in completion of this thesis. I am truly grateful to the many people who have supported me during my PhD journey. First and foremost, I would like to express my sincere thanks to the soul of this project, my supervisor, Associate Professor. A. Abu-Siada, for his unlimited support, extensive encouragement, and continuous motivation. He has offered consistent and positive guidance, as well as invaluable recommendations, all of which have helped to solve many difficulties throughout my PhD. I must also thank my thesis committee members, Professors. S. Islam and M. Masoum, for their significant role in the promotion of this thesis. But my most heartfelt gratitude goes to my lovely family, as well as to my brothers, Abdullah, Mohammed and Abdulrahman, and my sisters, Aisha, Maha, Amal, Khadija and Manal, for their prayers, encouragement and favours.

LIST OF PUBLICATION

[1] **O. Aljohani** and A. Abu-Siada, "Application of Digital Image Processing to Detect Short-Circuit Turns in Power Transformers Using Frequency Response Analysis," IEEE Transactions on Industrial Informatics, vol. 12, pp. 2062-2073, 2016.

[2] **O. Aljohani** and A. Abu-Siada, "Application of DIP to Detect Power Transformers Axial Displacement and Disk Space Variation using FRA Polar Plot Signature," IEEE Transactions on Industrial Informatics, vol. 20, pp. 1120-1129, 2016.

[3] **O. Aljohani** and A. Abu-Siada, "Application of Digital Image Processing to Detect Transformer Bushing Faults and Oil Degradation using FRA Polar Plot Signature," IEEE Transactions on Dielectrics and Electrical Insulation, vol. 24, Issue 1, pp. 428-436, February 2017.

[4] **O. Aljohani** and A. Abu-Siada, "New Intelligent Monitoring Technique to Detect Incipient Transformer Radial Deformation," IEEE Transactions on Power Delivery, 2017 (under review).

[5] **O. Aljohani** and A. Abu-Siada, "Identification of the minimum detection of transformer bushing failure based on Frequency Response Analysis (FRA)," IEEE 2nd Annual Southern Power Electronics Conference (SPEC), Auckland, NZ, 2016.

[6] **O. Aljohani**, A. Abu-Siada and Shengtao Li, "High Frequency Power Transformer Modelling for Frequency Response Analysis Studies", the International Conference on Condition Monitoring and Diagnosis (CMD2016) , Xi'an, China, 2016.

[7] **O. Aljohani** and A. Abu-Siada, "Minimum detection of power transformer short circuit fault using frequency response analysis," Australasian Universities Power Engineering Conference (AUPEC), Wollongong, Australia, 2015.

[8] **O. Aljohani**, A. Abu-Siada, and S. Islam, "Impact of insulating oil degradation on the power transformer frequency response analysis," IEEE 11th International Conference on the Properties and Applications of Dielectric Materials (ICPADM), pp. 396-399, Sydney, Australia, 2015.

[9] **O. Aljohani** and A. Abu-Siada, "Impact of Insulating Mineral Oil Degradation on the Power Transformer Frequency Response Analysis", the International Conference on the Properties and Applications of Dielectric Materials, Sydney, Australia, 2015

[10] **O. Aljohani** and A. Abu-Siada, "Impact of Power Transformer Insulating Mineral Oil Degradation on FRA Polar Plot" the 24th IEEE International Symposium on Industrial Electronics, Bouzios, Rio De Janeiro, Brazil, 2015.

[11] **O. Aljohani**, A. Abu-Siada and S. Islam, "Impact of Insulating Oil Degradation on Power Transformer Frequency Response Analysis", Asia-Pacific World Congress on Engineering, Plantation Island, Fiji, 2015.

[12] **O. Aljohani** and A. Abu-Siada and S. Islam, "Application of Digital Image Processing to Diagnose Various Winding Deformations Within Power Transformers Using FRA Polar Plot", the International Conference on Condition Monitoring and Diagnosis (CMD2014), Jeju, Korea, 2014.

[13] **O. Aljohani** and A. Abu-Siada, "Application of FRA polar plot technique to diagnose internal faults in power transformers," IEEE PES General Meeting, Washington, USA, 2014.

TABLE OF CONTENTS

LIST OF FIGURES

LIST OF TABLES

LIST OF ACRONYMS

AC	Alternative Current
AD	Axial Displacement
ASLE	Absolute Sum of Logarithmic Error
CBD	City-Block Distance
CC	Correlation Coefficient
CEGB	Central Electricity Generating Board
C_{HL}	Capacitance between HV and LV Windings
CIGRE	International Council on Large Electric System Association
CMD	Condition Monitoring and Diagnosis
C_o	Capacitance of Insulation between HV/LV and Tank/Core
C_{SH}	Capacitance of Winding Insulation
DGA	Dissolved Gas Analysis
DIP	Digital Image Processing
DSV	Disc space variation
EMF	Electromagnetic forces
ER	Electrical Representation
FEA	Finite Element Analysis
FRA	Frequency Response Analysis
GD	Geometric Dimensions
GEC	General Electric Company
G_{HL}	Conductance between HV and LV Windings
G_o	Conductance of Insulation between HV/LV and Tank/Core
G_{SH}	Conductance of Winding Insulation
HPT	Hot Spot Temperature
HV	High Voltage
IEC	International Electro-Technical Commission
IED	Image Euclidean Distance
IEEE	Institute of Electrical and Electronics Engineers
IM	Invariant Moment
LPT	Large Power Transformer
L_s	Inductance of Winding
LV	Low Voltage

M	Mutual Inductance
MTL	Multi-conductor Transmission Line
NR	Numerical Representation
NLTC	No-Load Tap Changer
OLTC	On-Load Tap Changer
PD	Partial Discharge
PDC	Polarization and Depolarization Current
RD	Radial Deformation
RLC	Resistance, Inductance and Capacitance
RMS	Root Mean Square
R_s	Resistance of Winding
SD	Standard Deviation
SC	Short Circuit
TA	Texture Analysis
TF	Transfer Function
UHF	Ultra-High Frequency

Chapter 1 Introduction

1:1 Background

Power transformers are indispensable to the electrical power system. Therefore, the health condition of these assets is a major concern to electricity utilities worldwide. Statistical studies reveal that the vast majority of the power transformer fleet commenced service before 1980, and many have already exceeded service life expectancy [1, 2]. Additional stress has been placed on the in-service power transformers by an increased demand for load power, particularly from developed and industrialised countries, and also by an increasing demand for nonlinear loads, such as electrical vehicles and power converters. Combined with the age of the transformers, these stresses mean the likelihood of transformer failure grows, subsequently leading to degradation of the transformer insulation system, loosening of the transformer winding clamping pressure, and a diminished capacity to withstand short circuit forces.

A survey conducted by KEMA [3], over a 13-year period between 1996 and 2008, examines the ability of 102 transformers to withstand Short Circuit (SC) forces. As illustrated in Figure 1-1, data analysis shows that around 30% of the collected samples are not able to resist the stresses of SC current [3]. Further studies show that SC faults are the most common reason for transformer failure [4].

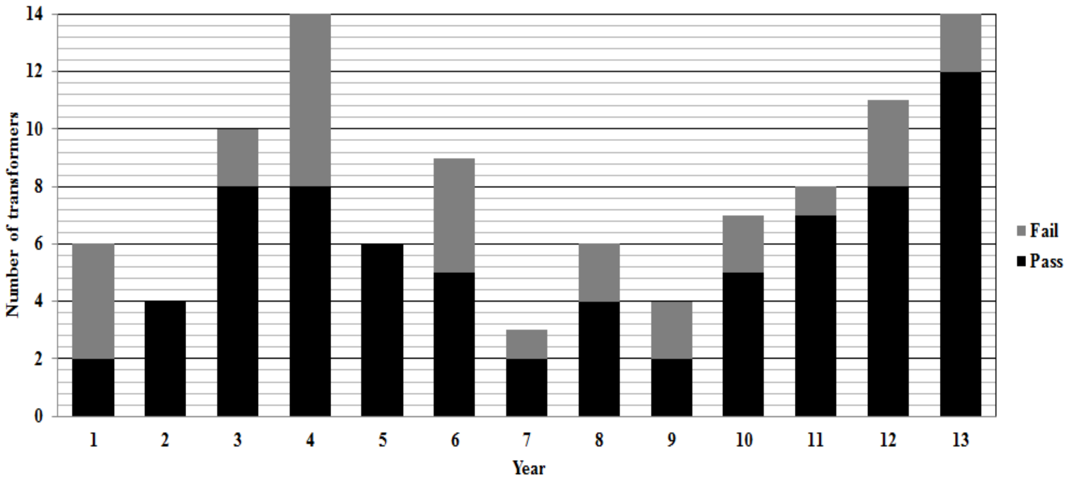

Figure 1-1 The 13-year survey of transformers' ability to withstand SC faults [3]

Transformer mechanical failure may occur as a result of SC faults, careless transportation, earthquakes, lightning or heavy rains [5].

As the majority of mechanical faults are of a progressive nature, it is important for a failure to be detected at an early stage for the purpose of corrective action [6, 7]. If not attended to, minor deformations may develop rapidly with catastrophic consequences [5]. Transformer failure can not only cause service interruption, but may also result in disastrous consequences such as devastating fires, serious injuries (including death), subversive activities, and high expense. A reliable, sensitive and economic diagnostic technique is therefore required to continuously monitor transformer health condition and allow timely and proper maintenance to be conducted (if required).

Although several Condition Monitoring and Diagnosis (CMD) techniques have recently been developed and accepted by the industry to inspect various chemical, electrical, thermal and mechanical failures in power transformers, FRA is still recognised as the most reliable tool to diagnose mechanical deformation [8].

The FRA technique was first studied by Dick and Erven during the 1970s, while the inaugural publication concerning the use of this technique for detecting transformer mechanical deformation was released in 1975 [9]. As a result, the UK's Central Electricity Generating Board (CEGB) accepted the FRA technique for application on transmission power transformers in 1980 [10]. From 1988 onwards, the FRA technique and its equipment were well-described, resulting in an enormous amount of publications and professional studies that discuss the impact of various mechanical faults on the FRA response.

The FRA technique is an offline test conducted by taking the investigated transformer out-of-service and then applying a sweep frequency AC voltage of low amplitude to one terminal of a transformer winding. The response signal is then measured across the other terminal of the same winding with reference to the earthed tank [11]. The measured FRA signature can be plotted in the form of winding impedance, admittance, or transfer function (V_{output}/V_{input} in dB) as a function of a wide frequency range (typically between 10 Hz and 2 MHz). The main concept of the FRA technique depends on a comparative analysis between the measured FRA signature and the reference (fingerprint) signature to identify any variation. A variation between the FRA signatures of the same transformer winding indicates unusual winding deformation.

As FRA results rely on graphical analysis, interpretation of the FRA signature is a highly specialised area. Researchers are motivated to investigate the impact of various mechanical windings deformations on the FRA signature in order to establish a reliable code for fault identification and quantification. This is also because incipient mechanical faults are hard to detect using the current analysis approach of the FRA technique.

The majority of studies to date on this subject are conducted using simulation analysis, which mimics the transformer’s real operation [12]. Several mechanical deformation failures such as axial displacement [13, 14], radial deformation [15, 16] and disk space variation [17] are discussed in the literature. However, there is little to no discussion regarding the need to establish a reliable application in order to automate and standardise the FRA interpretation process. Minor mechanical fault levels are not investigated in most studies published in the literature, due to the inability of the current FRA approach to detect such minor faults [18-21].

This research aims to develop a reliable, automated, rapid and economic tool that is based on advanced technologies including Digital Image Processing (DIP) techniques. The newly developed application will automatically identify and quantify an existing fault, even in its early stages (at minor levels), as well as determine its location.

The FRA technique is generally adopted to detect transformer mechanical failures. Few studies report that the FRA signature is also affected by other non-mechanical faults, such as insulation system degradation and bushing faults [22-24]. The newly developed application in this research shows that not all variations between two FRA signatures are linked to mechanical faults, but can also be related to bushing faults or a degradation of the transformer insulation system. In fact, the statistics show that a high percentage of transformer failures are attributed to transformer bushings and the insulation system [25-27]. To correctly understand the impact of transformer bushing defects and oil insulation degradation on the transformer FRA signature further investigation should be carried out.

1:2 Thesis Objectives

This thesis aims to improve the current interpretative approach for the power transformer's FRA technique. The substantial objectives of the thesis are listed below:

- Utilise a computer-based technique to accurately simulate a 3D Finite Element Analysis (FEA) transformer model in order to mimic the real operation of the power transformer under various conditions
- Implement mathematical and numerical approaches to model power transformer for FRA studies
- Develop a new approach for representing the power transformer's FRA signature by combining magnitude and phase angle responses into one polar plot
- Improve detection accuracy of the FRA interpretation process, using DIP techniques to automatically identify and quantify failures if they exist
- Investigate the accuracy of the proposed approach, when detecting minor mechanical deformations, through extensive simulation analyses and experimental measurements
- Investigate the impact of non-mechanical failures such as transformer bushing defects and oil insulation degradation on the proposed signature

1:3 Significance

This thesis introduces a different approach to FRA interpretation, so that both mechanical and non-mechanical failures of the power transformer can be detected automatically. The proposed approach will determine fault type, identify fault location, and also quantify incipient fault levels. This thesis aims to overcome the many drawbacks of the current interpretation process of the FRA technique, which have not yet been addressed in the literature. The new application applies DIP techniques to a FRA response signal, based on an amalgamation of measured magnitude and phase angle signatures (polar plots). The new application is easy to build within any commercial frequency response analyser and, as detailed in this thesis, characterised by its reliability, accuracy, simplicity and speed.

1:4 Thesis Outline

Chapter 1 presents the general background, main objectives and significance of the chosen thesis topic.

Chapter 2 presents a general review of various CMD techniques, including their pros and cons.

Chapter 3 describes the various causes and different types of mechanical faults within power transformers. Details of FRA measurements and interpretation techniques are also presented.

Chapter 4 demonstrates the methodologies available for modelling, simulating and representing the high-frequency power transformer for the purpose of FRA studies. The FEA technique for simulating power transformers is described. Details of two methods electrical circuit and numerical representation are also demonstrated.

Chapter 5 investigates the impact of several mechanical and non-mechanical faults on the current FRA technique for the transformers under study. A better understanding is reached regarding each fault’s impact on the current approach, and the inability of the current technique to detect minor mechanical deformation is demonstrated.

Chapter 6 presents the newly proposed signature and the utilisation of DIP techniques to automate and standardise the FRA interpretation process. All case studies in Chapter 5, which used the current FRA practice, are re-examined to demonstrate the superiority of the newly proposed automated technique over the current approach. This chapter also looks at the feasibility of the newly proposed application, based on a number of experimental measurements.

Chapter 7 provides the conclusion of this thesis alongside recommended future research directions that may be considered to extend work on the newly proposed application.

Chapter 2 Power Transformer Condition Monitoring and Diagnosis Techniques

2:1 Introduction

The overall condition of the power transformer governs the integrity of the whole electricity chain. In order to maintain transformer reliability during its expected operational life, there have been several studies dedicated to a better understanding of power transformer behaviour during various operating and health conditions. Various CMD techniques have been developed as part of these studies, which cannot detect any incipient fault as early as it emerges. Careless attendance to minor fault levels can lead to future catastrophic consequences, but an adopted CMD technique can precisely identify the failure type, level and also its location, allowing timely remedial action to be taken and hence avoiding any further consequences. Power transformer catastrophic failures will not only cause extended outages, but may lead to costly repairs, potentially serious injury, fire and/or fatality. Construction of the power transformer relies on several components, including the core, windings, insulation system and tank. Transformer components should be carefully studied to understand the real reaction of these elements during both healthy and faulty circumstances. This would facilitate the selection of a proper CMD technique and help developers improve current techniques.

2:2 Transformer Components

The main components of a power transformer (as shown in Figure 2-1) are illustrated in Figure 2-2 and briefly stated below.

- **Active parts**: are the laminated core, and the coaxial low voltage and high voltage windings. The active parts should be designed to withstand high electromagnetic stresses to avoid unexpected failure.
- **Insulation system**: is made up of solid elements (cellulose) and liquid insulation (transformer oil). Oil is substituted for air and cast resin in a dry-type transformer. Solid insulation, such as paper or pressboard, is predominantly used to isolate transformer windings, and the liquid insulation (commonly mineral oil) is used as a dielectric and cooling agent.
- **Accessories:** include:
    - **Electrical bushing** — an important insulation component in the power transformer, structured to allow an electrical conductor to pass (via a central insulated duct) through the main transformer tank.
    - **Tap changer** — a dynamic component within the transformer, used to regulate the voltage at the required level by adding or subtracting winding turns.
    - **Cooling system** — consists of fans, oil pumps and water-cooled heat exchangers, designed to reduce the high temperatures caused through operation and energy loss.
    - **Transformer tank** — made out of metal to protect the transformer's active parts and insulation system, and also to support the transformer's accessories and control panels. The transformer tank should withstand surrounding environment stresses, such as severe rain, humidity, wind and heat.

- **Transformer mechanical structures** — includes clamping, coil blocking and lead support, maintaining the transformer’s active parts firm against any mechanical stresses.

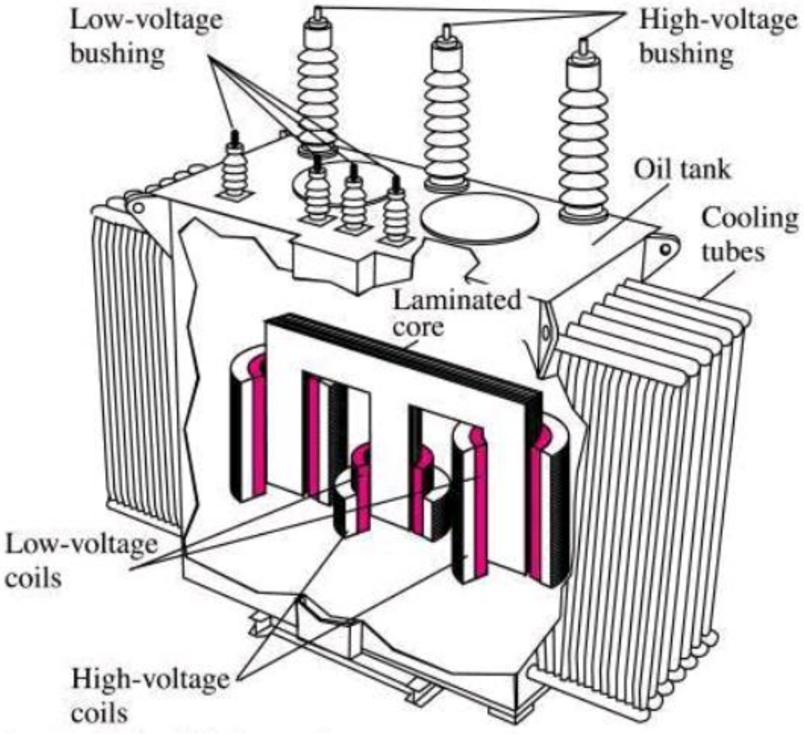

Figure 2-1 Schematic diagram of transformer components [28]

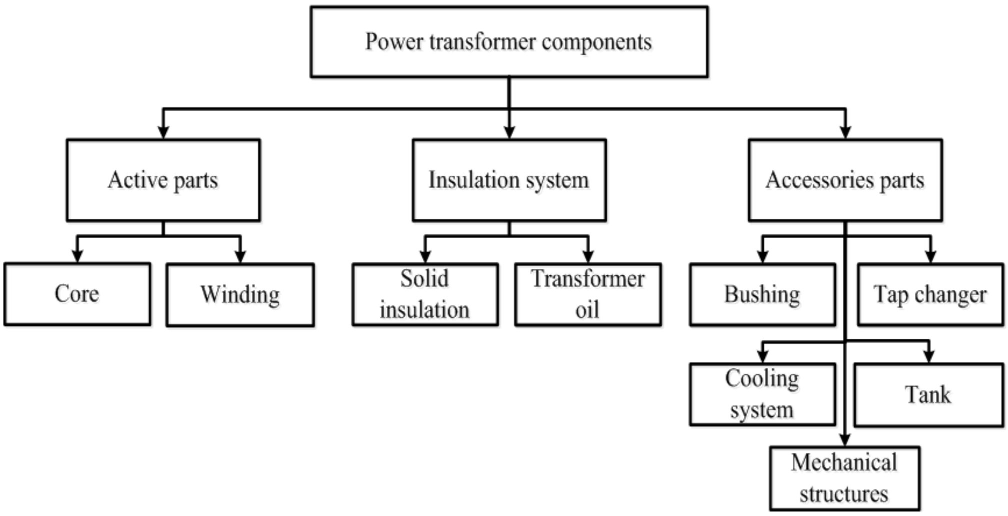

Figure 2-2 Classification of transformer components

Several global surveys have been conducted to identify the reliability of power transformers within electrical power distribution and transmission networks. In order to understand the full picture of when a transformer fails, there are three areas that should be investigated: 1) failure location, 2) failure cause, and 3) failure mode [29].

In [29], a survey conducted in Germany and South Africa collected statistical data from the period between 1996 and 2006 regarding the location, cause and mode of transformer failure. This data was then processed and analysed by CIGRE to provide a detailed study of transformer failure. As can be seen in Figure 2-3, transformer failure location was found in most cases at its protection parts, next at the tap changer and bushing, and then at the transformer windings. Figure 2-4 shows that the causes of transformer failure are firstly attributed to inherited deficiency, then to the environment or a system event, then to abnormal deterioration. Based on Figure 2-5 and several other studies [30], the largest detected classified failure was due to mechanical fault.

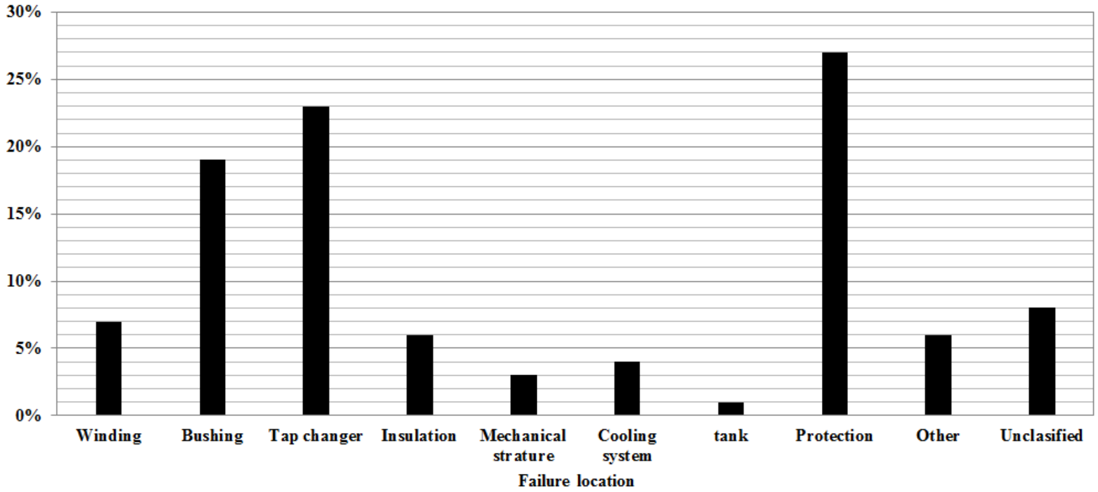

Figure 2-3Failure locations of power transformers [30]

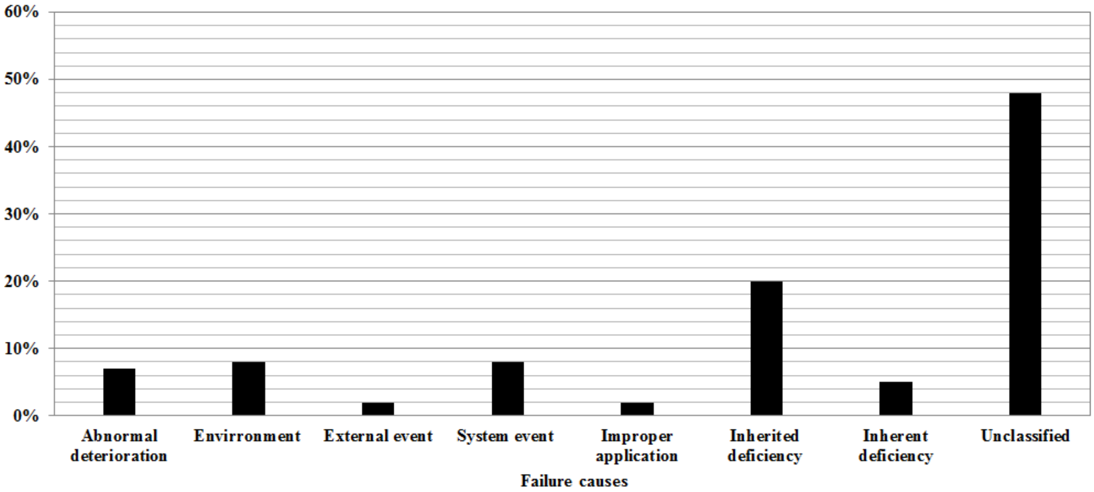

Figure 2-4 Failure causes of power transformers [30]

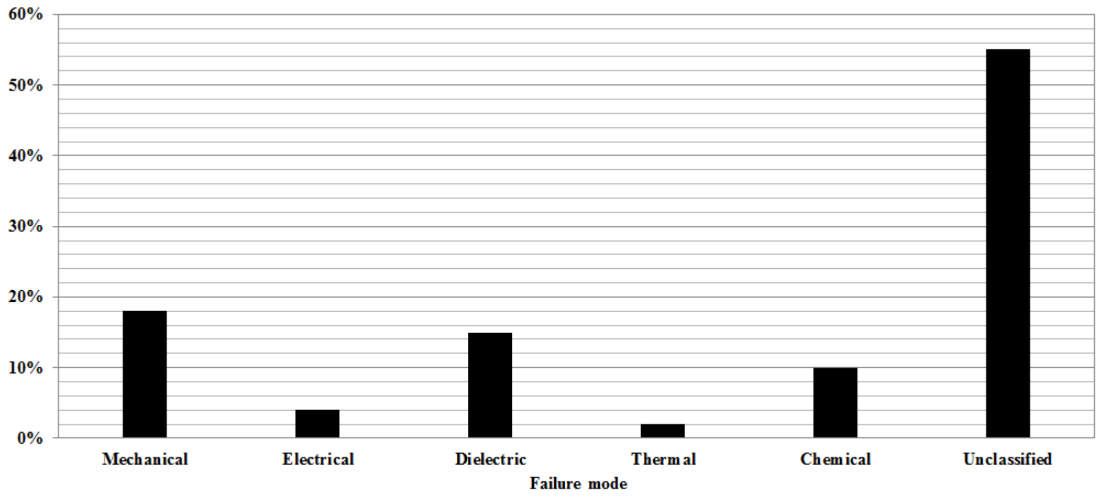

Figure 2-5 Failure modes of power transformers [30]

2:3 CMD Techniques

Several power transformer CMD techniques have been developed and accepted by the industry to investigate the health condition of various components within the transformer. Electrical power utilities and other stakeholders are interested in adopting such cost-effective CMD techniques in order to minimise maintenance costs, maximise service life expectancy and reduce life-cycle costs, all of which can be achieved by implementing a condition-based maintenance scheme rather than a routine servicing (time-based maintenance) scheme. A survey conducted by Hartford Steam Boiler over a period of more than a decade (exactly 13 years) collected significant data surrounding the common reasons behind power transformer failure [31]. Analysis of the collected data revealed that several factors can lead to transformer failure; these are:

- Instantaneous short circuits
- Extraordinary lightning and earthquake
- Inadequate maintenance
- Poor workmanship
- Deteriorated insulation systems
- Overloaded operations
- Moisture migration
- Loose connections

The use of CMD techniques significantly improves the diagnosis process by accurately analysing the obtained data and correctly reporting the health of the investigated transformer. Current CMD techniques can be administered on both energised transformers (on-line) and de-energised transformers (off -line), the choice of which depends on the nature of the test and its requirements [19]. Figure 2-6 shows some of the tests that can be conducted under each of these two categories.

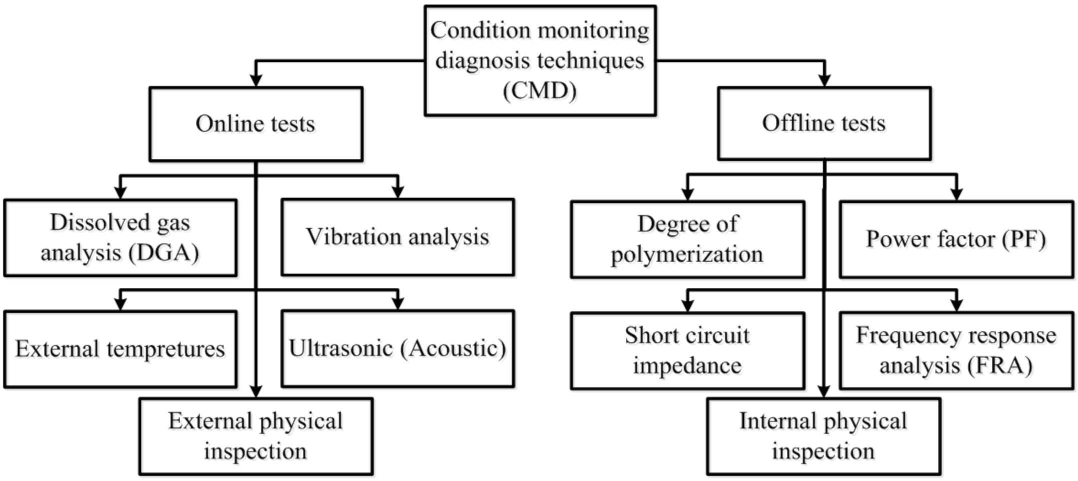

Figure 2-6 Transformer CMD techniques based on test's nature

Several CMD techniques can be found in the literature review. The following subsections briefly highlight the most common techniques:

2:3:1 Dissolved Gas Analysis (DGA)

DGA is a powerful tool that analyses the dissolved gases within the transformer's insulating oil. Due to high electrical and thermal stresses, the insulation system within the power transformer (oil and paper) decomposes, releasing characteristic gases that dissolve into the oil and decrease its dielectric strength [32]. Detection of these gases using DGA means that various electrical and thermal faults —such as partial discharge, arcing and overheating — can be identified based on the identity and quantity of released gases [33].

The type and quantity of a particular gas, along with its rate of generation, is attributed to a particular fault and severity. DGA measurements can be conducted in a laboratory environment using the chromatography technique, or online [34, 35]. As shown in Figure 2-7, various interpretation techniques have been developed to analyse DGA results.

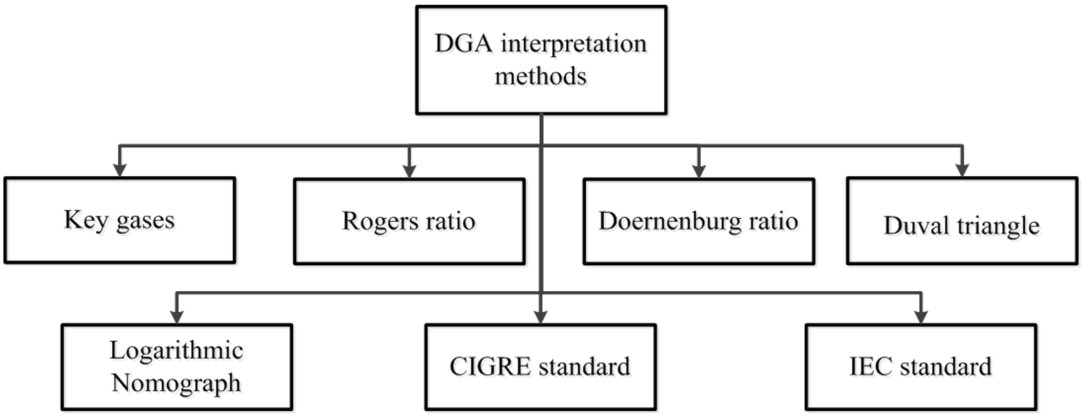

Figure 2-7 DGA interpretation techniques

2:3:2 Vibration Analysis (VA)

The energised transformer emits vibrations and noises. This is due to the windings' electromagnetic forces, the core magnetostrictive forces, the cooling fan's mechanical wave, the on-load tap changer (OLTC), and also fluid excitations from the pump [36, 37]. The vibration analysis technique was introduced in 1894 by Remington, who studied the vibration behaviour and electromagnetic properties of an air-core transformer [37, 38]. Many studies have since monitored the mechanical integrity of the power transformer's core and windings by using the measured vibration signal of the transformer tank. However, especially in the case of low vibrations, this technique still requires further investigation to ensure a failure is identified correctly [37, 39].

The vibration signals of the transformer's core and windings travel through the insulation system (transformer oil) to strike the transformer wall that should be fitted with accelerometers for measuring emitted signals. The vibrations are formed as a series of decaying bursts; an individual burst consists of a group of decaying sinusoidal waveforms. Vibration analysis can also monitor the transformer's OLTC [36]. This is an essential part (and the only dynamic part) of the transformer that allows regulation of the transformer's output voltage — through the addition or subtraction of winding turns — without interruption of load current. Transformer OLTC failures can be caused due to poor connection, weak springs, or a damaged driving mechanism inside the tap changer.

2:3:3 Partial Discharge (PD)

PD is a small area of localised dielectric collapse within the insulation system. It is caused by a lack of dielectric strength to withstand electric field stresses. PD creates a surge between the insulation system of the transformer conductors and the ground [40, 41]. Consistent discharge over time erodes the insulation system and, if not corrected, will have significant consequences, eventually leading to complete transformer failure [42]. The strength of PD can be defined during PD measurement and is based on a pre-defined voltage value from which discharge is supposed to start [43]. PD can be classified into four categories:

- **Internal discharge** — due to the cavities and voids inside the solid and oil dielectric materials that can be attributed to poor workmanship or ageing. Constant discharge on solid dielectric materials can form discharge channels within the dielectric materials and cause an internal discharge.
- **Surface discharge** — due to the contact between the boundaries of different dielectric materials, e.g. the surface of gas or liquid in contact with a solid.
- **Corona discharge** — due to discharge of gases attributed to divergent fields in the air or other gases.
- **Floating discharge** — due to electrical floating potentials related to gaseous dielectrics.

Several techniques have been adopted by the industry to detect PD activities, including the use of optical fibre sensors, piezoelectric sensors, or ultra-high frequency (UHF) sensors [44, 45].

2:3:4 Thermal Analysis (TA)

As the majority of faults within the power transformer change its thermal behaviour, a thermal monitoring method is required to observe transformer health condition. The ageing process of the transformer insulation system is accelerated due to thermal effects within the transformer [46]. Thermal stresses can be detected through Hot Spot Temperature (HST) and thermography analysis [47]. Thermal stresses within the power transformer can be identified using two industrial standards (NEMA and ANSI), which define several insulation materials under various temperature ratings

[48]. Although TA techniques are highly effective, some studies report that its sensitivity is still unable to detect rapidly developing faults [49, 50].

2:3:5 Power Factor (PF)

PF, which is also known as dielectric dissipation factor measurement, is applied to the transformer to monitor oil resistivity. In the case of new oil, resistivity measured at temperatures up to 20^o should be greater than $10x10^{12}$ Ω.metres [51, 52]. Oil resistivity is important when identifying the health condition of a power transformer, because it measures the ability of the insulation system to conduct electricity. A PF test is used to identify whether or not the transformer oil is contaminated (e.g. by moisture), which then reduces its resistivity [53, 54]. The voltage value applied to the oil sample during the test is commonly less than the rated voltage of the investigated transformer; however, the voltage value should be enough to detect contaminants in the insulation oil [55, 56].

2:3:6 FRA Test

The FRA test is the most reliable diagnostic technique for detecting mechanical deformation within the power transformer. The main concept of the FRA technique is that mechanical failures cause a change to the equivalent electrical parameters of the transformer, consequently leading to a change in the frequency response signature of the defected winding. A comparison process should be conducted between the measured FRA signature and the reference (fingerprint) signature to detect any variation. A healthy transformer’s fingerprint can be acquired prior to connecting the power transformer into service. If reference signatures are not available, another comparison technique should be adopted, such as phase to phase or an identically constructed transformer comparison. Alternatively, the reference for a healthy transformer (especially an old transformer) can be obtained through a Finite Element Analysis (FEA) technique, which is based on the transformer’s physical dimensions and structural design.

The FRA technique was developed from the idea that all transformer elements (including its active parts and insulation system) can be modelled as a cascaded network of resistive and inductive/capacitive reactance components [57]. As these components are frequently dependent on each other, any particular variation in the physical structure and/or insulation system of the transformer will change the component's value in a unique way [8, 12]. The FRA test is conducted by taking the investigated transformer out-of-service and applying a sweep frequency voltage of low amplitude (10 V) to one terminal of the transformer winding, and then by measuring the response across the other terminal of the winding with reference to the earthed tank [58]. The measured FRA signature is provided as a magnitude, and also as phase angle plots of the winding impedance, admittance, or transfer function (V_{output}/V_{input} in dB) in a wide frequency range (up to 2 MHz). Several mechanical failures — such as short-circuit faults, axial displacement, disk space variation and radial deformation — as well as some non-mechanical failures — including transformer oil degradation and bushing collapse — can be detected by applying the FRA test. Interpretation of the FRA technique, however, remains challenging, because it relies on graphical analysis by a person with high-level qualifications and expertise, often causing inconsistent results for the same FRA signature. Also, because failure of the transformer introduces only a slight variation to the FRA signature, the impact of incipient faults on the FRA signature is not easily detected by a visual inspection (naked eye).

The subsequent chapter investigates the condition monitoring of the transformer winding mechanical deformation using FRA technique.

Chapter 3 Monitoring Transformer Mechanical Deformation using FRA Technique

3:1 Introduction

The mechanical integrity of active parts within the power transformer should be maintained at a normal condition during its entire service period. This is because the nature of a mechanical fault is often progressive [59]. While a transformer can still work under a minor mechanical fault condition, significant consequences can arise if the fault is not attended to at an early stage [60]. If left unattended, the fault could create a catastrophic collapse of the power transformer, in turn causing detrimental impact to the environment, loss of revenue, or serious injury to the operating and maintenance teams.

Mechanical deformation of the active parts within the power transformer can be attributed to many different factors [61]. The most common reason for mechanical deformation in the winding is the short circuit (SC) current [62]. As it flows through the transformer winding, it generates massive electromagnetic forces (EMF) over a short period of time, leading eventually to its deformation and displacement [63]. A short circuit current can occur in a transformer winding for many reasons, such as an external short circuit fault (due to a lightning strike hitting the power line), or damage to a poorly manufactured winding during a factory-performed short circuit withstanding test [64]. Careless transportation of large power transformers (LPT) can also affect the transformer's mechanical integrity [12]. Many studies have investigated the impact of transportation procedures on power transformers, because all transformers are shipped when installed, relocated or repaired, and there are high costs associated with its proper configuration within the energy network [65]. In [66], a survey was conducted on a number of LPT case studies, looking at the consequences of careless shipping and the expense of attending to any mechanical deformations.

Another reason for mechanical deformation, which should not be overlooked, is unforeseen circumstances, such as earthquakes, lightning or heavy rains [67, 68]. These conditions can cause several forms of mechanical fault that could destroy the in-service transformers.

The FRA technique is the most reliable test for monitoring mechanical deformation in the transformer. However, it is inefficient in its detection of minor (incipient) faults, and also there is currently no trusted global standard that can be used to interpret the FRA results. To overcome some of these recognised drawbacks, the FRA test requires further technical and professional study.

3:2 Mechanical Faults within Transformer Windings

A short circuit current subjects the transformer winding to a huge EMF, which deforms and displaces the windings [69]. Depending on the magnitude and direction of the EMF, deformation and displacement can occur in several different locations and from many different directions. The essential parameter used to calculate the EMF is the transient current, which flows into the transformer windings. Within three-phase, the short circuit fault generally produces a transient current of a very high magnitude. This short circuit current (I_{SC}) is measured approximately as follows [63, 70]:

$$I_{SC}(t) \approx I_0 e^{-\frac{t}{\tau}} + \sqrt{2} I_{SS} \left(cos(\omega t + \psi - \varphi) - e^{-\frac{t}{\tau}} [cos(\psi - \varphi)] \right) \quad (3.1)$$

where:

$$\tau = \frac{L_{eq}}{R_{eq}};\ I_{Sc} = \frac{V_m}{\sqrt{{R_{eq}}^2+\omega^2{L_{eq}}^2}};\ \varphi = \tan^{-1}\frac{\omega L_{eq}}{R_{eq}} \qquad (3.2)$$

I_{SC} and I_{SS} are the short circuit current and its steady state value, respectively, t is time, ψ is the voltage angle when fault is occurred, I_0 is the initial current, R_{eq} and L_{eq} represent the total series resistance and inductance of the windings, respectively, and V_m is the maximum voltage. The short circuit current (I_{SC}) at maximum peak value is calculated by:

$$I_{SC}(t) \approx I_0 e^{-\frac{t}{\tau}} + \frac{V_m}{\sqrt{{R_{eq}}^2+\omega^2{L_{eq}}^2}}\cos(\omega t - \psi) \ (3.3)$$

The electromagnetic forces, which are imposed on the coils, increase significantly during an attending short circuit fault. They are calculated by combining the transient current and the leakage flux [71] as shown below:

$$\vec{F} = l\vec{I} \times \vec{B} \qquad (3.4)$$

where $\vec{F}$ is the EMF, the current intensity vector is represented by $\vec{I}$, l is the conductor length, and $\vec{B}$ represents the magnetic flux density.

Magnetic flux density in a transformer is the main parameter of the EMF calculation. It is made up of two directional components: the radial forces adopted on axial components, and the axial forces adopted on radial components [71, 72]. The axial forces compress both the HV and LV windings on the centre side axially, which causes vertical movement of the winding, completely (axial displacement (AD)) or partially (disk space variation (DSV)). This may either bend the windings or break the clamping structure [73]. The radial forces, however, push the internal winding inward, causing compressive stress (forced radial deformation) and pushing the external winding outward by the tensile stress (free radial deformation). Figure 3-1 shows the EMF as perpendicular to the magnetic flux density within the two windings of the transformer. In this figure, both the EMF and magnetic flux density are comprised of two components: vertical (Fy and By) and horizontal (Fx and Bx), where Bx and By create Fy and Fx, respectively.

Since the leakage flux field depends on the winding current as expressed in Equation (3.4), it can cause transient electromagnetic forces and increase the temperature inside the transformer, which then leads to winding deformation and displacement [71].

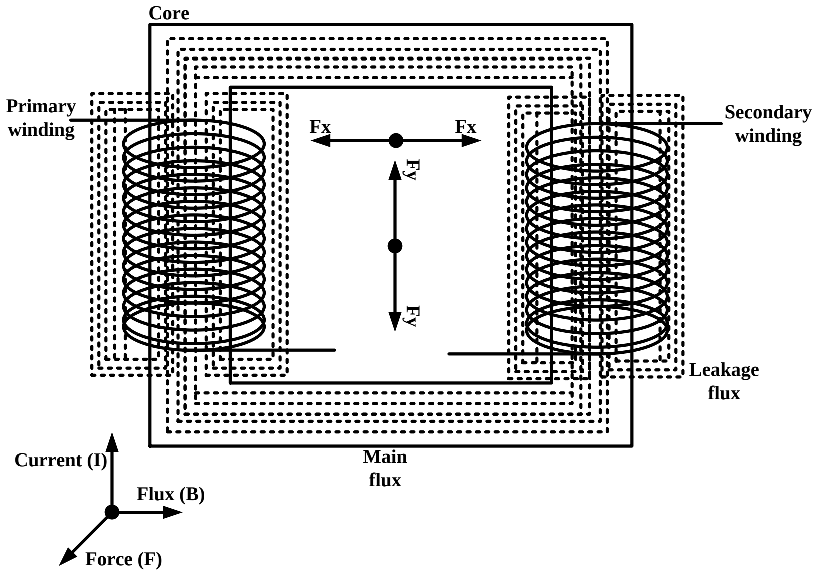

Figure 3-1 Schematic diagram showing the flux field and EMF of two windings of the transformer

3:2:1 Axial Forces Deformation

Axial displacement (AD) and Disk Space Variation (DSV) are the two most common modes of axial force that influence transformer windings. As the current inside the HV and LV windings flows in opposite directions, axial forces are imposed on both windings in inverse directions simultaneously, forming a symmetric distribution. A short displacement in a single winding alters the symmetric distribution of the forces between the windings, and increases the axial forces [74]. When a clamping force is unable to withstand the axial forces, the transformer winding is perpendicularly moved upwards or downwards as illustrated in Figure 3-2 (a). Significant axial forces can cause immediate damage to the transformer winding, as well as to parts of the clamping structure, such as the press plate and pressure ring [75]. Axial forces can also create a DSV, which only partially moves the transformer winding. These lesser forces are not able to displace the entire winding but are able to move some disks within the winding as shown in Figure 3-2 (b).

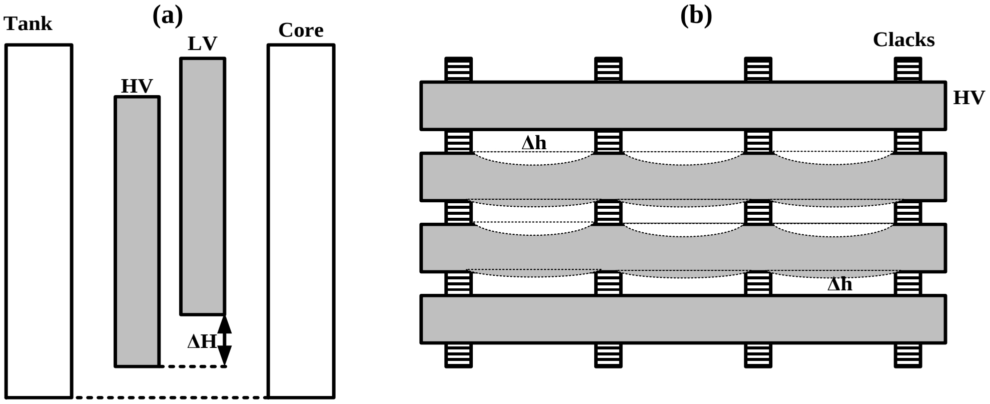

Figure 3-2 Schematic diagram of axial forces deformation of HV winding: (a) AD and (b) DSV

3:2:2 Radial Forces Deformation

As stated above, radial forces on transformer windings are generated when short circuit currents and magnetic flux interact. Upon exceeding certain limits, these forces may lead to winding radial deformation [1, 76]. Excessive radial forces generate a tensile stress that pushes the outer winding towards the tank (free radial buckling), while the inner winding is subjected to compressive stress that pushes the winding inward (forced radial buckling) [76]. Figure 3-3 (a) illustrates the impact of free radial buckling on an HV winding, and Figure 3-3 (b) shows how forced radial buckling influences the LV winding. Forced radial buckling causes the conductor to bend in alternate spans, while free radial buckling causes a bulge on one or more edges of the conductor [76].

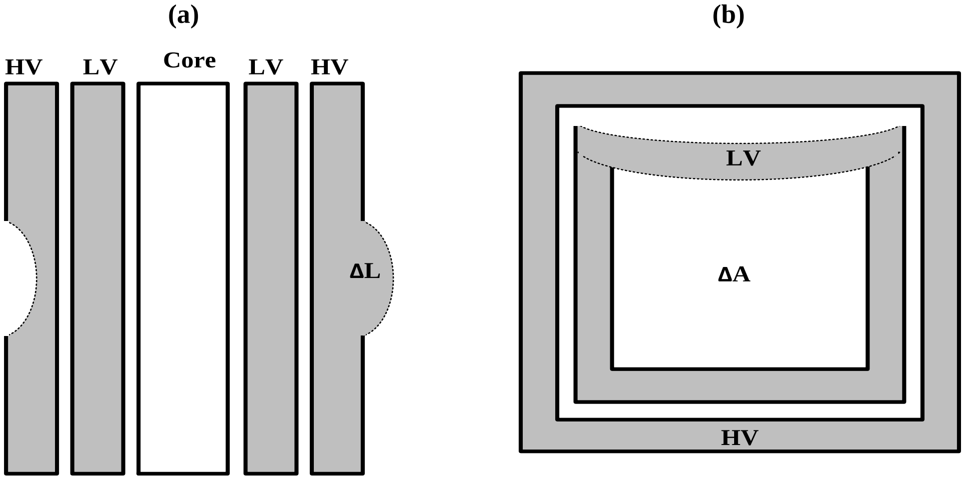

Figure 3-3 Schematic diagram of radial forces deformation of HV and LV windings: (a) free and (b) forced

3:2:3 Other Mechanical Faults within Transformer Windings

In addition to the above-mentioned mechanical faults, which are formed due to axial and radial forces, transformer windings can experience other mechanical faults, including short circuit turn (inter-turn) faults. The main reason for winding turn to short circuit is the collapse of the insulation between the adjacent conductors in the transformer windings. As can be seen in Figure 3-4, the short circuit inside the transformer leads to overheating of the winding, while the deteriorating mechanical strength of the insulation causes short-circuiting in the winding conductors [77, 78]. Consequences of the winding overheating include fusion of the surrounding components, which are manufactured using copper [64].

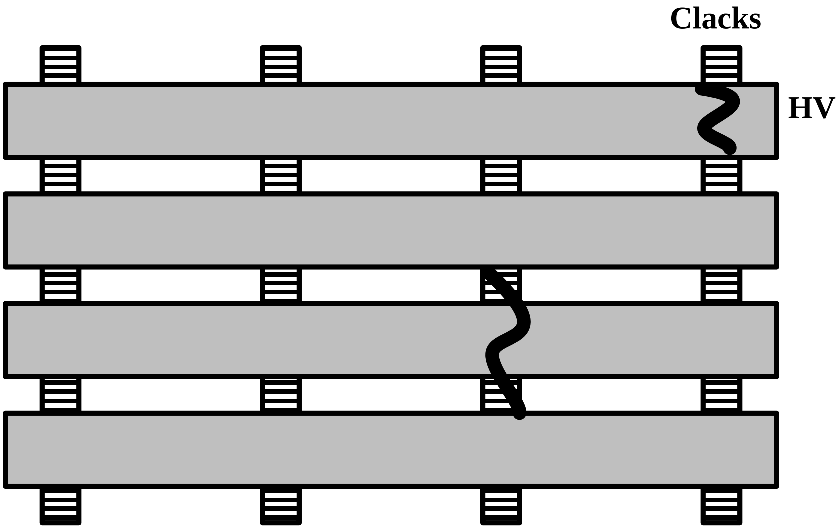

Figure 3-4 Schematic diagram of SC faults in HV winding

3:3 CMD Techniques for Mechanical Faults

Mechanical faults in the transformer can be detected using several techniques, including:

- Transformer excitation current (TEC) test
- Leakage inductance (LI) test
- Winding capacitance (WC) test
- Frequency response analysis (FRA) test

From the above tests, the FRA test is the most reliable for identifying various transformer winding faults. This is because it is sensitive enough to detect all existing mechanical faults, whereas the TEC, LI and SC tests detect only certain mechanical faults (usually radial deformation) [60, 79-81]. Table 3-1 summarises the advantages and disadvantages of the FRA technique [12].

Table 3-1 Advantages and disadvantage of the FRA technique

Advantages	Disadvantages
Simple configuration and fast responses obtained	**Difficult to detect minor levels of mechanical failure**
Sensitive in detecting mechanical winding deformation	**Difficult to interpret FRA responses due to lack of standard codes**
Sensitive in detecting non-mechanical deformation (transformer bushing failures and transformer oil degradation)	**Service outages, as FRA is offline test**

The FRA test is conducted at three points during the transformer's lifecycle: 1) before service commencement, when a reference measurement is obtained either at the factory or on site, 2) any time a transformer is relocated, when the test looks specifically for any transportation damages, and 3) any time a transformer shows signs of requiring maintenance. The FRA response for transformer windings relies on the equivalent high frequency (HF) transformer model, which is comprised of a cascaded network of resistive, inductive and capacitive reactance components.

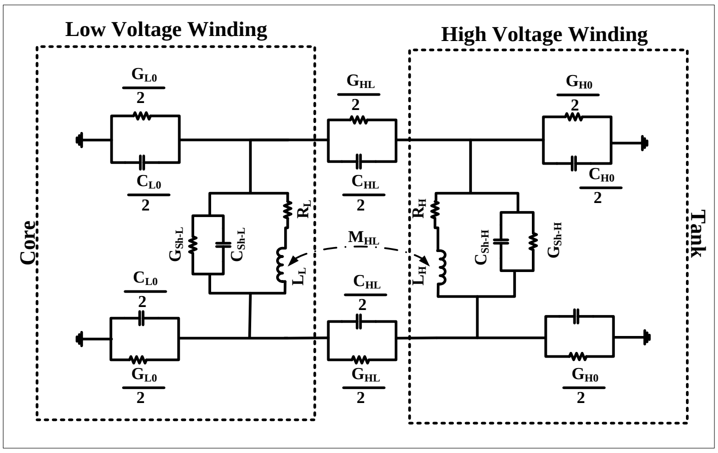

Figure 3-5 Equivalent circuit of transformer winding (one disk/turn)

Figure 3-5 shows the most common representation of an HF transformer. It is based on the parameters of a RLC equivalent circuit [70, 76], which include winding resistance and inductance (R_s, L_s), winding insulation capacitance and conductance (C_{sh}, G_{sh}), capacitance and conductance of the insulation between the windings (C_{HL},

G_{HL}), coil mutual inductance (M), and insulation capacitance and conductance between the HV/LV windings and the earthed tank/core (C_o, G_o).

Mechanical deformation of a transformer’s physical geometry leads to changes in the values of RLC parameters and consequently the FRA response. The FRA test detects the change by taking the investigated transformer out-of-service, applying a sweep frequency voltage of low amplitude to one terminal of a transformer winding, and then measuring the response across the other terminal of the winding with reference to the earthed tank [58]. The measured FRA signature is plotted in a wide frequency range as magnitude and phase angle of the winding impedance, admittance, or transfer function (V_{out}/V_{input} in dB).

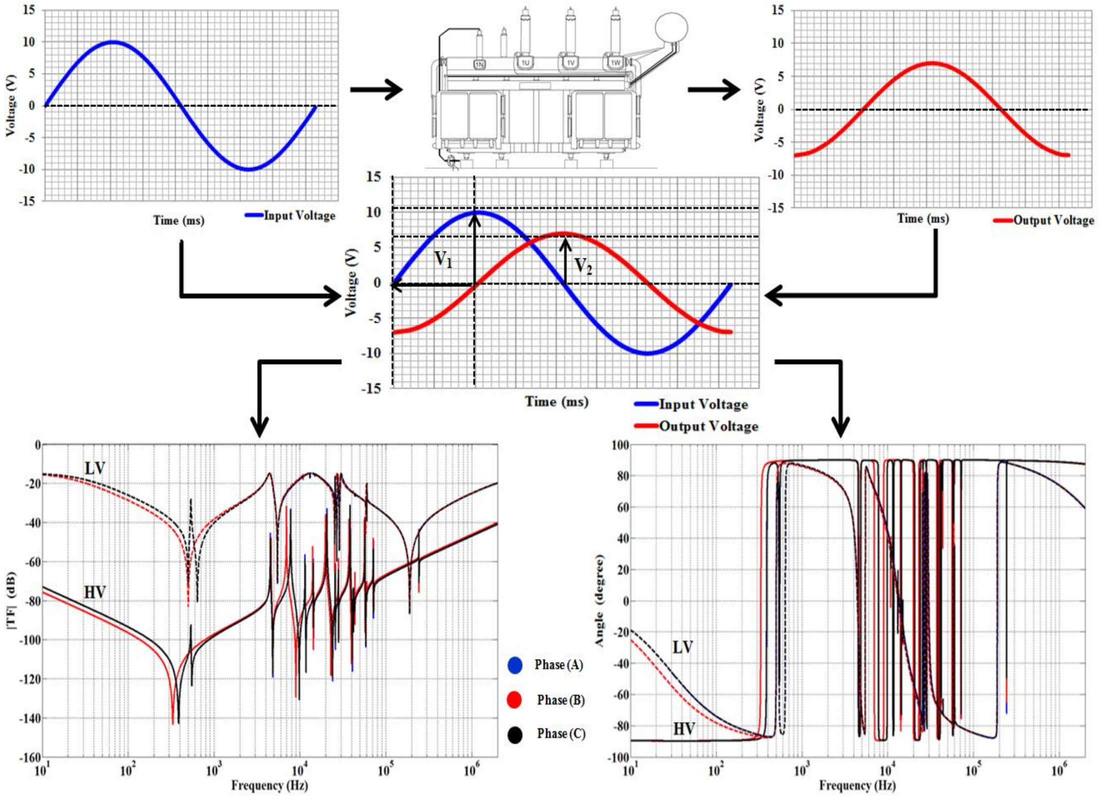

Figure 3-6 The methodology of an FRA test on a three-phase power transformer (input and output voltages are shown only at the power frequency)

As shown in Figure 3-6, the FRA signature of the transformer is obtained by connecting a low-amplitude AC voltage source (10 V) of a variable frequency (V_{in}) at one terminal of the transformer winding, and then by measuring the response signal at the other terminal of the same winding (V_{out}). Other phases are left open-circuited. The transfer function of each phase within the HV and LV transformer windings is calculated in a wide frequency range (up to 2 MHz) and plotted as magnitude (in dB) using Equation 3.5 and phase angle (in degrees) using Equation 3.6.

$$|\mathrm{TF}| = 20\log_{10}\left(\frac{V_{output}}{V_{input}}\right) \qquad (3.5)$$

$$\angle\mathrm{TF} = tan^{-1}\left(\frac{V_{output}}{V_{input}}\right) \qquad (3.6)$$

All commercial FRA analysers are able to obtain an FRA response in the form of magnitude and phase angle plots, however currently only the magnitude signature is used to analyse the health condition of the transformer winding (conventional approach). The conventional approach (current FRA practice) requires two FRA signatures, determining any variation between the two. One of these two signatures is the reference (fingerprint) signature, which is measured at the test of acceptance before a transformer commences service. The second signature shows the current condition of the transformer under study. FRA testing is strongly recommended for new transformers prior to connection to the network, so a reference dataset can be acquired. It is expected that a pool of reference datasets will be readily available for standard power transformers in the future.

For old transformers, it is important to note that the healthy reference dataset acquired from FRA practical measurement may reflect an already-developed internal fault within the transformer. In this instance, another comparison technique is necessary for diagnosis, such as the use of an FRA signature for an identically constructed transformer or the adoption of a phase-to-phase transformer. It is expected that all phases within the same transformer will have almost identical FRA signature, and any significant deviation among these signatures is considered indication of a fault. The FRA reference signature of the transformer winding can also be obtained through a 3D finite element model of the investigated transformer, which is based on its physical dimensions.

3:4 Configuration and Setup of the FRA Test

In order to correctly measure the response signals, the FRA test requires some preparation surrounding configuration and setup of the analyser equipment. There are four different configurations that can be adopted for connecting the FRA analyser to the transformer terminals [18, 82, 83]. These are as follows:

- End-to-end open circuit test
- End-to-end short circuit test
- Capacitive inter-winding test
- Inductive inter-winding test

3:4:1 End-to-End Open Circuit Test

The end-to-end open circuit test can be conducted on either HV or LV windings by connecting the FRA analyser to the terminal of the suspected winding, injecting a low amplitude voltage (10 V) with a variable frequency (up to 2 MHz), and then measuring the response signal across the other terminal of the same winding. As the terminals of the unexamined winding are floating (i.e. the terminals are left open), this test is conducted as an open circuit test. The configuration of this test is commonly applied to obtain the FRA signature of the transformer winding because it is particularly sensitive to winding failure, more so than the other configuration connections [12]. It is also considered a very simple test because the windings are examined individually [81]. Configuration of the end-to-end open circuit test on both HV and LV windings is illustrated in Figures 3-7 and 3-8, respectively.

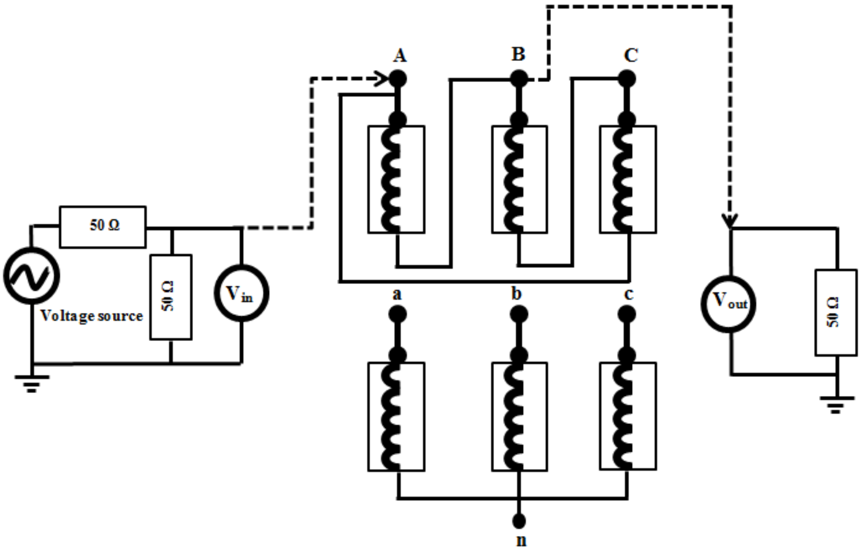

Figure 3-7 End-to-end open circuit test of the three-phase transformer HV winding (delta connection) 50 Ω co-axial cables used to connect FRA analyser with transformer winding

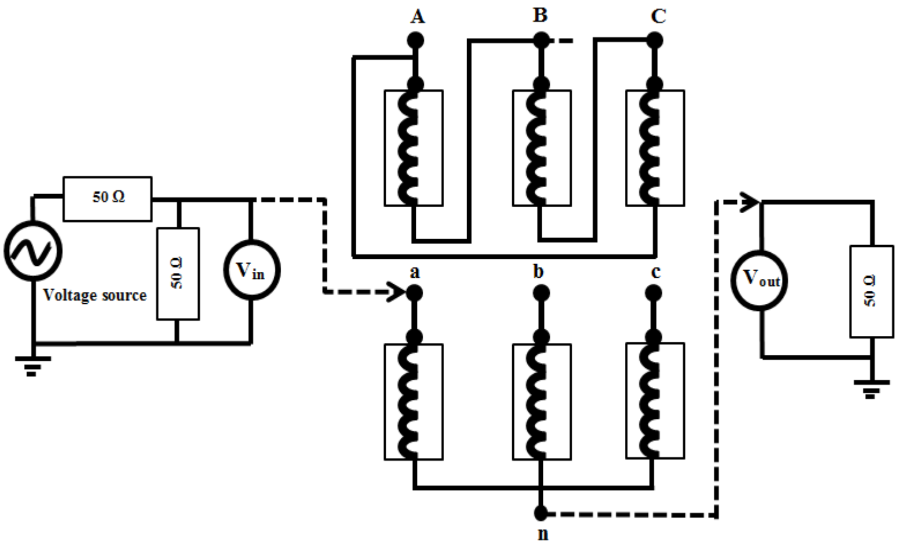

Figure 3-8 End-to-end open circuit test of the three-phase transformer LV winding (Wye connection)

3:4:2 End-to-End Short Circuit Test

The end-to-end short circuit configuration is very similar to the open circuit test, except here the terminals of the other winding are connected simultaneously (i.e. short circuited).

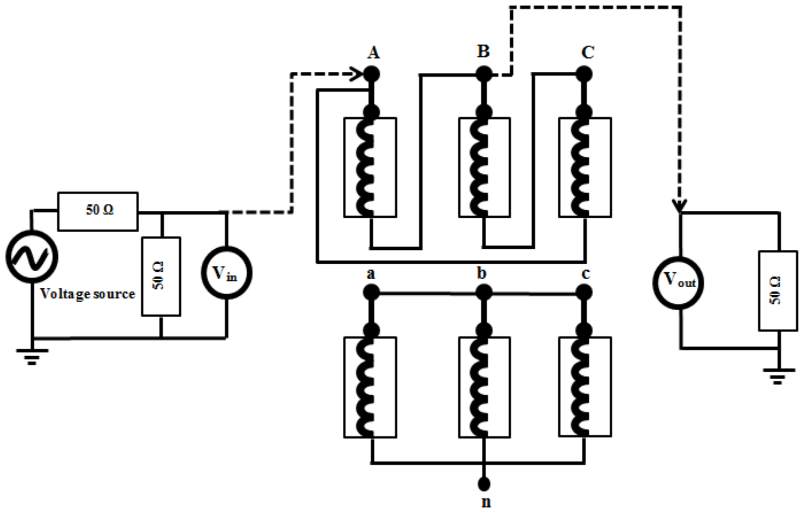

Figure 3-9 End-to-end short circuit test of the three-phase transformer HV winding

This excludes the impact of the core's electromagnetic inductance on the frequency response. The short-circuited terminals of the untested winding can assist in understanding the source of failure, i.e. if it was the core or not [12]. The configuration of the end-to-end short circuit test on the HV winding is illustrated in Figure 3-9.

3:4:3 Capacitive Inter-Winding Test

In the capacitive inter-winding test, unlike in the previous configurations, the FRA analyser injects the signal at the terminal of one winding, and then the response signal is measured across the same phase on the other winding [12]. Also, in this test, the input signal should be injected into the HV winding. The LV winding is used to measure the output signal and vice versa. This test has been reported as inadequate, due to the difficulties associated with understanding the frequency response [24]. Implementation of this test configuration on the HV winding is shown in Figure 3-10.

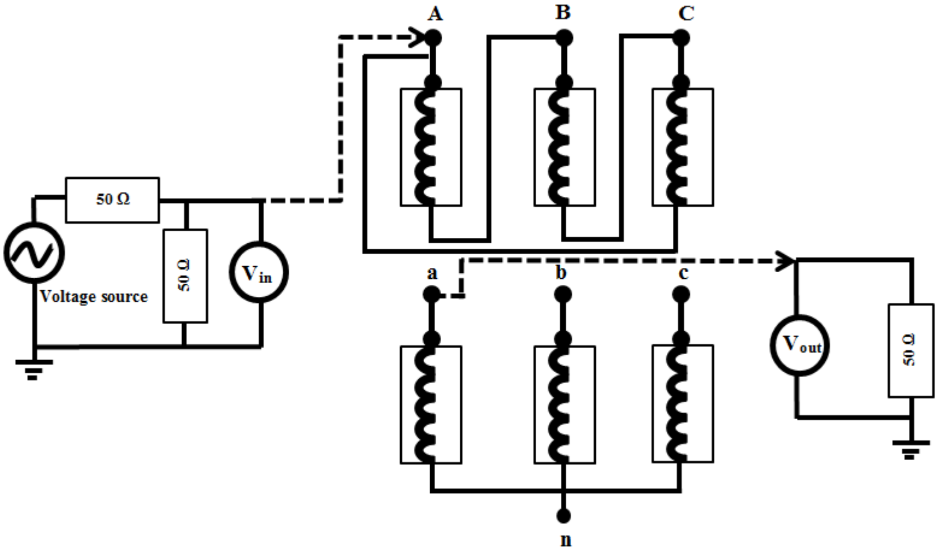

Figure 3-10 Capacitive inter-winding test of the three-phase transformer HV winding

3:4:4 Inductive Inter-Winding Test

The inductive inter-winding test is similar to the capacitive inter-winding test and is the last configuration test option. In this configuration, the other terminals of the HV and LV winding are connected to ground. This test can be used to measure the turns ratio of the winding based on a low frequency response as discussed in [12]. The configuration of inductive inter-winding test is shown in Figure 3-11.

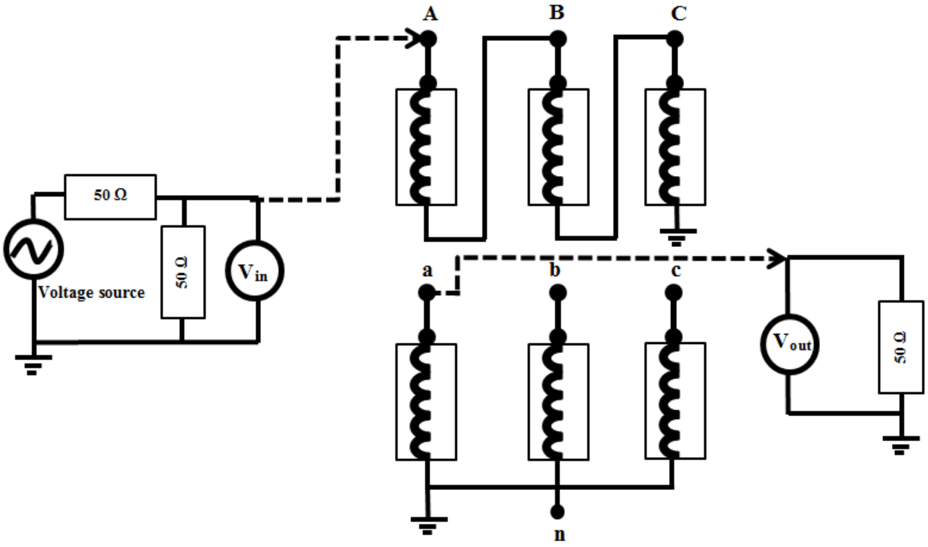

Figure 3-11 Inductive inter-winding test of the three-phase transformer HV winding

3:5 Current Methodologies for Analysing FRA Signature

As noted in the literature, the FRA technique uses well-developed and standardised equipment and methods for measurement. However, the inconsistency in interpretation of the FRA responses remains unaddressed. This is because there is no official interpretation system. In the following sections, several implemented projects that use the FRA technique are reviewed:

3:5:1 CIGRE Booklet

In April 2008, WG (A2.26) of CIGRE, which is the International Council on Large Electric Systems, released a booklet to assess mechanical conditions in transformer windings using frequency response analysis (FRA). This project concentrated on three main objectives as follows [12]:

- To help those individuals and organisations, who are interested in the transformer's monitoring field, understand the impact of mechanical windings failure on the FRA signature.

- To review the conducted practices for mechanical failure detection based on the FRA technique, also provide important suggestions for the analysis process.
- To support current studies through the introduction of an improvement guide to developing FRA interpretation approaches.

The WG (A2.26) booklet recommends setting up the configuration of the FRA analyser and transformer winding as an end-to-end open circuit connection [12]. It also suggests that the reference (fingerprint) signature, which is to be compared with the measured FRA signature, is obtained using time-based, type-based and construction-based measurements [12]. The WG (A2.26) booklet also discusses the use of statistical indicators to interpret the FRA responses. It has been noted, however, that this proposed method is unable to determine the indicator values required for distinguishing between a healthy and faulty condition [12]. Further studies should be conducted on the statistical indicators method in order to investigate its reliability prior to being adopted [12].

Several statistical indicators can be used to interpret the FRA responses, including the Standard Deviation (SD), Correlation Coefficients (CC), and the Absolute Sum of Logarithmic Error (ASLE). These indicators are based on the following Equations: 3.7, 3.8 and 3.9, respectively [12].

$$\mathrm{SD}=\frac{\sqrt{\sum_{i=1}^{n}((X_i-\bar{x})-(y_{i}-\bar{y}))^2}}{n-1} \qquad (3.7)$$

$$\mathrm{CC}=\frac{\sum_{=1}^{n} \mathrm{X_i Y_i}}{\sqrt{\sum_{i=1}^{n}[\mathrm{X_i}]^2 \sum_{i=1}^{n}[\mathrm{Y_i}]^2}} \qquad (3.8)$$

$$\mathrm{ASLE}=\frac{\sum_{=1}^{n} Y_i-X_i}{n} \qquad (3.9)$$

where Xi and Yi are the ith elements of the reference and healthy signatures, respectively, while n is the total number of selected points in the frequency response signature.

Some studies in the literature apply the proposed statistical method using the above indicators: CC, SD and the ASLE [84-86]. However, the use of these statistical indicators can result in incorrect interpretation. The use of CC indicators in certain circumstances can lead to an incorrect correlation between the two investigated signatures and is considered an inadequate parameter for FRA interpretation [86]. SD fails to reflect the information scattered around the low magnitudes of the FRA signature, so only the peak differences between the two investigated signatures are shown in the calculated value [86, 87]. The ASLE was introduced to realise a full logarithmic-scaled comparison between two FRA signatures [88]. However the reliability of using the ASLE indictor for FRA interpretation is in question, and it requires further investigation [89].

3:5:2 IEC Principle

In July 2012, the International Electro-Technical Commission (IEC) released part of series (IEC 60076-18-2012), which defines the measurement technique and measurement equipment required in the FRA test. The aim of this publication was to offer assistance during FRA examination [90]. However, it did not provide any guidance with the interpretation of the results, which would have helped form an understanding of the FRA signature [90]. In IEC 60076-18:2012, the frequency domain is divided into four areas, based on the factors illustrated below.

- Low-frequency range — less than 2 kHz, and influenced by the health condition of the transformer core.
- Middle-frequency range — between 2 kHz and 20 kHz, and affected by the interaction between transformer windings.
- High-frequency range — between 20 kHz and 1 MHz, and controlled by the winding structure failure.
- Very-high-frequency range — higher than 1 MHz, and influenced by the earthling connection and measurement set-up.

It is worth mentioning, however, that the above subdivision is not perfect. This is because the characteristic FRA can vary among the fleet of power transformers based on several factors, including their size, rating, winding structure and insulation system [90].

3:6 The Impact of Transformer Winding Faults on FRA

FRA signatures within power transformers are affected by both mechanical and non-mechanical failures. Of the many transformer components, it is the windings that are subjected to the majority of mechanical failures, including axial displacement (along with disk space variation), radial buckling (forced and free deformation) and short circuit faults. FRA signatures are also influenced by both transformer bushing failures and transformer oil degradation (non-mechanical failures). It should be noted that a change in the FRA signature is not necessarily associated with a transformer mechanical fault. In order to distinguish between a mechanical and non-mechanical failure, it is imperative to understand each one's individual impact on the response of the FRA. To achieve this understanding, experimental measurements or simulation analysis should be conducted. The majority of studies in the literature use the simulation analysis approach, which can be attributed to the following benefits:

- The simulation analysis approach can mimic the real operation of a physical transformer but is only acceptable when a proper software tool is utilised.
- The implementation of simulation analysis is easy, fast, and the least expensive option.
- The implementation of physical faults on an operating transformer for research purposes is not possible.

As long the transformer is accurately simulated, the influence of transformer failures on the FRA signature is understood correctly. As a result, the interpretation process can be properly developed to identify and quantify failures.

In the following chapter, several HF power transformers are modelled using simulation analysis, in order to obtain FRA signatures for the purpose of discussion and research.

Chapter 4 High Frequency Transformers Modelling

4:1 Introduction

When studying FRA, it is essential to develop a reliable high frequency (HF) transformer model. This is because it gives interested parties a better understanding of how both mechanical and non-mechanical faults impact the FRA signature of the power transformer. As mentioned in the previous chapter, components of the transformer (i.e. its core, windings and insulation system) can be modelled as a cascaded network of elements (R, L, and C). When the elements' values change, due to a mechanical or non-mechanical fault, the FRA signature changes accordingly.

As previously stated, professional research studies on power transformers can be conducted using simulation modelling. One of the most reliable simulation methods is the Finite Element Analysis (FEA) techniques. FEA is a computerised technique used for solving multi-physics problems of real systems. In order to find a solution, it analyses the system's surrounding fields, such as the electromagnetic field [15, 63, 91, 92]. The majority of simulation-based analysis studies on power transformers have been conducted using FEA [15, 92]. This is due to the ability of this technique to effectively mimic the genuine operation of the transformer [93]. The power transformer can be built using the FEA technique, first, by modelling it in a three-dimensional (3D) design. The design is analysed in magneto-static, electro-static and eddy current solvers, and then Maxwell’s equations are used to extract the inductance, capacitance and resistance matrices of the transformer’s equivalent electrical circuit. However, in order to obtain the actual FRA signature of the simulated transformer model, two common approaches can be used. These are: 1) the electrical distributed parameters circuit, and 2) numerical representation.

4:2 Finite Element Analysis

FEA is an advanced numerical technique, developed to solve factual problems of real systems that are surrounded by various physical fields. By modelling the geometrical complexities and nonlinear material characteristics of a system, an accurate solution can be found [94, 95]. Several studies have recommended applying the FEA technique to simulate the power transformer for various purposes, including design and manufacturing, improvement of its performance, and improvement of condition monitoring methods. The FEA technique is an ideal choice for solving electromagnetic fields problems, modelling complicated designs, and studying characteristic materials [71, 93]. However, although many FEA computer-based techniques can be applied to simulate HF transformers, ANSYS Maxwell is the most reliable computer-aided engineering platform [96, 97]. ANSYS Maxwell is a powerful, accurate, high-performance tool that uses the FEA technique for modelling, designing, simulating and analysing electromagnetic and electromechanical systems, such motors and transformers. It also solves problems with static, frequency-domain, and time-varying electromagnetic and electric fields. The ANSYS Maxwell platform uses four of Maxwell’s equations to solve problems defined by the user. These equations are listed below:

- Ampere’s Law of current

$$\nabla \times \mathrm{H} = \mathrm{J} + \dot{D} \qquad (4.1)$$

- Gauss’s Law of electricity

$$\nabla \cdot \dot{D} = \rho \qquad (4.2)$$

- Faraday’s Law of induction

$$\nabla \times E = -\dot{B} \quad (4.3)$$

- Gauss’s Law of magnetism

$$\nabla \cdot B = 0 \qquad (4.4)$$

where:

B: magnetic flux density

H: magnetic flux intensity

E: electrical field

D: electric flux density

Based on the given requirements, the above-mentioned equations, and in line with the capabilities of the ANSYS Maxwell platform, the most valid solution for the simulated system is automatically selected.

4:3 Transformer Windings Simulation using FEA

The simulation analysis studies in this thesis are conducted using the ANSYS Maxwell platform. As shown in Figure 4-1, this technique is applied to the design and model of two three-phase power transformers, each with different ratings (10 kVA and 40 MVA), physical dimensions and winding structures. Figure 4-2 shows in millimetres (mm) the 3D schematic diagrams of the two transformers under study.

In the 10 kVA transformer, the windings are designed in a rectangular shape. The HV winding comprises of six disks with 1134 turns per disk, while the LV winding is a continuous layer of 140 turns. The transformer windings of the 40 MVA are, in comparison, structured in a circular form. The HV winding consists of ten disks with 1200 turns per disk, and the LV winding is designed as a continuous layer of 200 turns. The specifications, physical dimensions and insulation system characteristics for both transformers are listed in Tables A-1, A-2 and A-3 in the appendix.

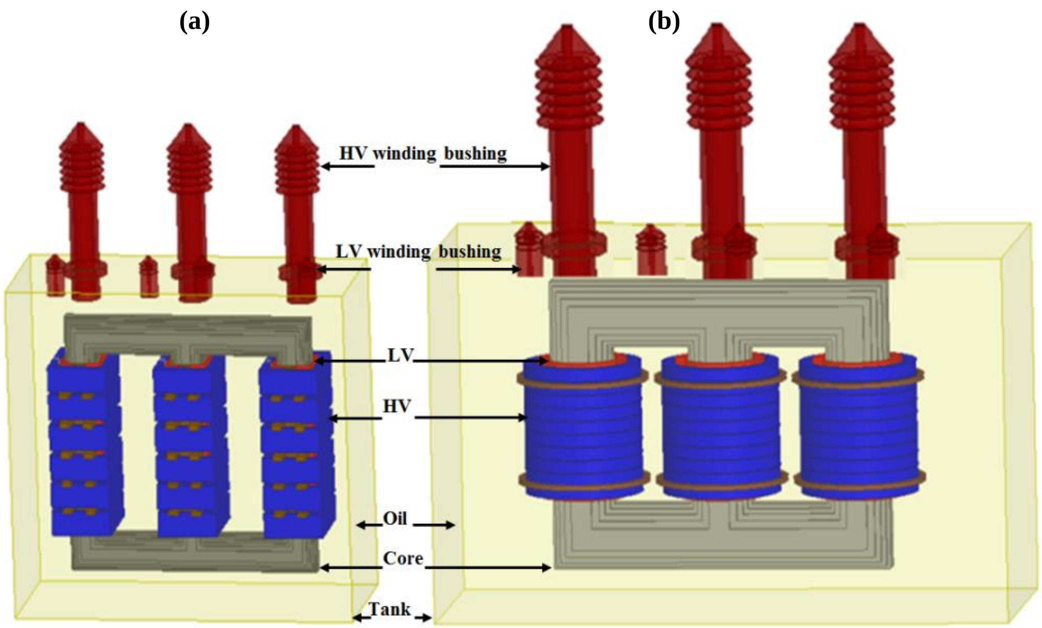

Figure 4-1 FEA transformer 3D structures: (a) 10 kVA and (b) 40 MVA

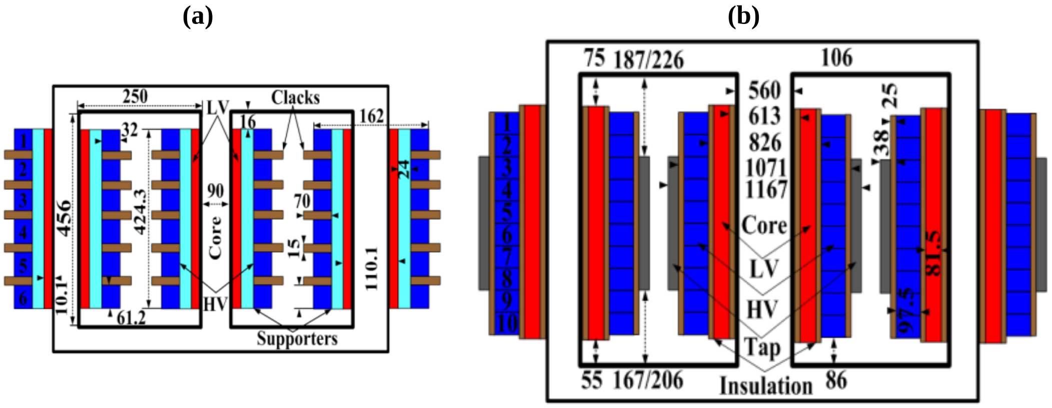

Figure 4-2 Schematic diagrams with dimensions in mm: (a) 10 kVA and (b) 40 MVA

4:4 Transformer Insulation System

The insulation system of a power transformer consists of paper immersed in either mineral- or vegetable-type insulating oil. Mineral oil is the most popular fluid used for insulating electrical equipment, such as the power transformer [98]. Researchers have recently attempted to improve the technical attributes of mineral oil to overcome some of its drawbacks. These drawbacks include its non-eco-friendly nature, and due to the shortage of petroleum-based products, its anticipated forthcoming price increase [98, 99]. The dielectric property of the insulation system is characterised by two fundamental factors: permittivity and conductivity. Permittivity affects the behaviour of the insulation system during electrical transient conditions, while electrical conductivity plays an essential role in specifying the dielectric strength of the insulating system [100, 101]. As depicted in Figure 4-3, the model of the transformer’s insulation system can be implemented using complex capacitance ($C_{insulation}$), represented as double conductive layers of paper with oil in-between [102, 103].

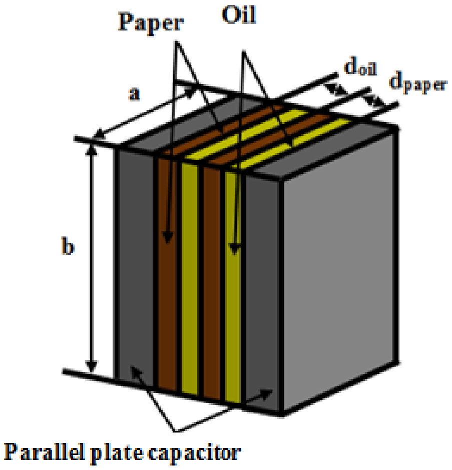

Figure 4-3 Constructive model of the main insulation system

The main insulation systems, located between the HV and LV windings of the investigated 10 kVA and 40 MVA transformers, are shown in Figures 4-4 (a) and (b), respectively.

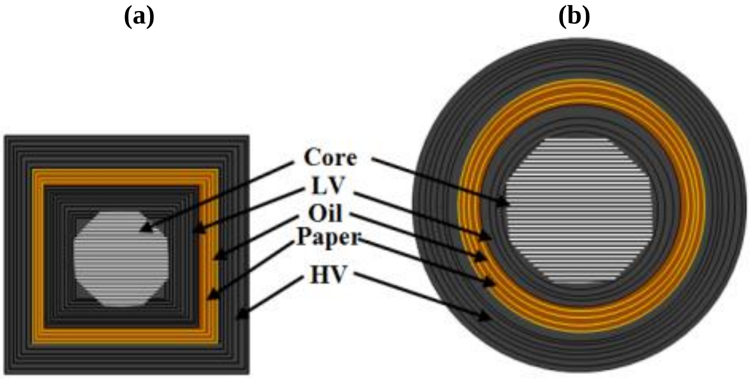

Figure 4-4 Main insulation system: (a) 10 kVA model and (b) 40 MVA model

The calculation of $C_{insulation}$ depends on both the complex permittivity (ε_x) and the electrical conductivity (σ). The complex permittivity of the transformer insulation system is calculated as follows:

$$\varepsilon_{x.oil} = \frac{\sigma_{oil}}{j.\varepsilon_{0.oil}.\omega} + \varepsilon_{r.oil} \qquad (4.5)$$

$$\varepsilon_{x.paper} = \frac{\sigma_{paper}}{j.\varepsilon_{0.paper}.\omega} + \varepsilon_{r.paper} \qquad (4.6)$$

where, ε_x, ε_r, and ε_0 refer to the complex, relative, and vacuum permittivity, respectively. σ is the electrical conductivity (s.m^{-1}) and ω is the frequency (rad.s^{-1}).

The equivalent capacitance that represents transformer insulation system can be calculated based on (4.7) below:

$$C_{insulation} = A\left[\frac{\varepsilon_{0.oil}.\varepsilon_{x.oil}}{d_{oil}} + \frac{\varepsilon_{0.paper}.\varepsilon_{x.paper}}{d_{paper}}\right] \quad (4.7)$$

where *A* and *d*, are respectively the plate area and thickness of the insulation.

The main insulation system of the two transformers under investigation can be represented by an average complex capacitance. Its value is affected by moisture content, which significantly accelerates the insulation aging process [104].

As shown in Figure 4-5, the FEA technique is used to evaluate the correlation in both transformers between the total transformer oil capacitance and the percentage increments in oil complex permittivity and electrical conductivity. As also can be seen in this figure, the increase in ε_x and σ, which can be used to simulate deterioration of the insulation system [23], leads to an increase in the total capacitance of the transformer's insulation system. The results of Figure 4-5 show that, due to dielectric factor variation, vegetable oil exhibits more changes to capacitance than mineral oil. It can also be observed that the increase in insulation capacitance of the 40 MVA transformer is more than that of the 10 kVA transformer. This is attributed to the volume of the insulating oil in both transformers.

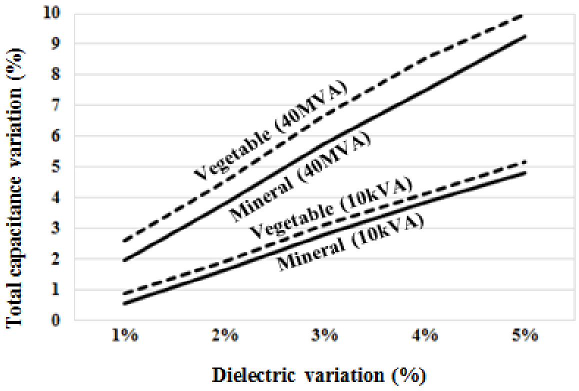

Figure 4-5 Correlation of dielectric factors increases with capacitance of transformer's main insulation system

4:5 Transformer Bushing Simulation using FEA

As shown in Figure 4-6, an oil-filled condenser (otherwise known as an oil-impregnated paper (OIP) bushing) is constructed by winding impregnated paper around a central core and then immersing it in insulation oil.

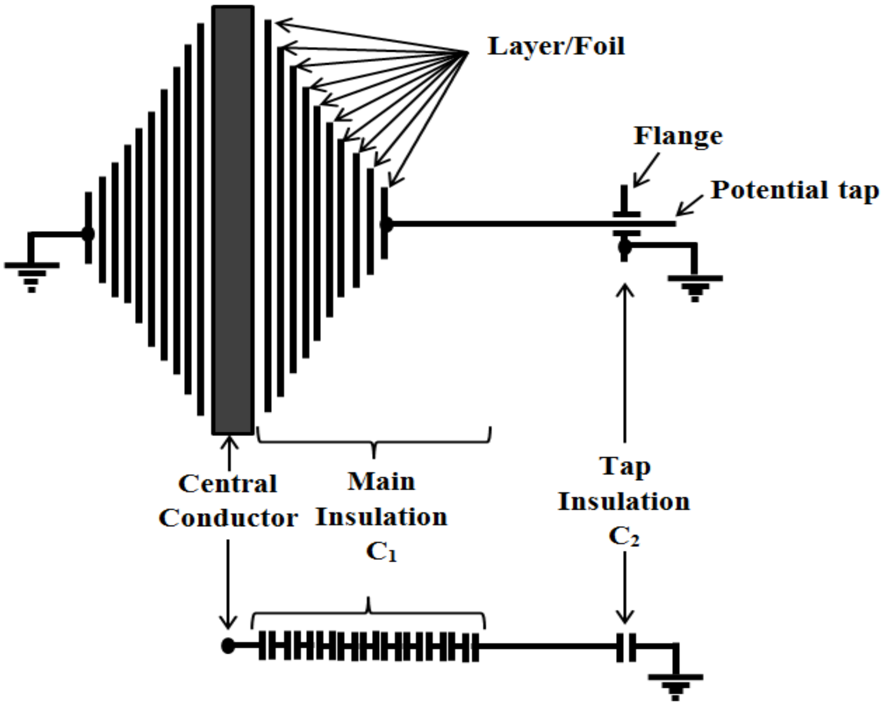

Figure 4-6 Constructive design of an OIP condenser bushing

To equalise the electrical field within the bushing, the insulation of an OIP bushing is made up of several conductive layers. The bushing's earthed flange is connected to the outer conductive layer, while the second outer layer is connected to a potential tap that is used to measure power factor and capacitance of the bushing [105]. Bushing integrity is assessed based on its dielectric capacitance, and any change in capacitance indicates a defect within the bushing [23]. In Figure 4-7, the equivalent electrical circuit of a bushing is represented as a T-shaped model, in which C_1 indicates main insulation capacitance and C_2 represents the capacitance of the two layers close to the flange [105, 106]. The central conductor of the bushing is represented by series resistance and inductance, R_s and L_s, respectively.

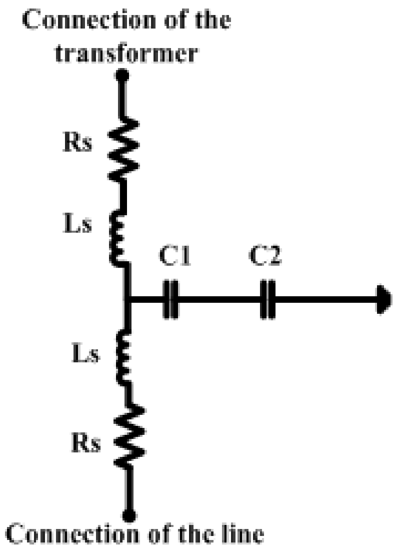

Figure 4-7 Equivalent electrical circuit of OIP condenser bushing

The 3D model of the transformer bushing is simulated using FEA as shown in Figure 4-8.

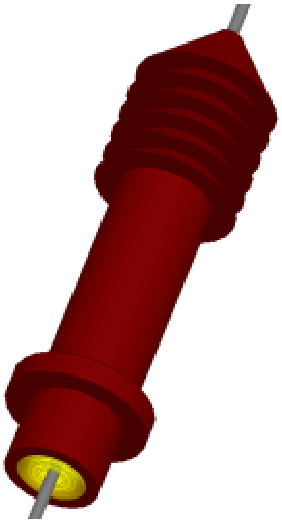

Figure 4-8 3D model of OIP condenser bushing

Figure 4-9 depicts the percentage increase in both capacitive components (C_1 and C_2), attributed to the percentage increment in the insulation dielectric factors (ε_x and σ). It shows a greater effect on C_1 than C_2 [23], meaning that the variation of bushing capacitive components in the 40 MVA transformer is slightly higher than the corresponding variation in the capacitive components of the 10 kVA transformer.

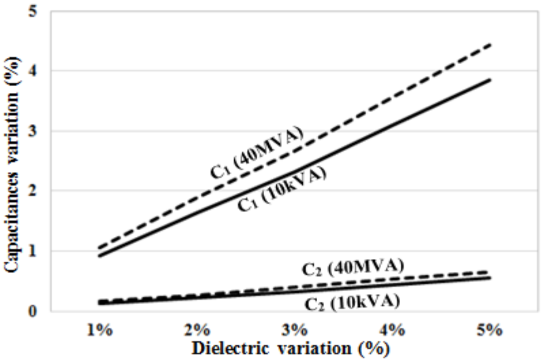

Figure 4-9 Correlation of dielectric factors increment with bushing capacitive components

4:6 Transformer Parameters Calculation using FEA

Magneto-static and electro-static solvers, using Maxwell equations, are applied to the 3D models of the 10 kVA and 40 MVA transformers, in order to extract the capacitance and inductance matrices of the relevant transformer components. The resistance and conductance calculations are carried out by applying eddy current and electric DC conduction solvers as illustrated below:

- The capacitive components calculation is carried out using the electro-static solver, where a voltage v is applied to one conductor and maintained at zero in the other. The electrostatic field energy (w) between the two conductors can be calculated as follows [63, 71]:

  $$W_{ij} = \frac{1}{2}\int_{\Omega} D_i \, E_j d\Omega \qquad (4.8)$$

  where W_{ij} is the electrical field energy between the conductors i and j, D_i is the electrical flux density of conductor i, and E_j is the electrical field intensity of conductor j.

  The capacitance C between two conductors i and j is then calculated as:

  $$C = \frac{2W_{ij}}{v^2} \qquad (4.9)$$

- Inductive components are calculated using the average of magnetic field energy (W_{av}) and the corresponding peak current that passes through the winding (I_p) as shown below [63]:

  $$W_{av} = \frac{1}{4}\int_{m} B \times H \, dm \qquad (4.10)$$

$$L = \frac{4W_{av}}{{I_p}^2} \quad (4.11)$$

where B is the magnetic field density, H is the magnetic field intensity, and m is the conductor volume.

- Resistive components are calculated based on power loss (P_{loss}), which depends on conductor conductivity (σ) and current density (J), as given in (4.10) and (4.11) below:

$$P_{loss} = \frac{1}{2\sigma} \int_m \vec{J}.\vec{J}\, dm \qquad (4.12)$$

$$R = \frac{P_{loss}}{I_{rms}^2} \quad (4.13)$$

The equivalent circuit parameters of the two transformers, including the capacitance, inductance and resistance components, can be then readily calculated and are listed in Table A-4 in the appendix.

4:7 Transformer Representations

The two most commonly used methods for representing the power transformers are electrical circuit representation (ECR) and numerical representation (NR). These methods are described in the following subsections.

4:7:1 ECR Method

The ECR method is frequently used to model power transformers in the form of RLC-lumped or -ladder electric circuits. As previously shown in Figure 3-5, the transformer’s equivalent electrical system parameters — including resistance, self/mutual inductance, capacitance and conductance — are connected to represent a single turn or disk. An overall model of the transformer winding can be simulated by connecting the equivalent circuit of winding turns or disks in series. Several electrical computer-based programs — such as ANSOFT Simplorer, MATLAB Simulink and P-Spice — can be used [89]. In [70, 76], Ansoft Simplorer has been recommended for power transformer modelling and design, because of its proven accuracy in simulating such complex circuits.

4:7:2 NR Method

NR relies on solving a set of first order differential equations that represent transformer windings as a multi-conductor transmission line (MTL) [107]. The MTL technique has been used to study partial discharge and transient voltage distribution within power transformers [108, 109]. For the purpose of FRA study, transformer windings can be simulated as a MTL [110].

MTL modelling of the transformer winding can be described using telegraphic equations in a frequency domain as follows [107, 111]:

$$\frac{\partial}{\partial z}\left(\bar{V}(z,h)\right) = -\bar{\bar{Z}}\,\bar{I}(z,h) \quad (4.14)$$

$$\frac{\partial}{\partial z}\left(\bar{I}(z,h)\right) = -\bar{\bar{Y}}\,\bar{V}(z,h) \quad (4.15)$$

where $\bar{V}(z)$ and $\bar{I}(z)$ represent the voltage and current vectors of a transmission line h, respectively, while $\bar{\bar{Z}}$ and $\bar{\bar{Y}}$ refer to self and mutual impedance and admittance matrices, respectively, that can be defined as:

$$\bar{\bar{Z}} = \bar{\bar{R}} + j\omega\bar{\bar{L}} \quad (4.16)$$

$$\bar{\bar{Y}} = \bar{\bar{G}} + j\omega\bar{\bar{C}} \quad (4.17)$$

As depicted in Figure 4-10, the MTL technique is used to model the transformer winding as a combination of transmission lines and two ports that send and receive electrical signals

The admittance Y-matrix, representing the transformer winding, can be expressed as:

$$\begin{bmatrix} I_s \\ I_r \end{bmatrix} = \begin{bmatrix} Y_{s11} & -Y_{s12} \\ -Y_{r21} & Y_{r22} \end{bmatrix} \begin{bmatrix} V_s \\ V_r \end{bmatrix} \quad (4.18)$$

where:

Y_{s11}=Y_{r22}= Y ($\frac{\xi}{\lambda}$) Coth ($\frac{\lambda l}{\xi}$) and

Y_{s12}=Y_{s21}= Y ($\frac{\xi}{\lambda}$) Csch ($\frac{\lambda l}{\xi}$)

I_s, V_s, I_r and V_r are the current and voltage vectors of the sending and receiving terminals. ξ and λ represent the eigenvectors and eigenvalues of matrix ZY to calculate $Y_{s11}, Y_{s12}, Y_{r21}$ and Y_{r22}. The winding conductor length l is represented as a diagonal matrix of a dimension equal to the number of turns.

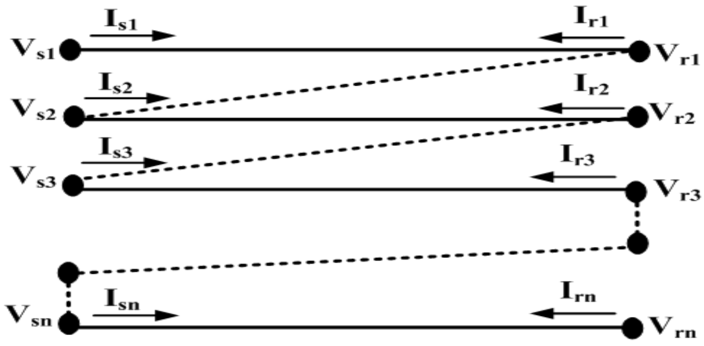

Figure 4-10 MTL model for transformer winding

The transformer winding with (*n*) number of turns is based on (4.18) and represented as:

$$\begin{bmatrix} I_{s1} \\ I_{s2} \\ \vdots \\ I_{sn} \\ I_{r1} \\ I_{r2} \\ \vdots \\ I_{rn} \end{bmatrix} = \left[Y_p\right]_{2n\times 2n} \begin{bmatrix} V_{s1} \\ V_{s2} \\ \vdots \\ V_{sn} \\ V_{r1} \\ V_{r2} \\ \vdots \\ V_{rn} \end{bmatrix} \Longleftrightarrow \begin{bmatrix} V_{s1} \\ V_{s2} \\ \vdots \\ V_{sn} \\ V_{r1} \\ V_{r2} \\ \vdots \\ V_{rn} \end{bmatrix} = \left[Y_p{}'\right]_{2n\times 2n} \begin{bmatrix} I_{s1} \\ I_{s2} \\ \vdots \\ I_{sn} \\ I_{r1} \\ I_{r2} \\ \vdots \\ I_{rn} \end{bmatrix} \qquad (4.19)$$

The input and output voltages “V_{s1} and V_{rn}” of the transformer winding are shown in Figure 4-10 and can be easily calculated based on (4.19) as:

$$V_{s1} = Y'_{1,1} \times I_{s1} + Y'_{1,2n} \times I_{rn} \qquad (4.20)$$

$$V_{rn} = Y'_{2n,1} \times I_{s1} + Y'_{2n,2n} \times I_{rn} \qquad (4.21)$$

FRA practical testing employs input/output co-axial cables of 50Ω, which can be taken into account in the numerical representation (4.22) below:

$$I_{rn} = \frac{V_{rn}}{50} \qquad (4.22)$$

By inserting the solution to equation (4.22) into equations (4.20) and (4.21), the FRA response of the transformer winding modelling, based on NR in the form of transfer function (V_{output}/V_{input}), can be calculated as:

$$V_{s1} = Y'_{1,1} \times I_{s1} + Y'_{1,2n} \times \frac{V_{rn}}{50} \qquad (4.23)$$

$$V_{rn} = Y'_{2n,1} \times I_{s1} + Y'_{2n,2n} \times \frac{V_{rn}}{50} \qquad (4.24)$$

$$\frac{V_{rn}}{V_{s1}} = \frac{V_{out}}{V_{in}} = \frac{Y'_{2n,1} \times 50}{Y'_{1,1} 50 + Y'_{1,1} \times Y'_{2n,2n} + Y'_{2n,1} \times Y'_{1,2n}} \qquad (4.25)$$

4:8 FRA Signatures for the Investigated Transformers

The FRA technique is conducted on the simulation models of two investigated transformers (10 kVA and 40 MVA) by connecting a sweep frequency AC voltage source of low amplitude (10 V) at one terminal of a transformer winding, and then measuring the response signal at the other terminal of the same winding with respect to the earthed tank. This is illustrated in the case studies below.

4:8:1 Case Study 1: 10 kVA Transformer

As shown in Figure 4-11, the measured transfer function of the 10 kVA transformer for each phase within the HV and LV windings is plotted as a magnitude (dB) and phase angle (degrees) against a wide range of frequency (Hz). In this figure, the transformer simulation model is based on the application of the ECR method using ANSOFT Simplorer.

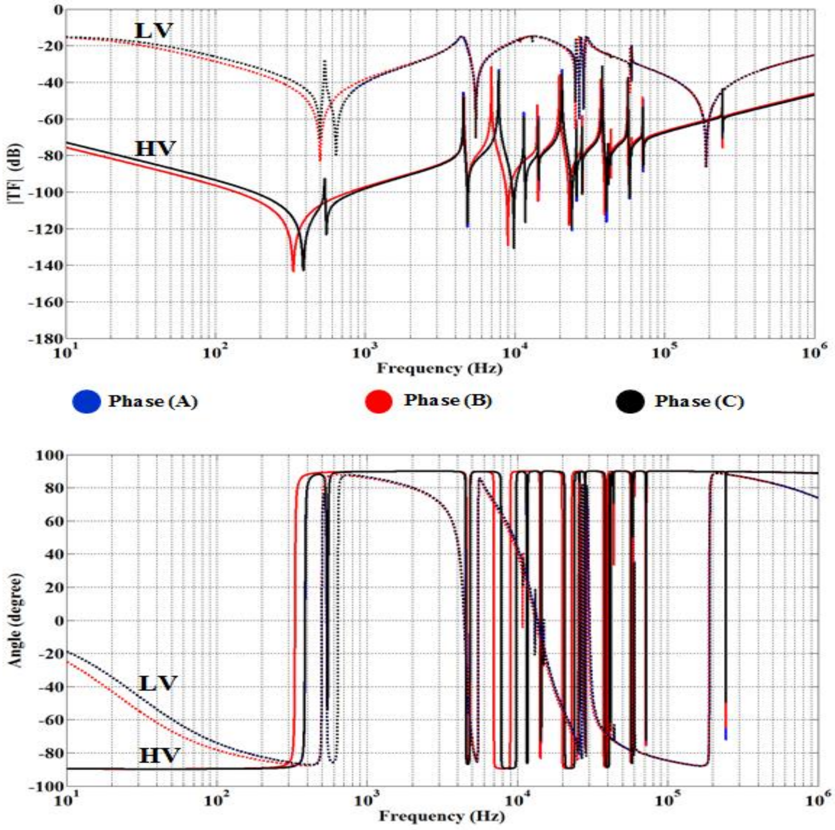

Figure 4-11 Healthy FRA signature of 10 kVA transformer using ECR method

To assess the robustness of the ECR method, a simulation model based on the NR method is used to obtain the FRA signature for the transformer (as shown in Figure 4-12). The NR method is applied by developing a programming code under the MATLAB coding platform to readily solve the MTL technique equations.

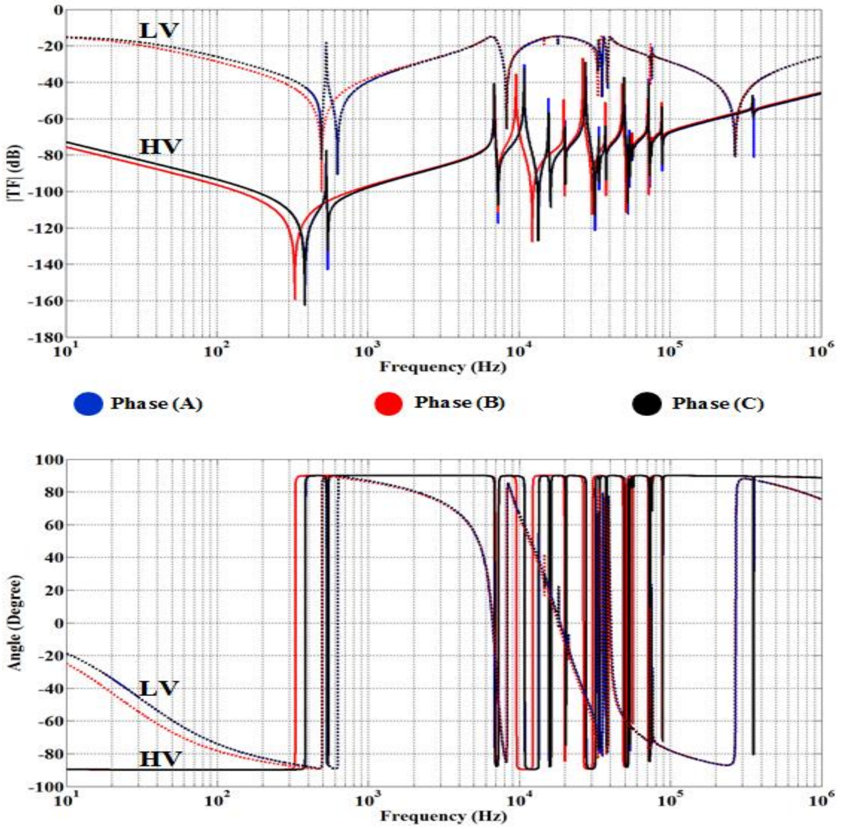

Figure 4-12 Healthy FRA signature of 10 kVA transformer using NR method

As shown in Figures 4-11 and 4-12, the 3-phase FRA signature is characterised by resonance and anti-resonance frequencies along the entire frequency range. As the frequency increases, space harmonics build up in the winding. At a low frequency range, and because flux penetration to the core is significant at this low range, the signature is characterised by the transformer's inductive components. At a high frequency range, the distributed capacitive components tend to shunt the winding inductance. This is shown by the phase angle, which fluctuates around ±90º. Both figures show identical FRA signatures for all three phases within the LV and HV windings, except for the middle phase (red plot) that tends to shift toward the left in the low frequency range. This may be attributed to the slight difference in the magnetic flux of the central limb (phase B), compared to the other two limbs (phases A and C).

Figure 4-13 shows a comparison between the ECR and NR methods, used to obtain FRA signatures for the HV and LV windings of the 10 kVA transformer. As can be seen in this figure, the two methods produce an identical FRA signature in the mid and high frequency range. In the low frequency range, the signature obtained, using NR, shifts slightly to the left. This may be because, in NR modelling, the mutual inductance representation is in most cases lumped with the self-inductance representation [8]. Although both methods are eligible to represent the transformer simulation model, several studies prefer the ECR method. This is due to the professional capabilities of ANSOF Simplorer [70, 76]. This thesis strongly agrees with this idea, because there is better consistency when maintaining simulation modelling analysis (ANSYS Maxwell) and the ECR method (Simplorer) within one-package platform (ANSFOT).

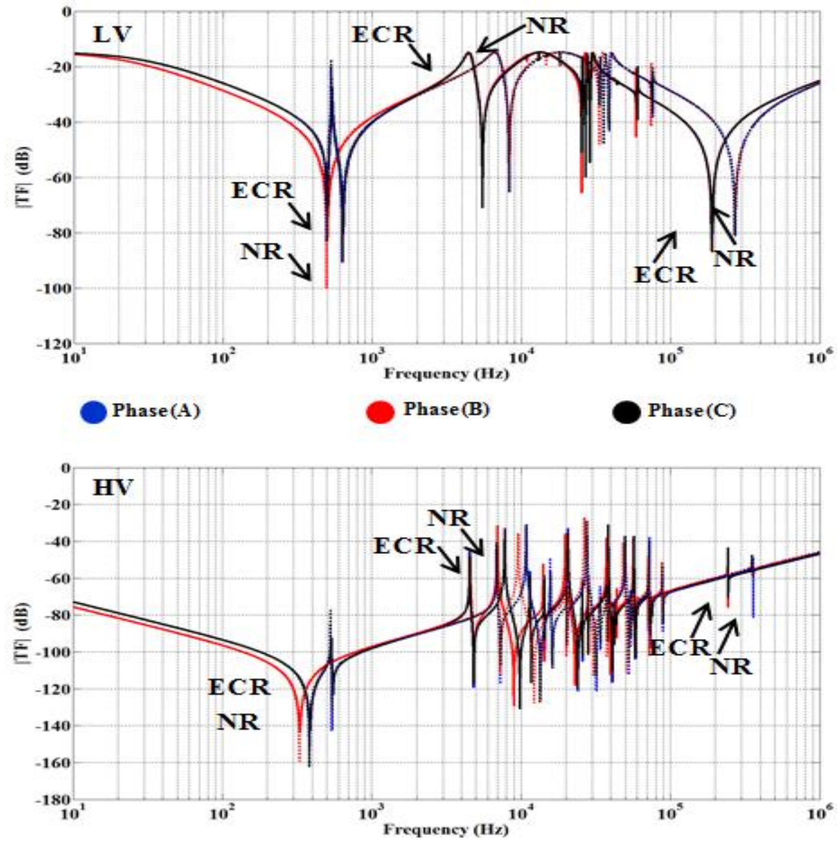

Figure 4-13 Healthy FRA magnitude signature of 10 kVA transformer using ECR and NR methods

4:8:2 Case Study 2: 40 MVA Transformer

As shown in Figure 4-14, the simulated ECR model of the 40 MVA is used to obtain the FRA fingerprint for the HV and LV windings.

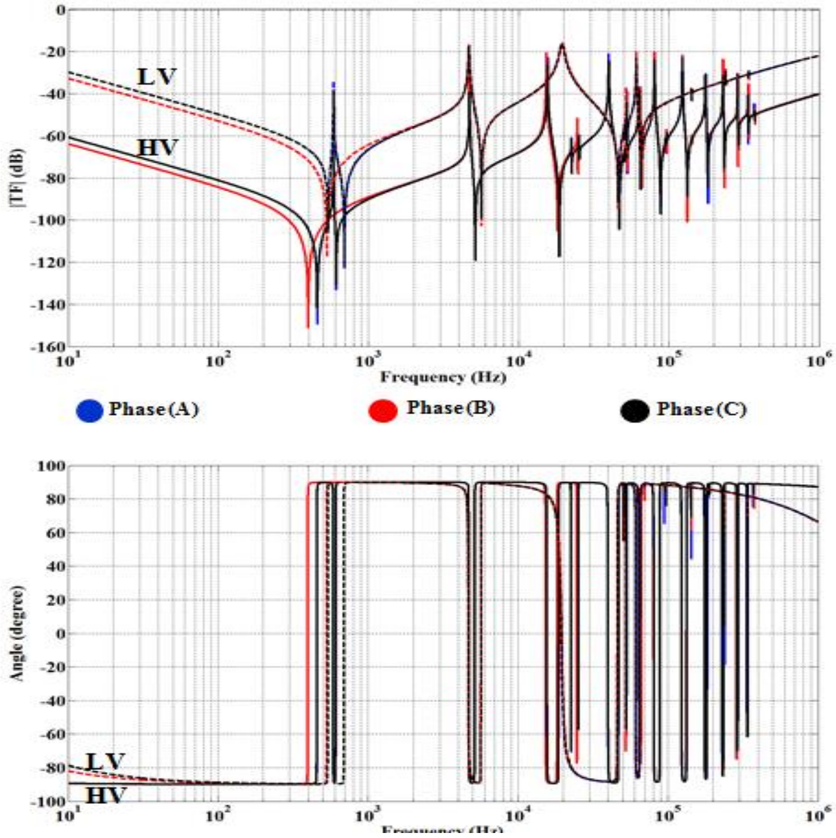

Figure 4-14 Healthy FRA signature of 40 MVA transformer using ECR method

The overall trend of the 40 MVA transformer’s simulated healthy signature is similar to that of the trend of the healthy signature in the 10 kVA simulation model.

Several mechanical and non-mechanical failures can be modelled, using simulation modelling alongside the ECR method, in order to study the impact of these failures on the FRA responses, and also to understand the pros and cons of applying the FRA technique. This idea will be elaborated upon in the following chapter.

Chapter 5 Detection Accuracy of Current FRA Practice

5:1 Introduction

As per previous discussions in Chapters 3 and 4, the FRA signature of a transformer is sensitive to several mechanical and non-mechanical faults. A comprehensive study should, therefore, be conducted in order to determine the accuracy of current FRA practice. This can be achieved by developing a precise simulation model of several power transformers to allow a better understanding of a fault's impact on the FRA signature. Current FRA practice has many shortcomings to be addressed. It relies on an expert technician to interpret the graphical representation, and it uses only the magnitude signature, neglecting the information contained within the phase angle plot. Furthermore, it can be seen that when current FRA practice is applied to detect minor (low) fault levels, its sensitivity should be robustly improved. In this chapter, several mechanical and non-mechanical faults are simulated on two three-phase power transformer FEA models using the ECR method to examine the accuracy of current FRA practice. This study considers the type, level and location impacts of the following faults:

- Short circuit turns
- Radial deformation (free and forced buckling)
- Axial deformation (axial displacement and disk space variation)
- Transformer insulation degradation
- Transformer bushing faults

The simulation studies of the above-mentioned faults create a better understanding of both the advantages and disadvantages of using the FRA technique based on current FRA practice.

5:2 Case Study 1: SC Turns Faults

Using the FEA technique based on ANSYS Maxwell, various fault levels of SC turns within the 10 kVA and 40 MVA transformers' LV and HV windings are simulated by short-circuiting a portion of the selected transformer winding. The SC turns fault level is calculated using the equation below:

$$\%\ \text{SC fault level} = \frac{\text{Number of short circuited turns}}{\text{Total number of turns}} \times 100 \qquad (5.1)$$

5:2:1 LV Winding of the 10 kVA Transformer

Figure 5-1 shows the impact of five minor SC fault levels (1% to 5%) and an exaggerated fault level (40%) within phase A of the LV winding using the current FRA approach. As previously discussed, the current FRA approach only considers the 10 kVA transformer's FRA magnitude signature. Figure 5-1 also reveals that the impact of minor SC fault levels on the FRA magnitude signature is difficult to detect using visual inspection. The impact of an exaggerated SC level can, however, be easily distinguished.

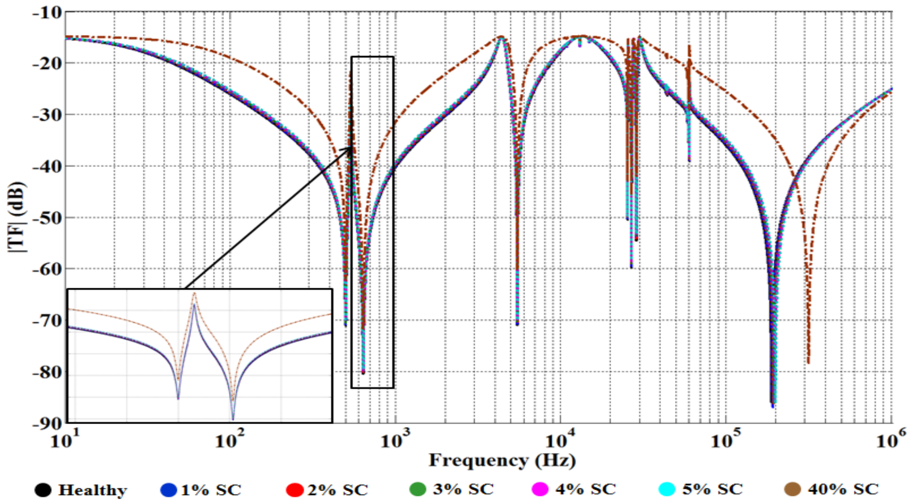

Figure 5-1 Impact of SC faults using current FRA practice on the 10 kVA transformer's LV winding phase A

5:2:2 HV Winding of the 10 kVA Transformer

FRA signatures are also obtained when SC faults of various levels (1% to 5%, and 40%) are applied to phase A of the HV winding. Based on the winding structure of the 10 kVA, previously discussed in Chapter 4, this type of fault is assumed to take place in several different places within the HV winding: in the top disk (Disk 1), middle disk (Disk 3), and bottom disk (Disk 6).

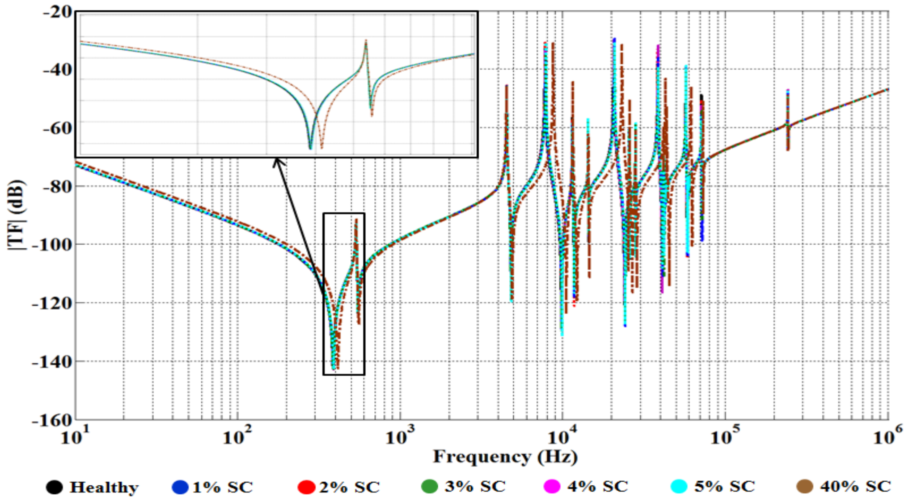

Figure 5-2 Impact of SC turns faults using current FRA practice on the 10 kVA transformer's HV winding phase A in the top disk (Disk 1)

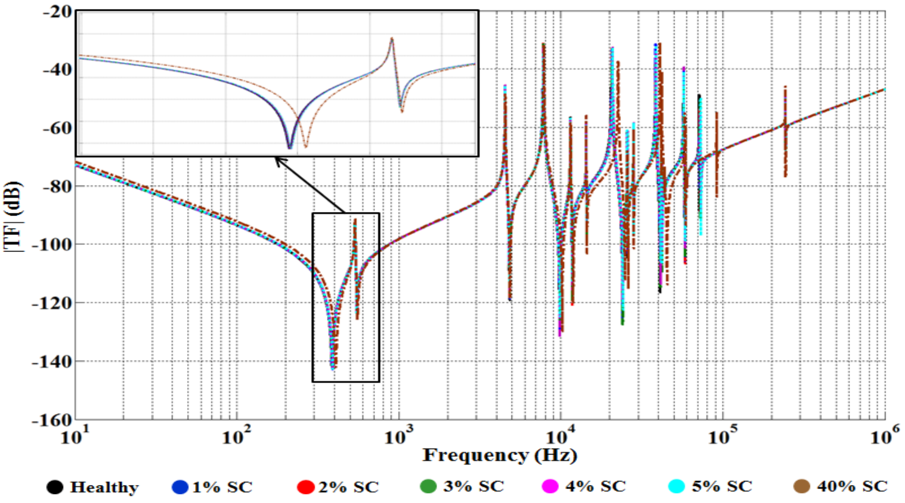

Figure 5-3 Impact of SC turns faults using current FRA practice on the 10 kVA transformer's HV winding phase A in the middle disk (Disk 3)

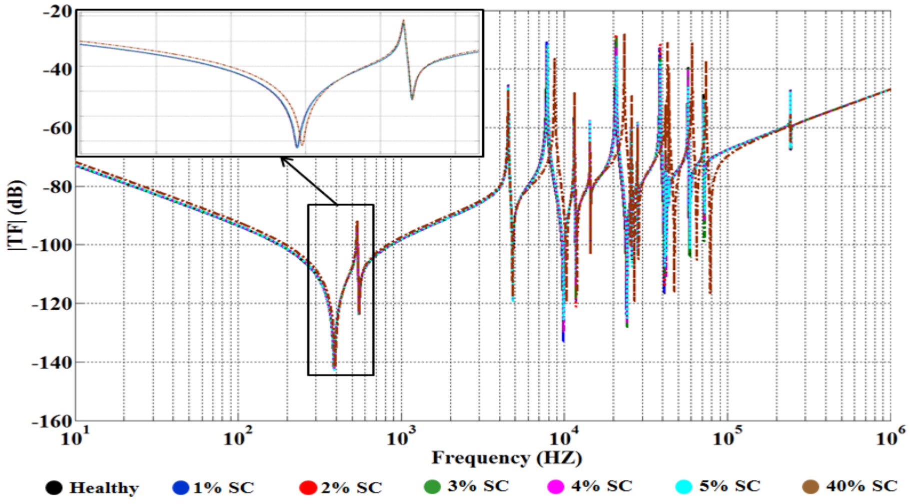

Figure 5-4 Impact of SC turns faults using current FRA practice on the 10 kVA transformer's HV winding phase A in the bottom disk (Disk 6)

The impact of an SC fault at various levels (1% to 5%, and 40%) and in different locations (top, middle and bottom disks) is shown in Figures 5-2, 5-3 and 5-4, respectively. The above figures reveal that current FRA practice is unsuccessful in identifying and quantifying the levels and locations of minor SC faults (less than 5%).

5:2:3 LV Winding of the 40 MVA Transformer

This subsection considers the impact of the transformer's rating, size, and winding structure. Using the FEA technique and ECR method, a simulation model of SC turn faults on a higher transformer rating (40 MVA) is conducted. The same SC fault levels (1% to 5%, and 40%) are implemented on phase A of the 40 MVA transformer's LV winding to obtain the FRA signatures shown in Figure 5-5.

Just as in previous observations, the impact of minor SC fault levels on the LV winding of the 40 MVA transformer are hard to detect when applying current FRA practice. Once again, the exaggeration level is readily detected by a visual inspection.

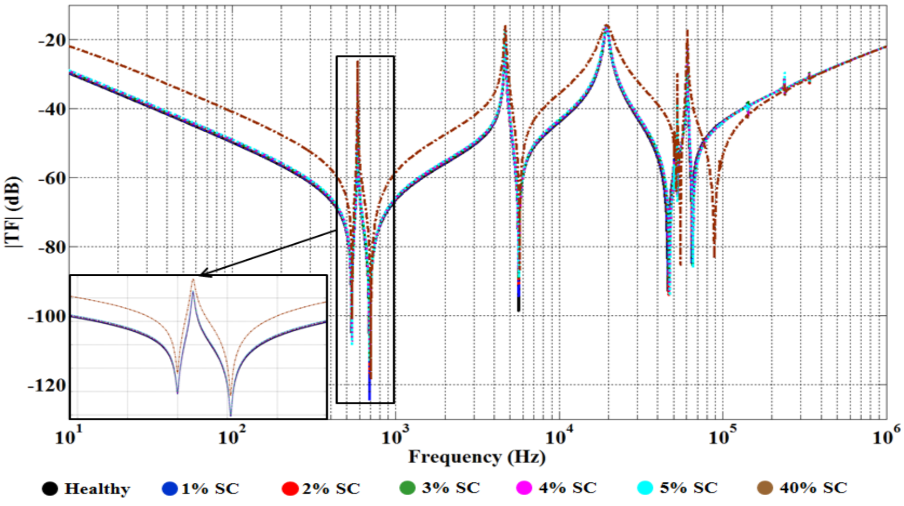

Figure 5-5 Impact of SC turns faults using current FRA practice on the 40 MVA transformer's LV winding phase A

5:2:4 HV Winding of the 40 MVA Transformer

According to the information given in Chapter 4, regarding the specifications and dimensions of the transformers under study in this thesis, the HV winding of the 40 MVA transformer consists of 10 disks per phase. The SC fault of various levels is applied to the top disk (Disk 1), middle disk (Disk 5) and bottom disk (Disk 10). The impact of the different fault levels and locations using the FRA technique based on current practice is illustrated in Figures 5-6 (SC fault is located in the top disk), 4-7

(SC fault is located in the middle disk) and 4-8 (SC fault is located in the bottom disk).

Just as in the previous case studies, the detection of incipient SC fault levels at different locations is extremely hard to detect using current FRA practice, as shown in the following figures.

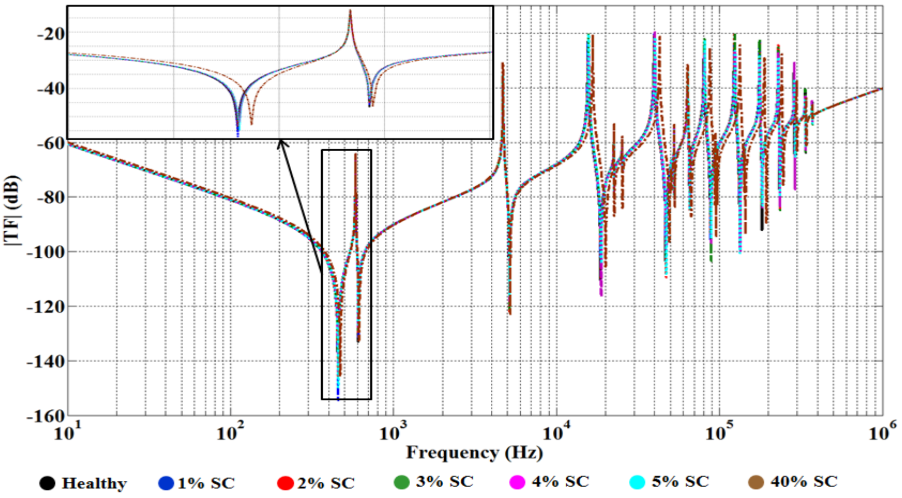

Figure 5-6 Impact of SC turns faults using current FRA practice on the 40 MVA transformer's HV winding phase A in the top disk (Disk 1)

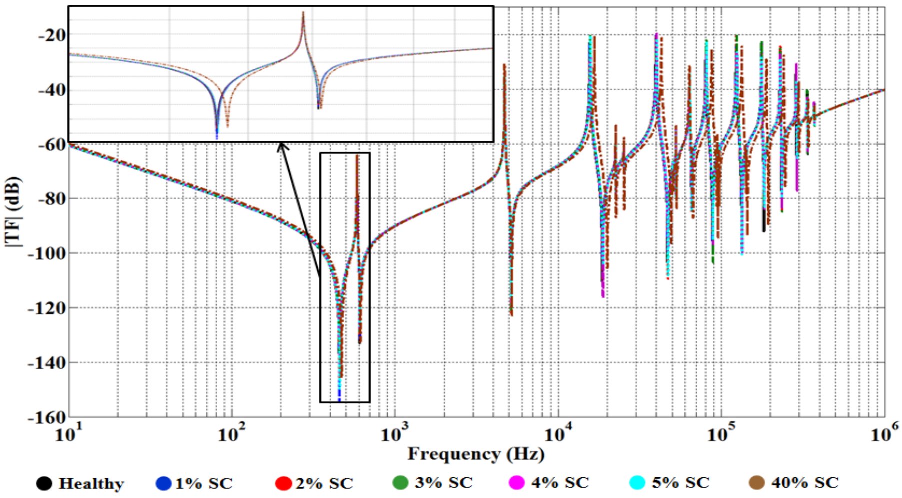

Figure 5-7 Impact of SC turns faults using current FRA practice on the 40 MVA transformer's HV winding phase A it the middle disk (Disk 5)

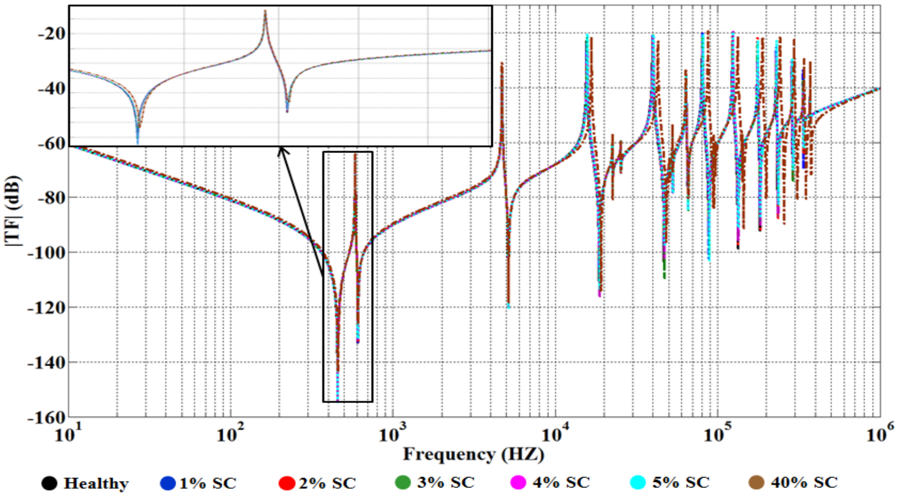

Figure 5-8 Impact of SC turns faults using current FRA practice on the 40 MVA transformer's HV winding phase A it the bottom disk (Disk 10)

5:3 Case Study 2: Radial Faults

Radial forces on transformer windings are generated by the interaction of SC currents and magnetic flux. Upon exceeding certain limits, these forces may lead to winding radial deformation [1, 76]. Excessive radial forces generate a tensile stress that pushes the outer winding towards the tank (free radial buckling). The inner winding is subjected to compressive stress that pushes the winding inward (forced radial buckling) [76]. As a result of forced radial buckling, the conductor bends in alternate spans, while free radial buckling causes a bulge at one or more edges of the conductor [76]. Buckling deformations are simulated on the two investigated transformers using FEA, as shown in Figures 5-9 and 5-10, respectively.

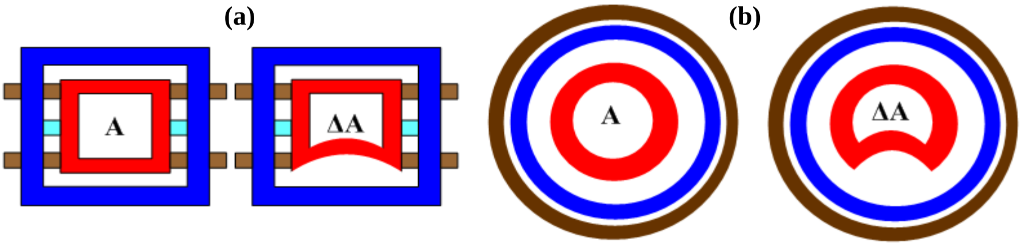

Figure 5-9 Top view of healthy and forced radial buckling on the LV winding: (a) 10 kVA, (b) 40 MVA

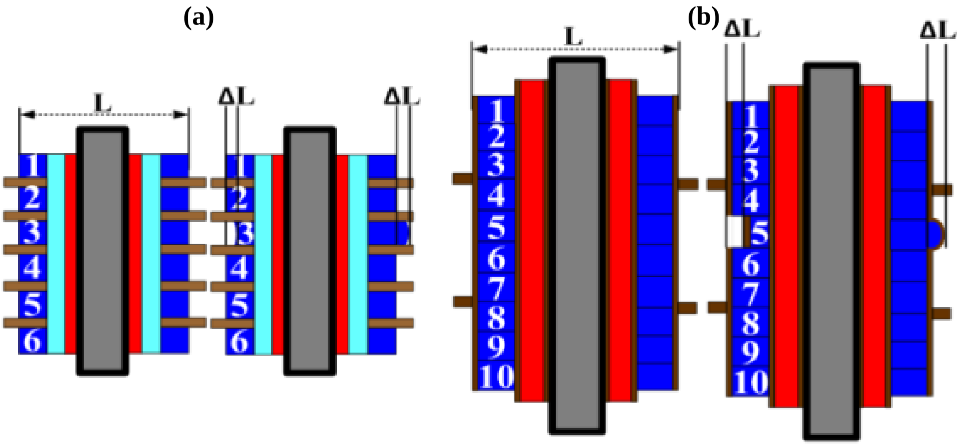

Figure 5-10 Front view of healthy and free radial buckling on the HV winding: (a) 10 kVA (Disk 3) and (b) 40 MVA (Disk 5)

The fault levels of forced and free radial buckling, which are shown in the above figures, are calculated based on the following equations:

$$\text{Forced radial buckling} = \frac{\text{area of deformed section } (\Delta A)}{\text{healthy cross section area } (A)} \times 100\% \qquad (5.2)$$

$$\text{Free radial buckling} = \frac{\text{Radial length } (\Delta L)}{\text{disk length } (L)} \times 100\% \qquad (5.3)$$

5:3:1 Forced Radial Buckling (10 kVA Transformer)

The FEA technique is used to simulate five minor fault levels (1% to 5%) and an exaggerated fault level (40%) of forced radial buckling within phase A of the 10 kVA transformer’s LV winding.

The impact of the investigated fault levels on the LV winding based on current FRA practice is shown in Figure 5-11. It reveals the difficulty in identifying minor fault levels of forced radial buckling. The impact of 40% fault level, however, is clearly distinguishable from the healthy signature.

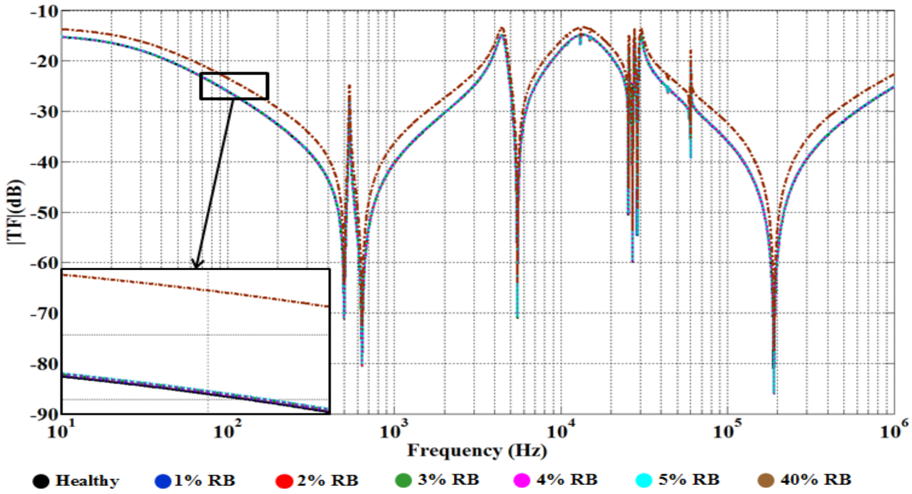

Figure 5-11 Impact of forced radial buckling faults using current FRA practice on the 10 kVA transformer's LV winding phase A

5:3:2 Free Radial Buckling (10 kVA Transformer)

Using FEA, free radial buckling faults are simulated on phase A of the 10 kVA transformer's HV winding at three different locations, including the top disk (Disk 1), middle disk (Disk 3) and bottom disk (Disk 6), and also at various fault levels (1% to 5%, and 40%).

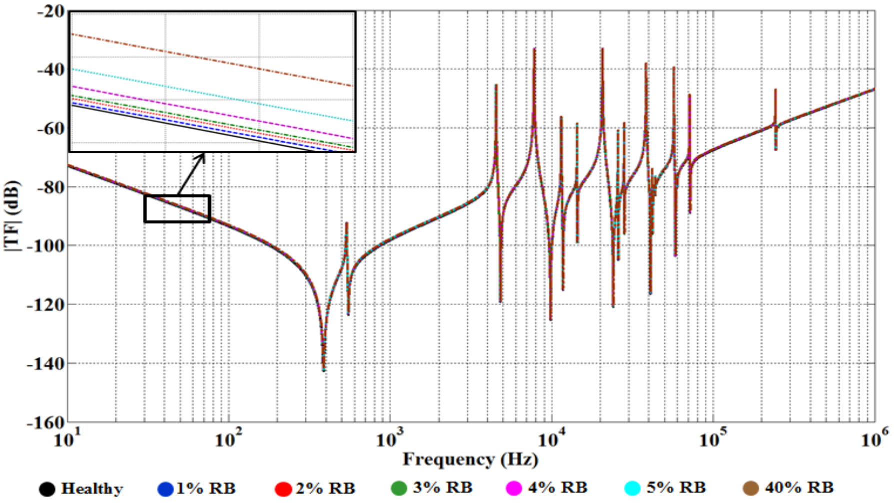

Figure 5-12 Impact of free radial buckling faults using current FRA practice on the 10 kVA transformer's HV winding phase A in the top disk (Disk 1)

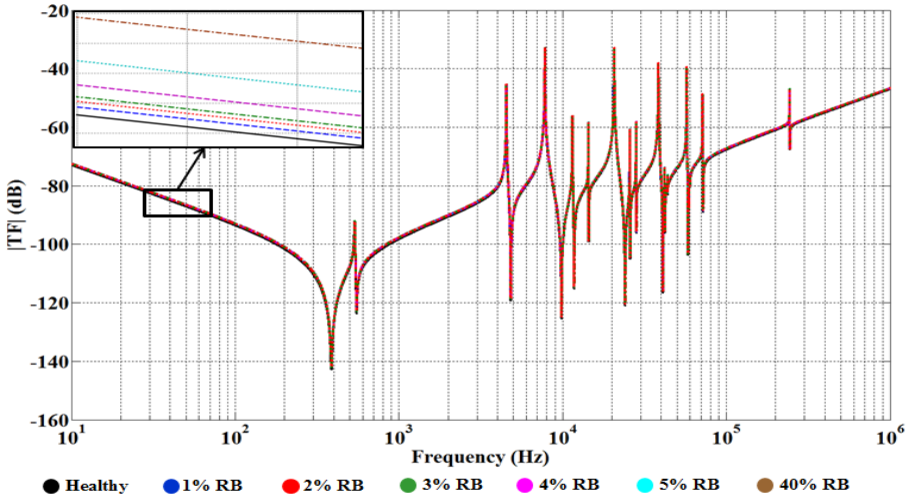

Figure 5-13 Impact of free radial buckling faults using current FRA practice on the 10 kVA transformer's HV winding phase A in the middle disk (Disk 3)

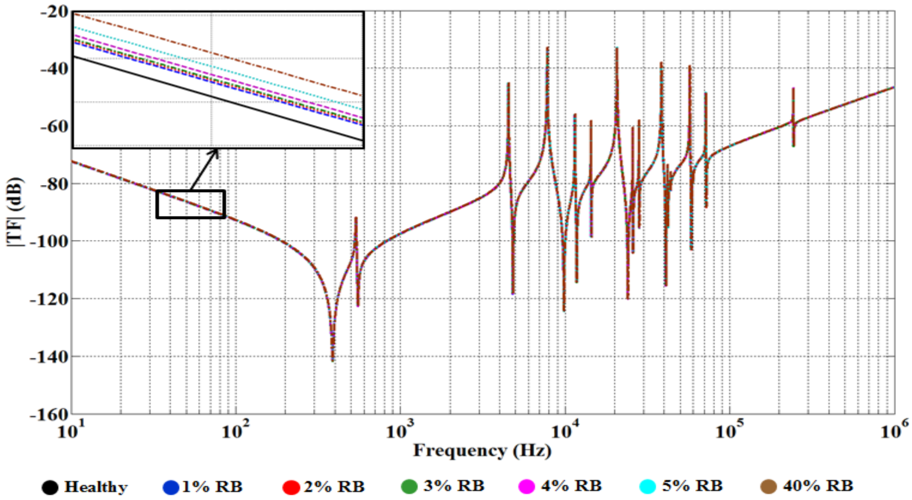

Figure 5-14 Impact of free radial buckling faults using current FRA practice on the 10 kVA transformer's HV winding phase A in the bottom disk (Disk 6)

As can be seen in Figures 5-12 (fault in top disk), 5-13 (fault in middle disk) and 5-14 (fault in bottom disk), the impact of such minor fault levels using current FRA practice reveals the drawbacks of this approach when identifying the incipient fault's location as well as its level.

5:3:3 Forced Radial Buckling (40 MVA Transformer)

The impact of the transformer's rating, size and winding structure, along with forced radial buckling faults on phase A of the 40 MVA transformer's LV winding, is investigated by simulating five minor levels (1% to 5%) and an exaggerated fault level (40%) using the FEA technique and ECR method (Figure 5-15). As has been observed in all previous case studies, current FRA practice is incapable of detecting minor fault levels up to 5%.

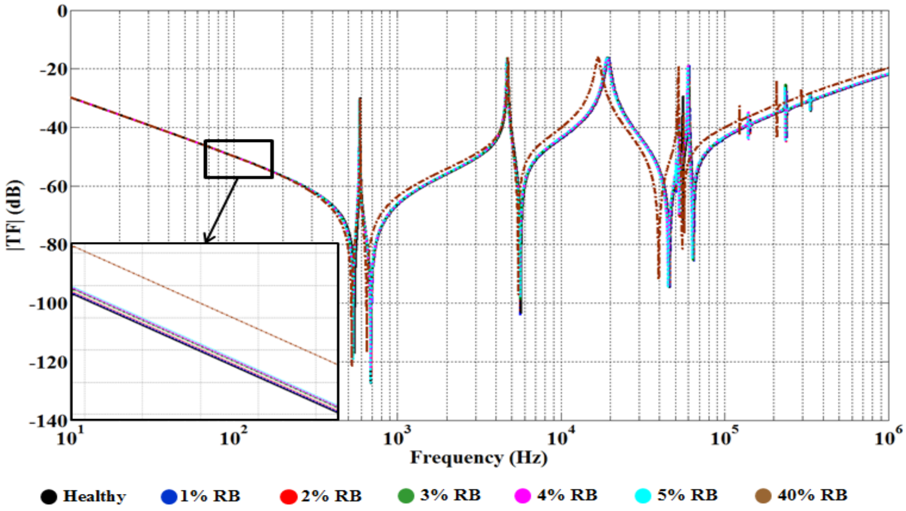

Figure 5-15 Impact of forced radial buckling faults using current FRA practice on the 40 MVA transformer's LV winding phase A

5:3:4 Free Radial Buckling (40 MVA Transformer)

In this case study, free radial buckling at various fault levels is simulated on the top disk (Disk 1), middle disk (Disk 5) and bottom disk (Disk 10) of the 40 MVA HV winding. As can be seen in Figures 5-16, 5-17 and 5-18, it is difficult to report the level and location of free radial buckling at low fault levels.

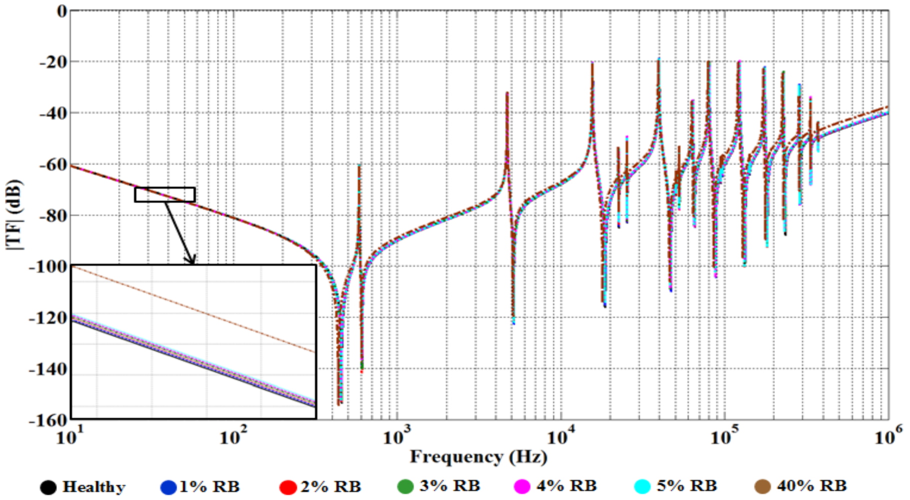

Figure 5-16 Impact of free radial buckling faults using current FRA practice on the 40 MVA transformer's HV winding phase A in the top disk (Disk 1)

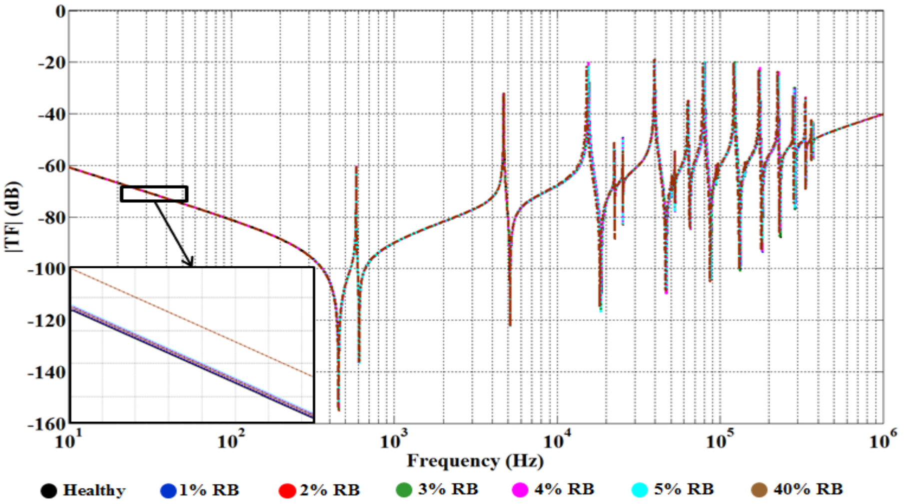

Figure 5-17 Impact of free radial buckling faults using current FRA practice on the 40 MVA transformer's HV winding phase A in the middle disk (Disk 5)

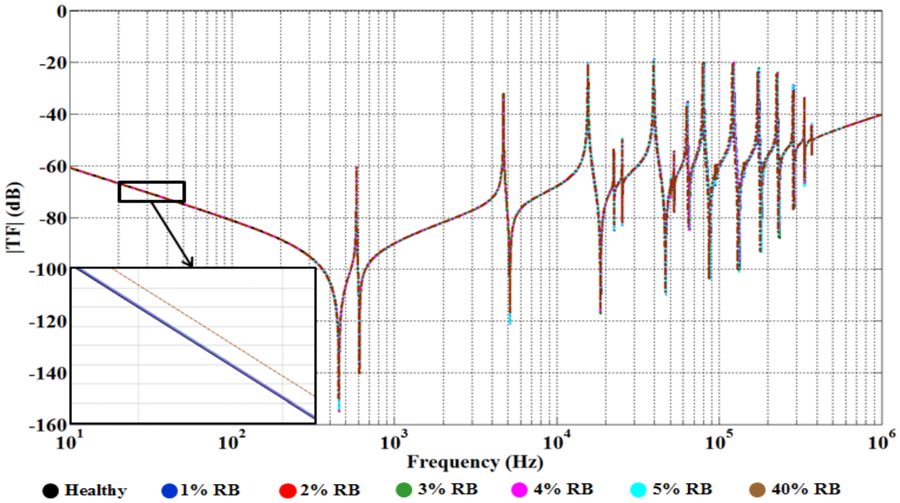

Figure 5-18 Impact of free radial buckling faults using current FRA practice on the 40 MVA transformer's HV winding phase A in the bottom disk (Disk 10)

5:4 Case Study 3: Axial Displacement Faults

Axial displacement (AD) of the transformer winding may be a result of imbalanced magnetic forces between the HV and LV windings due to short circuit faults [1, 58, 112]. The FEA technique is employed to simulate AD and DSV faults on the 10 kVA and 40 MVA transformer models. Figure 5-19 shows a schematic diagram for the AD fault within phase A of the HV and LV windings of both investigated transformers. Figure 5-20 shows the configuration for a DSV fault within the HV winding of both transformers. The level of AD and DSV faults are calculated using (5.4) and (5.5), respectively.

$$\%\ \text{AD Fault level} = \frac{\text{Axial displacement length } (\Delta\text{H})}{\text{Winding height (H)}} \times 100\% \qquad (5.4)$$

$$\%\ \text{DSV Fault level} = \frac{\text{Disk space variation length } (\Delta\text{h})}{\text{Disk height (h)}} \times 100\% \qquad (5.5)$$

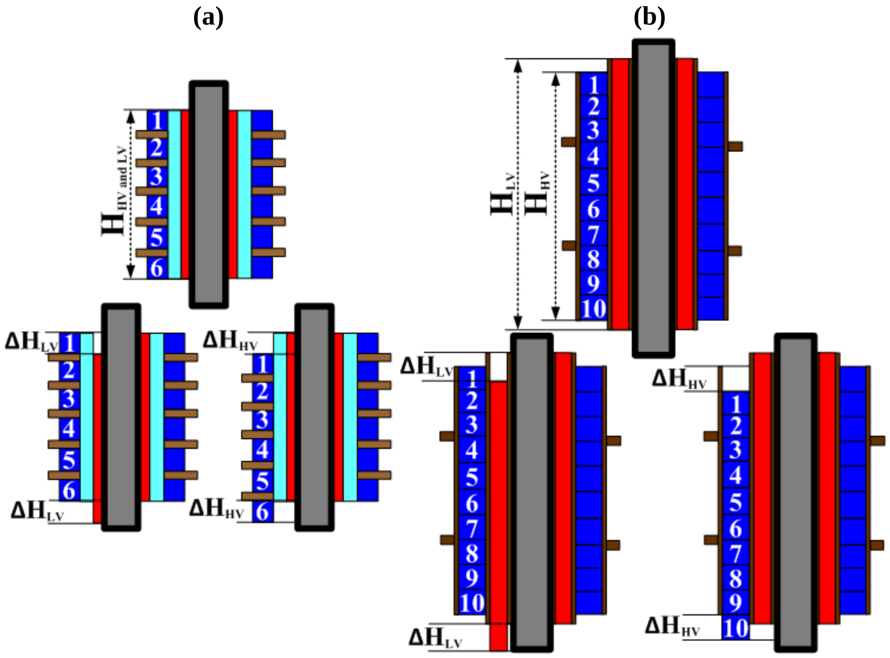

Figure 5-19 Front view of healthy and AD fault conditions of HV and LV windings: (a) 10 kVA and (b) 40 MVA

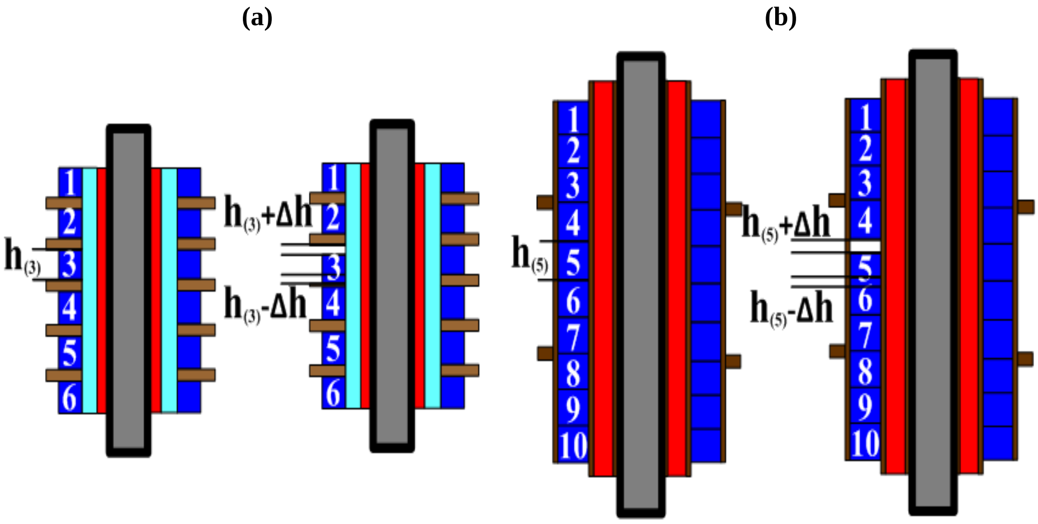

Figure 5-20 Front view of healthy and DSV fault conditions of HV winding: (a) 10 kVA and (b) 40 MVA

5:4:1 Axial Displacement (10 kVA Transformer)

Five minor levels (1% to 5%) of AD fault within phase A of the 10 kVA transformer's HV and LV windings are simulated using the FEA technique. The impact of these faults using current FRA practice is shown in Figures 5-21 and 5-22, respectively. These figures also reveal the difficulty of the current FRA approach to detect such minor AD faults.

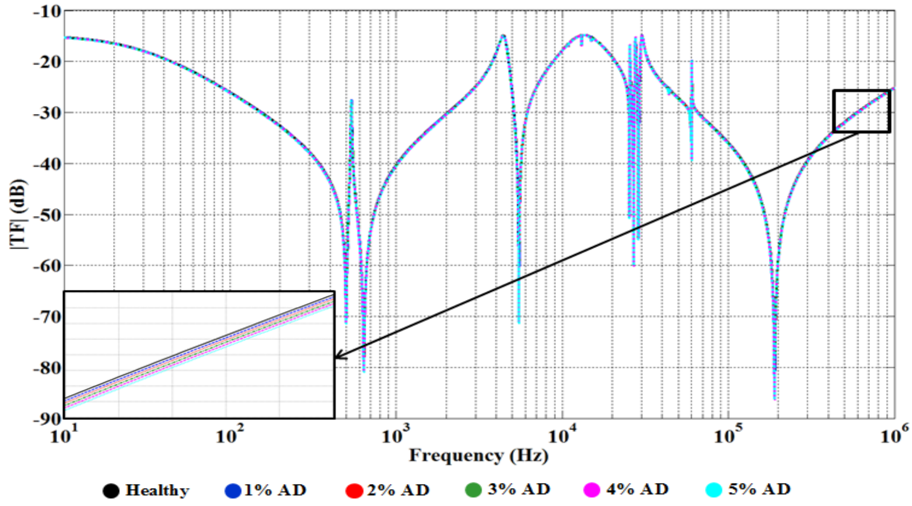

Figure 5-21 Impact of AD faults using current FRA practice on the 10 kVA transformer's LV winding phase A

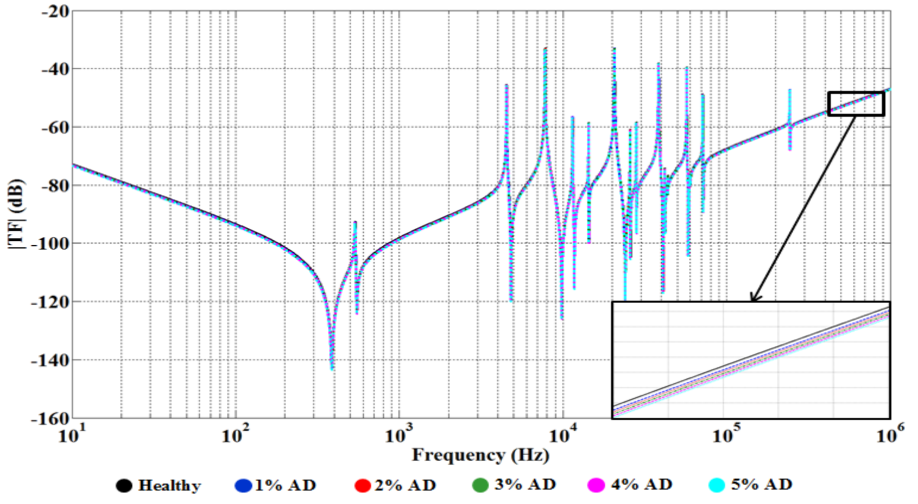

Figure 5-22 Impact of AD faults using current FRA practice on the 10 kVA transformer's HV winding phase A

5:4:2 Axial Displacement (40 MVA Transformer)

AD faults with five minor levels (1% to 5%) are simulated using FEA on phase A of the 40 MVA transformer's LV and HV windings. The FRA signature obtained for each fault level is shown in Figures 5-23 and 5-24, respectively. Just as in previous case studies, the impact of minor AD fault levels within the 40 MVA transformer's LV and HV windings are extremely hard to detect using the current FRA approach.

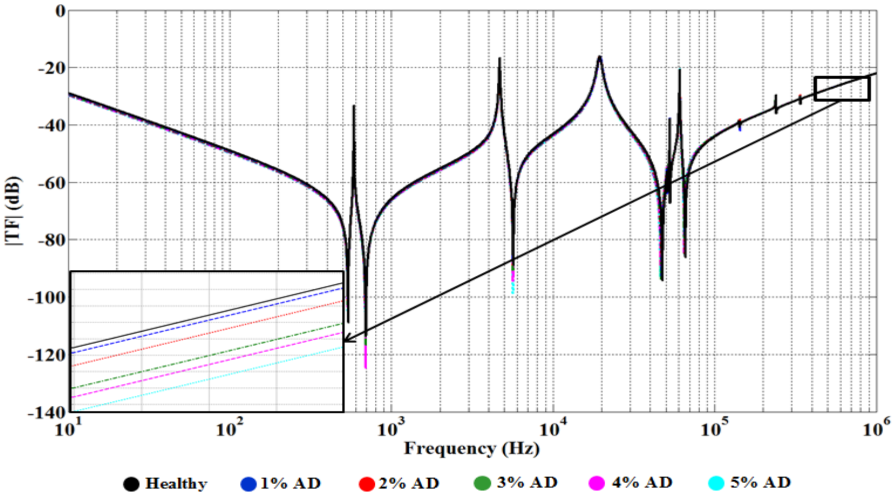

Figure 5-23 Impact of AD faults using current FRA practice on the 40 MVA transformer's HV winding phase A

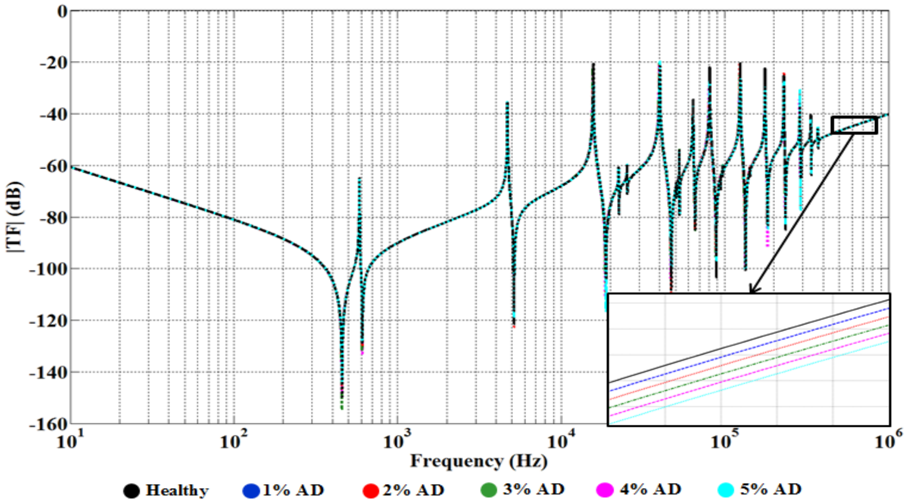

Figure 5-24 Impact of AD faults using current FRA practice on the 40 MVA transformer's HV winding phase A

5:4:3 Disk Space Variation (10 kVA Transformer)

A DSV fault is simulated at different locations within phase A of the 10 kVA transformer's HV winding. Three locations, including in the top disk (Disk1), middle disk (Disk 3) and bottom disk (Disk 6), as well as five minor fault levels (1% to 5%) are simulated using the FEA technique and ECR method.

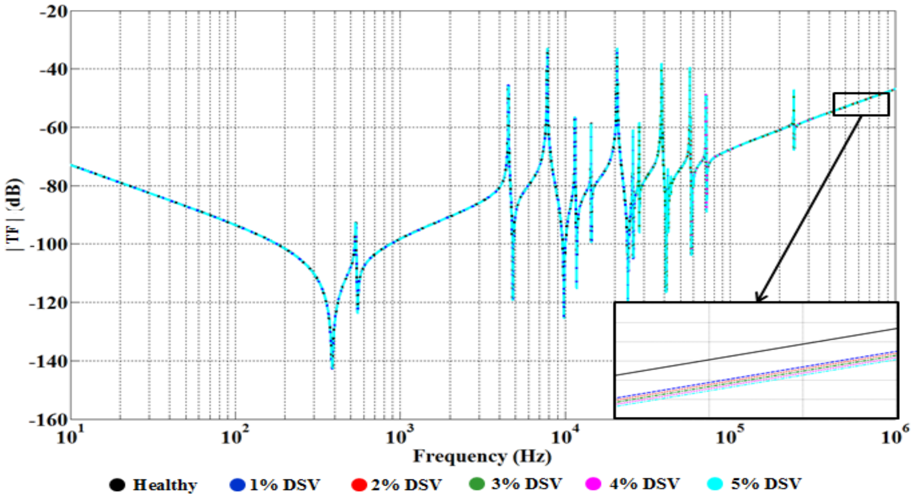

Figure 5-25 Impact of DSV faults using current FRA practice on the 10 kVA transformer's HV winding phase A in the top disk (Disk 1)

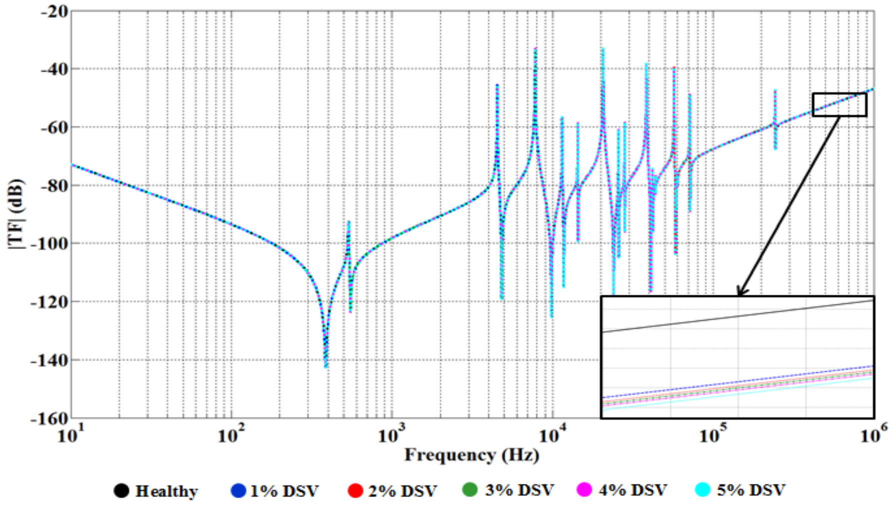

Figure 5-26 Impact of DSV faults using current FRA practice on the 10 kVA transformer's HV winding phase A in the middle disk (Disk 3)

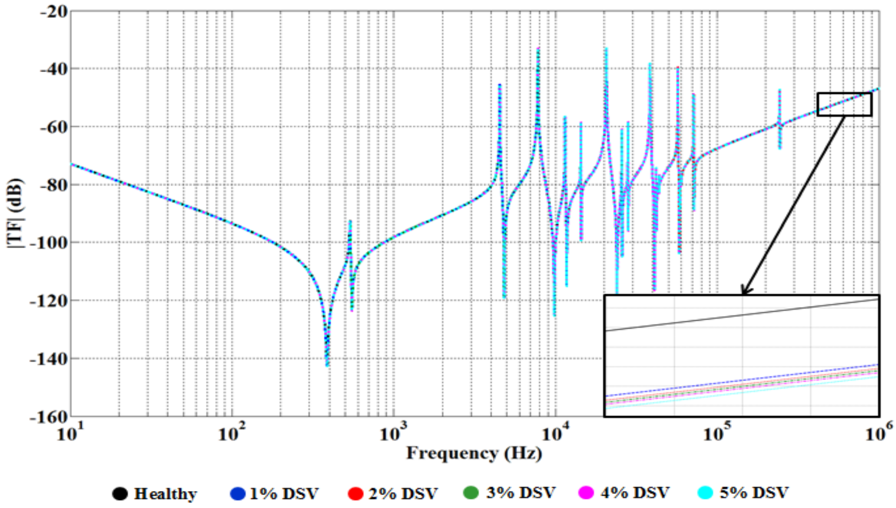

Figure 5-27 Impact of DSV faults using current FRA practice on the 10 kVA transformer's HV winding phase A in the bottom disk (Disk 6)

Figures 5-25, 5-26 and 5-27 show the impacts of the investigated DSV fault levels and locations on the 10 kVA transformer using current FRA practice. Just as in the AD case studies, minor DSV faults are extremely difficult to identify and quantify using the current approach.

5:4:4 Disk Space Variation (40 MVA Transformer)

DSV at minor fault levels are simulated in various locations of the 40 MVA transformer's HV winding, including in the top disk (Disk 1), middle disk (Disk 5) and bottom disk (Disk 10). As shown in Figures 5-28, 5-29 and 5-30, the same difficulty with applying the current FRA approach to detect minor DSV faults can be recognised.

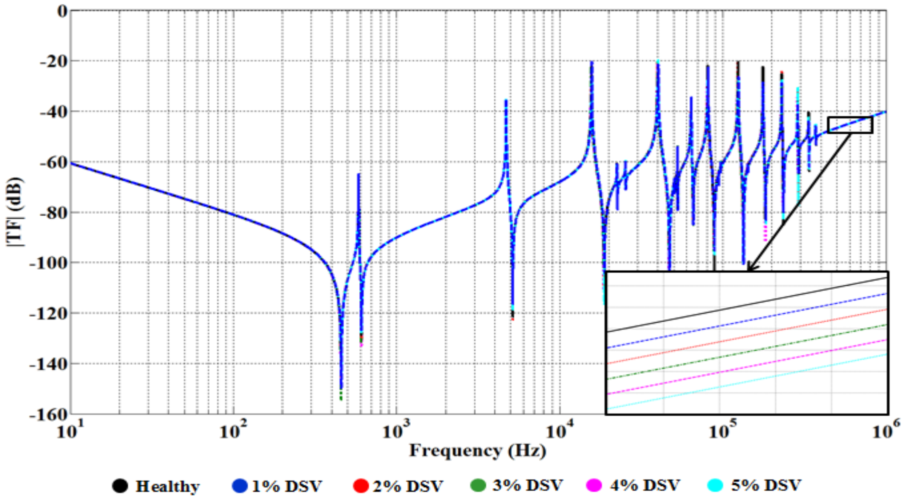

Figure 5-28 Impact of DSV faults using current FRA practice on the 40 MVA transformer's HV winding phase A in the top disk (Disk 1)

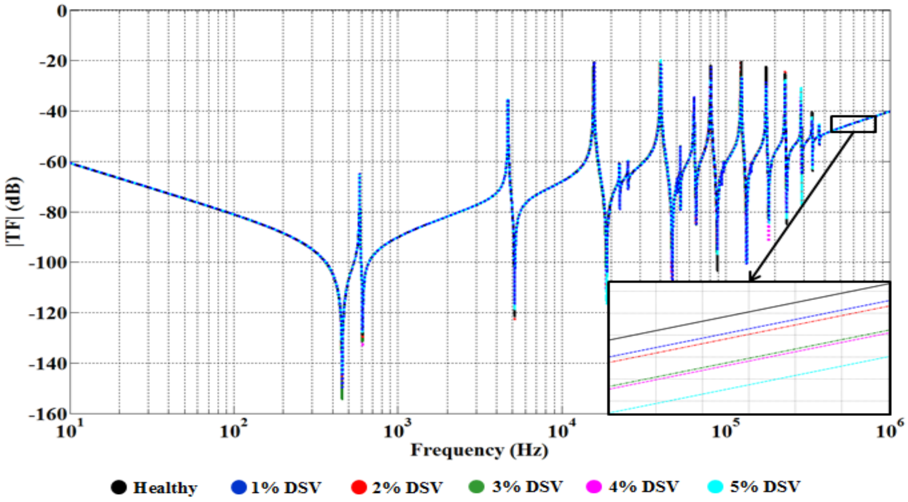

Figure 5-29 Impact of DSV faults using current FRA practice on the 40 MVA transformer's HV winding phase A in the middle disk (Disk 5)

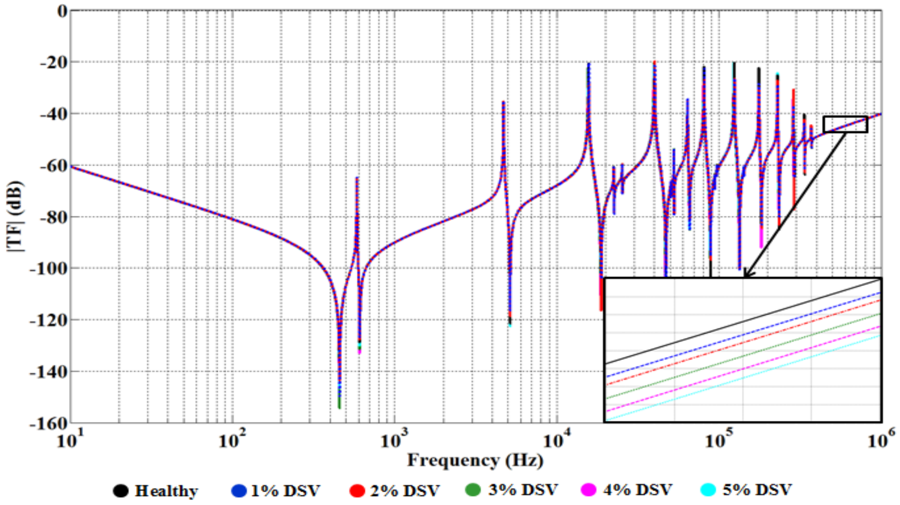

Figure 5-30 Impact of DSV faults using current FRA practice on the 40 MVA transformer's HV winding phase A in the bottom disk (Disk 10)

5:5 Case Study 4: Bushing Faults

Bushing failures are commonly attributed to the deterioration of a transformer's interior insulation materials [26]. As stated in Chapter 4, the moisture content of the 10 kVA and 40 MVA transformers' interior bushings can be changed by increasing the dielectric factors (permittivity and conductivity) [23]. Using the FEA technique, small bushing faults levels are simulated by increasing the bushing insulation's complex permittivity and electrical conductivity by 1% to 5%. These simulations are based on the obtained correlation illustrated in Chapter 4 (Figure 4-9). Figures 5-31 and 5-32 show the impact of changing complex permittivity and electrical conductivity on the FRA signature of the 10 kVA and 40 MVA transformers' HV windings. While a slight change in the FRA signature is observed within the high frequency range, interpretation of such a change is challenging. Furthermore, misinterpretation may refer this change to a different fault type or location.

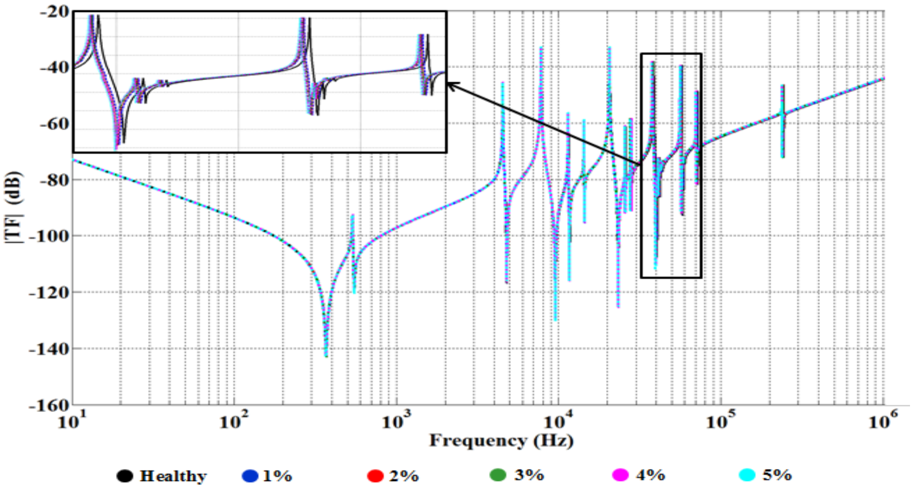

Figure 5-31 Impact of minor fault levels on 10 kVA transformer's HV bushing using current FRA practice

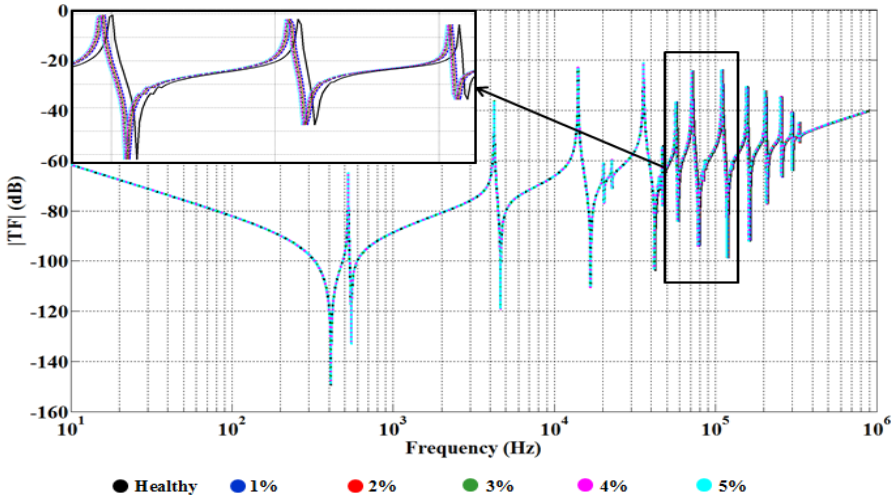

Figure 5-32 Impact of minor fault levels on 40 MVA transformer's HV bushing using current FRA practice

5:6 Case Study 5: Insulation System Degradation

This case study investigates the impact of the insulating oil type/degradation on the transformer using the FRA technique. This is because the FRA technique has previously been shown as sensitive to the health condition and type of insulating oil used within the transformer [23]. Using the FEA technique, various insulating mineral and vegetable oil degradation levels are simulated by changing the oil dielectric factors ε_x and σ from 1% to 5% based on the obtained correlation illustrated in Chapter 4 (Figure 4-5). The impact of minor mineral and vegetable oil fault levels on the 10 kVA and 40 MVA transformers' HV windings using current FRA practice is shown in Figure 5-33 to 5-36.

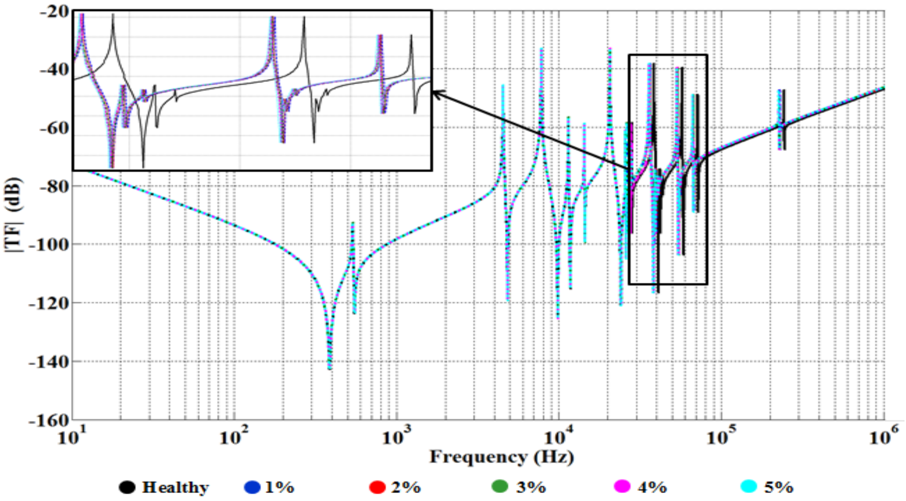

Figure 5-33 Impact of minor mineral oil degradation levels on the 10 kVA transformer's HV winding using current FRA practice

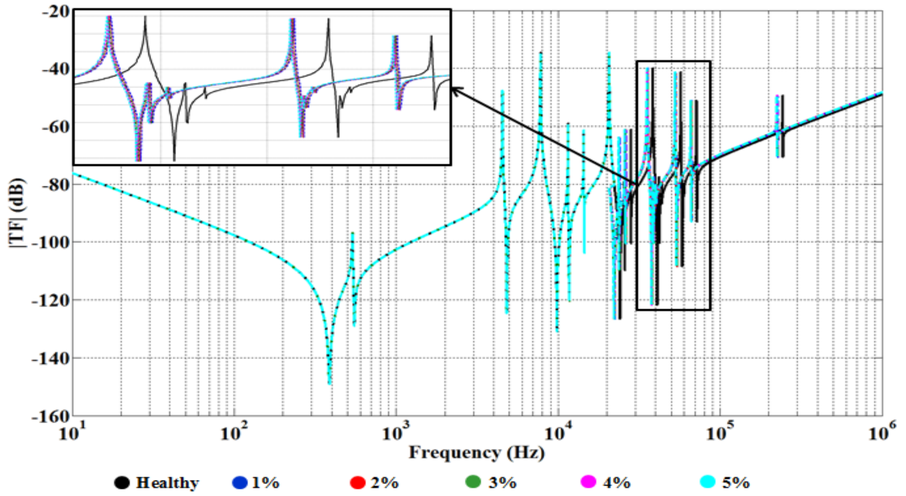

Figure 5-34 Impact of minor vegetable oil degradation levels on the 10 kVA transformer's HV winding using current FRA practice

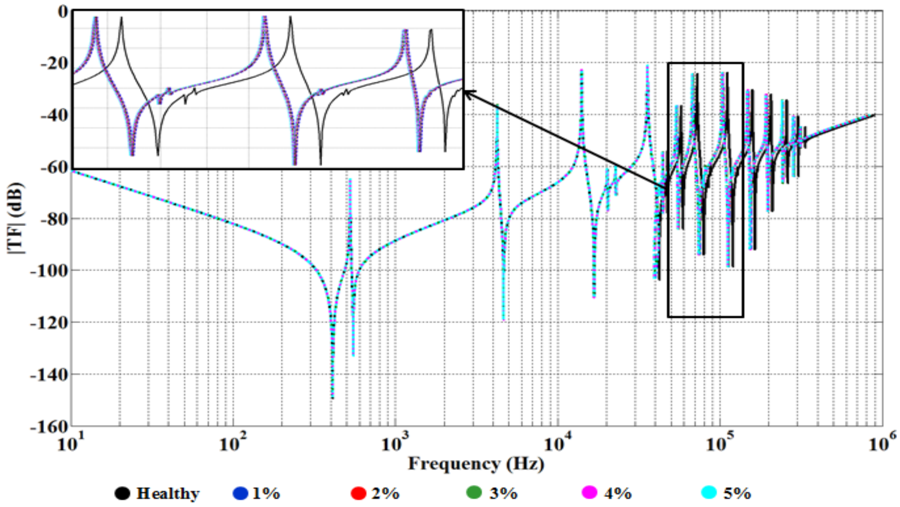

Figure 5-35 Impact of minor mineral oil degradation levels on the 40 MVA transformer's HV winding using current FRA practice

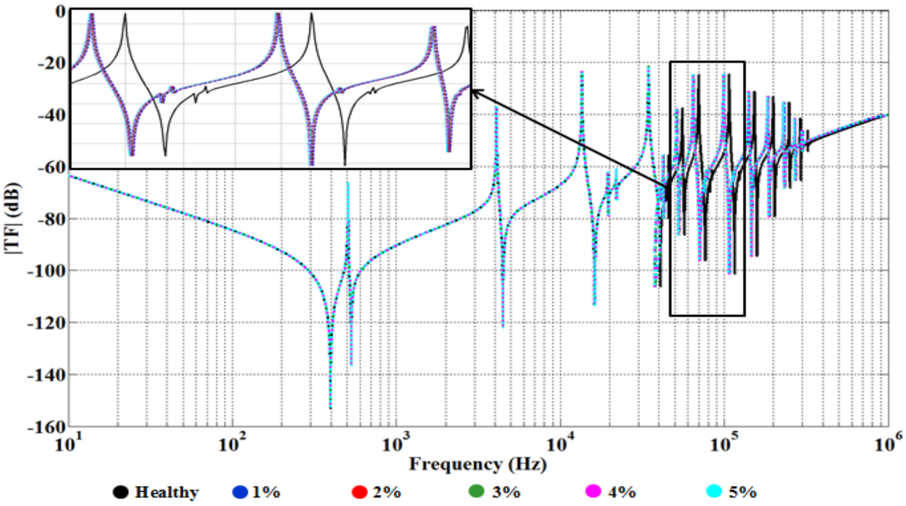

Figure 5-36 Impact of minor vegetable oil degradation levels on the 40 MVA transformer's HV winding using current FRA practice

Although the current FRA approach does show slight variations in the high frequency range due to insulating oil degradation, it is extremely difficult to analyse and refer to these variations as oil degradation. This is because the impact of a bushing fault shows a similar trend at this frequency range.

5:7 Challenges of Current FRA Practice

According to the above case studies, current FRA practice is unable to distinguish between healthy and fault signatures with minor fault levels (up to 5%). The results obtained clearly show the limitations of using the current FRA approach to identify and quantify minor mechanical and non-mechanical faults within power transformer windings. Moreover, the obtained FRA signatures must still be interpreted by expert personnel. This may lead to different conclusions for the same FRA signature. The aim of the new approach is to overcome some of these drawbacks and limitations, and this will be discussed in the following chapter.

Chapter 6 Proposed Approach for Detecting Mechanical and Non-Mechanical Faults

6:1 Introduction

As stated in previous chapters, the main drawbacks and limitations of the FRA technique, which include its incapability with detecting minor fault levels and the absence of a standard interpretation code for the measured FRA signature, have not yet been addressed. The proposed approach in this thesis takes advantage of recent technological advancements in Digital Image Processing (DIP) techniques. Three DIP techniques are developed to manipulate measured FRA signals and describe the pictorial information by extracting key unique features of the images. These features are analysed using numerical computer-based subroutines to calculate three DIP metrics used to automate and standardise the FRA interpretation process. In order to develop the proposed application accurately, the FRA response signals need to be represented in a new format. All commercial FRA analysers can measure the transfer function of the FRA test in the form of magnitude and phase angles against a wide frequency range. However, this thesis proposes the use of DIP techniques to form a new FRA signature by combining these magnitude and phase angle plots into one polar plot. This new approach will provide an automated and detailed report, including the fault type, level and location (if the fault exists).

6:2 Polar Plot Approach

As demonstrated in Chapter 4, the FRA technique is applied to the 10 kVA and 40 MVA transformer simulation models to measure the transfer function for each phase within the HV and LV windings. The measured TF is then plotted as magnitude (dB) and phase angle (degrees) in a wide frequency range (Hz) as illustrated in Chapter 4 (Figures 4-11 and 4-14). These two figures describe the healthy FRA signatures for both simulation models of the 10 kVA and 40 MVA transformers, which are identified by resonance and anti-resonance frequencies over the entire frequency range. These resonance frequencies are influenced by the transformer's inductive components in the low frequency range. They are also affected by the capacitive components in the high frequency range, which can be observed in the phase angle plot that fluctuates around $\pm 90^o$.

Current FRA practice relies only on the FRA magnitude signature for fault diagnosis by comparing it with the transformer fingerprint. If the fingerprint is not available, the FRA magnitude signature is compared to the signature of a sister transformer, or phase to phase comparison is used. As this approach relies on visual graphical analysis, the process is not always consistent and, when analysed by different personnel, may lead to different conclusions for the same FRA signature.

To standardise, automate and improve the detection accuracy of current FRA practice, a new approach is proposed based on the incorporation of the magnitude and phase angle signatures in one polar plot as shown in Figure 6-1. By definition, the polar plot of a transfer function $\mathbf{TF(j2\pi f)}$ is constructed with polar coordinates, and based on its magnitude $\mathbf{|TF(j2\pi f)|}$ and phase angle $\mathbf{\angle TF(j2\pi f)}$ as the frequency $\mathbf{f}$

fluctuates from zero to infinity [113-115]. The points on the proposed polar plot provide three different types of information regarding the measured FRA signature: 1) the magnitude r, which is measured from the origin O, which is a fixed point of reference for the geometry of the surrounding space in the polar plot at zero frequency, 2) the phase angle **θ**, which is measured with respect to the x-axis, and 3) a particular frequency value **f** (varying from 10 to 1 MHz) [113, 114]. While the polar plot is constructed in a 2D plane, the frequency is inherently represented by this set of values: the transfer function magnitude and the phase angle at a specific frequency value as illustrated in Figure B-1 and Table B-1 in the appendix. The proposed polar plot image exhibits more features than the magnitude plot image. This means an improvement in detection accuracy, also facilitating the use of DIP techniques that will enable the automation and standardisation of FRA interpretation. Figure 6-1 reveals that the polar plots of the three phases within the HV and LV windings each have a similar total area and contour perimeter. In the case of the HV windings, they are increasing, which may be attributed to the difference in the design of the LV and HV windings. It can be also seen that the 40 MVA transformer is characterised by a larger total area and a longer contour than that of the 10 kVA transformer. This is due to differences in the transformers' ratings and physical dimensions.

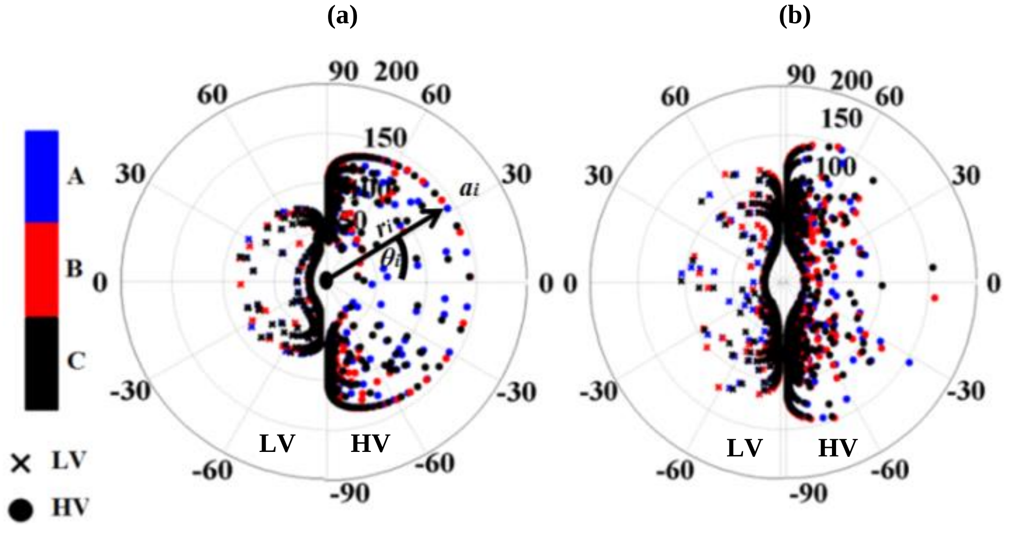

Figure 6-1 Polar plot signatures for a healthy transformer condition: (a) 10 kVA and (b) 40 MVA transformers

6:3 Digital Image Processing Techniques

Digital image processing (DIP)-based techniques are gaining more popularity in application, due to their ability to significantly enhance interpretation accuracy of pictorial information [116, 117]. In such techniques, a digital image [*A*] is represented as a 2D matrix ($M \times N$), which is comprised of a finite number of digital values (pixels). Any point on the proposed polar plot is represented as $a(i, j)$, where $|a|$ represents the image intensity at (a) point, which has a spatial location of (i,j) in respect to the (X,Y) coordinates. To automate and standardise the proposed technique, the obtained FRA polar plots (Figure 6-1) are manipulated using various DIP techniques. Unique features are then extracted, which can be used to characterise the transformer's polar plot signature [117].

In this thesis, image features — such as geometric dimensions, invariant moment, and texture analysis — are extracted from the polar plot image using DIP techniques as per the flow chart in Figure 6-2 [118-120].

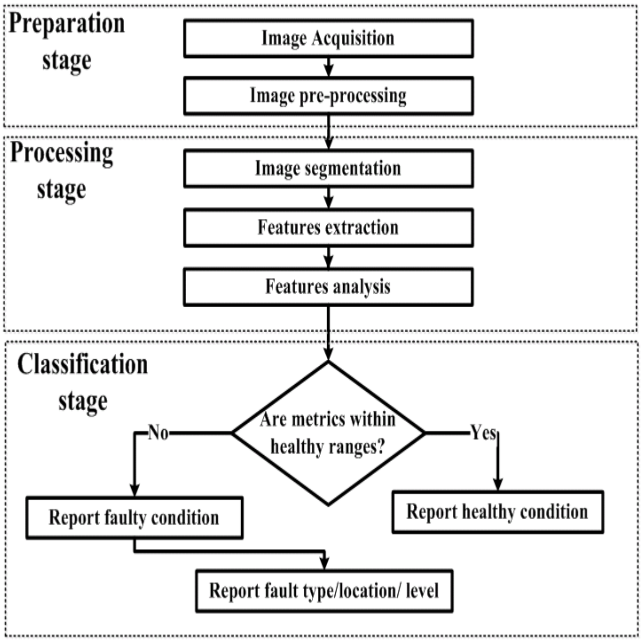

Figure 6-2 Flow chart of the proposed DIP technique

In the flow chart of Figure 6-2, the pre-processing stage is aimed at adjusting image dimension size, colour format, and extension type to assist the image sensor in electronic systems [117, 121].

A segmentation process is used to divide the image into several parts, eliminating unwanted effects, such as image noise and background, and revealing the required object within the image using edge detection algorithms, such as the improved Canny edge detector [122, 123]. The detected FRA polar plot is manipulated to extract four geometric dimension features and 11 combined features using invariant moment and texture analysis techniques [118, 120]. The extracted features are analysed to calculate three unique metrics: city-block distance (CBD), root mean square (RMS) and image Euclidean distance (IED) as below [124].

$$CBD = \sum_{i=1}^{4} |faulty\ feature_i - healthy\ feature_i| \qquad (6.1)$$

$$RMS = \sqrt{\frac{1}{11}\sum_{i=1}^{11} feature_i^2} \qquad (6.2)$$

$$IED = \sqrt{\sum_{i=1}^{11}(faulty\ feature_i - healthy\ feature_i)^2} \qquad (6.3)$$

Similar to the current FRA approach, the three metrics are to be calculated for all new transformers and used as a reference dataset for future comparison.

The classification process shown in Figure 6-2 is aimed at identifying fault type, level, and location within the investigated transformer through comparing polar plot extracted features with the reference dataset [124].

The geometric dimension technique extracts four features from the polar plot image, including entire area (g_1), outer contour perimeter (g_2), centroid coordinates (g_3), and the length of minor and major axes of the outer contour (g_4). These features are based on the equations listed in Table C-1 in the appendix [117, 119, 125, 126].

The invariant moment is a powerful DIP technique as the seven extracted features are independent of the image scale, rotation, and translation [120, 127]. The seven features of the invariant moment technique are measured from order moment (m_{pq}), central moment (μ_{pq}), and normalised moment (η_{pq}) of the image function $f(x,y)$ based on Equations (6.4), (6.5) and (6.6), respectively [120, 128, 129]. The formulas used to calculate the invariant moment features are listed in Table C-2 in the appendix.

$$m_{pq} = \iint_{-\infty}^{\infty} x^p y^q \, f(x,y)dxdy \qquad (6.4)$$

where: $(p+q)^{\text{th}}$: order moment m_{pq} of the image function $f(x,y)$

$$\mu_{pq} = \iint_{-\infty}^{\infty} (x-\bar{x})^p (y-\bar{y})^q \, f(x,y)dxdy \qquad (6.5)$$

$$\eta_{pq} = \frac{\mu_{pq}}{\mu_{00}^{\gamma}} \qquad (6.6)$$

where: $\bar{x} = \frac{m_{10}}{m_{00}}$, $\bar{y} = \frac{m_{01}}{m_{00}}$, $\gamma = \frac{p+q}{2} + 1$

The texture analysis technique can provide information about the intensity of the investigated polar plot signature. Four texture features are extracted from the processed image, including 1) the correlation feature (τ_1), which measures the correlation between the pixel and its neighbours over the entire image, 2) the homogeneity feature (τ_2), which measures the spatial closeness of the image distribution elements to the diagonal elements, 3) the contrast feature (τ_3), which calculates the contrast between the pixel and its neighbour over the entire image, and 4) the energy feature (τ_4), which measures entire image uniformity [118, 130, 131]. Table C-3 in the appendix lists the equations of the texture analysis technique.

The FRA polar plot signatures of the healthy HV and LV windings of the two investigated transformers (Figure 6-1) are manipulated using the developed DIP techniques. Geometric dimension, invariant moment and textures analysis techniques are used to extract four physical features and 11 combined features, as listed in Tables 6-1 and 6-2, respectively. The four geometric dimension features are used to calculate the CBD metric, while the 11 combined features are used to calculate the other two metrics, RMS and IED, based on Equations (6.1), (6.2) and (6.3).

Table 6-1 Geometric dimension features of healthy HV and LV windings in both transformers

Feature		10 kVA transformer		40 MVA transformer	
		HV	LV	HV	LV
g_1		30443	9600	66091	47692
g_2		878.70	493.15	1837.44	1473.07
g_3	X-axis	358.85	339.95	673.65	673.10
	Y-axis	289.88	289.91	612.83	560.22
g_4	Major	374.85	221.58	834.53	642.54
	Minor	109.41	59.24	199.37	127.23

As shown in Table 6-1, the four extracted features, which represent the physical dimensions of the investigated polar plot of the HV winding, are higher than the corresponding features of the LV winding within both transformers. Table 6-2 shows that the 11 combined features of the HV winding are, in contrast, less than the corresponding features of the LV winding. This is the case in all features except for featureτ_1, which is always greater, and Φ_2 which always equals zero and hence is omitted from the upcoming calculations. Tables 6-1 and 6-2 indicate that all features of the 40 MVA transformer are higher than the corresponding features of the 10 kVA transformer.

Table 6-2 The 11 extracted features for healthy HV and LV windings in both transformers

Feature		**10 kVA transformer**		**40 MVA transformer**	
		HV	**LV**	**HV**	**LV**
Invariant moment	Φ_1	**0.2929**	**0.4745**	**0.6207**	**0.8109**
	Φ_2	**0.0000**	**0.0000**	**0.0000**	**0.0000**
	Φ_3	**0.0016**	**0.0017**	**0.0070**	**0.0072**
	Φ_4	**-0.0054**	**-0.0077**	**-0.0320**	**-0.0377**
	Φ_5	**0.6358**	**1.7363**	**3.1864**	**5.2993**
	Φ_6	**0.0975**	**0.4392**	**1.0943**	**2.3430**
	Φ_7	**0.5423**	**1.4437**	**2.5769**	**4.3172**
Texture analysis	τ_1	**0.0779**	**0.0611**	**0.0573**	**0.0521**
	τ_2	**1.9611**	**1.9694**	**1.9714**	**1.9740**
	τ_3	**1.8222**	**1.8588**	**1.8664**	**1.8789**
	τ_4	**0.4876**	**0.5075**	**0.5295**	**0.5301**
RMS		**0.863598**	**1.091791**	**1.538326**	**2.345671**

The reliability, accuracy and capability of the proposed DIP technique to identify fault type, level, and location are each assessed by re-examining all previous case studies of mechanical and non-mechanical faults (Chapter 5), using the proposed polar plot signature along with the developed DIP code.

6:4 Case Study 1: SC Turns Faults

As previously mentioned in Chapter 5, the various levels and different locations of SC turns within both the 10 kVA and 40 MVA transformers’ LV and HV windings are simulated to apply the proposed DIP approach. The FRA polar plot signatures of all SC fault cases are obtained through a computer-based algorithm that has been developed to combine the FRA signature's magnitude and phase angle into one polar plot. The obtained polar plots are processed using the developed DIP technique to extract 15 features (four geometric dimensions, seven invariant moment and four texture analyses) and calculate the three unique metrics (CBD, RMS and IED) as discussed below.

6:4:1 LV Winding (10 kVA Transformer)

As shown in Figure 6-3, the impacts of five minor SC fault levels (1% to 5%) as well as an exaggerated fault level (40%) on the proposed polar plot signatures are obtained within phase A of the 10 kVA transformer's LV winding. Although it is still difficult to identify the faulty signature through visual inspection, the polar plot approach has the advantage of comprising more image features than the magnitude plot. It also facilitates the utilisation of various DIP techniques, which aid in the standardisation and automation of the FRA technique's interpretation process.

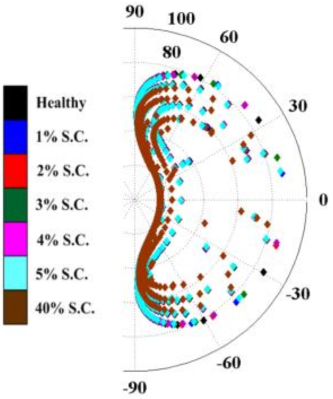

Figure 6-3 Impact of 10 kVA transformer's LV winding SC faults on FRA polar plot signature

The polar plot geometric dimension features of the studied fault levels are extracted and listed in Table 6-3. These results reveal that the area and perimeter features decrease gradually along the increase in fault level. The other three features only change slightly with the change in fault level. As shown in Table 6-3 and Figure

6-4, the calculated CBD value of the extracted geometric dimension features increases with the increase in fault level. In the case of the exaggerated fault level (40%), the increase in CBD value is significant. CBD minimum and maximum threshold levels to indicate the severity of the SC fault within the investigated transformer's LV winding are shown in Figure 6-4.

Table 6-3 Geometric dimension features of 10 kVA transformer's LV winding SC faults

Feature		Fault level					
		1%	2%	3%	4%	5%	40%
g1		9598	9549	9529	9493	9457	7985
g2		491.71	490.88	489.71	488.29	487.71	439.91
g3	X-axis	339.74	339.57	339.64	339.56	339.60	338.37
	Y-axis	289.59	289.89	289.49	289.81	289.37	289.58
g4	Major	219.02	220.24	219.03	218.97	217.55	159.74
	Minor	60.48	59.48	59.77	59.52	59.91	55.72
CBD		7.76	55.24	78.24	115.23	154.02	1735.51

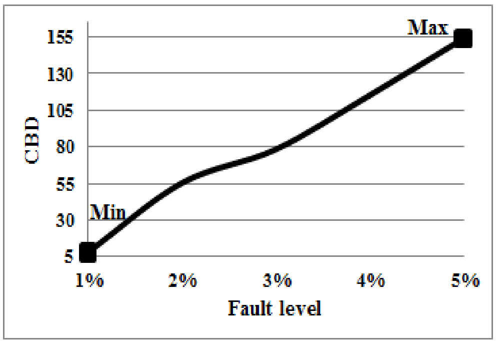

Figure 6-4 CBD trend for various SC fault levels on the 10 kVA LV winding

The 11 polar plot features of the investigated short circuit fault levels are extracted and listed in Table 6-4. Features, 1, 5, 6, 9, 10 and 11, increase with the increase in fault level. However, Features, 3, 4, 7 and 8, decrease with the increase in fault level. Feature 2 is maintained at zero value. It can also be seen in this table that the RMS and IED values of the 11 features increase with the increase in fault level. The increase in these two metrics is significant in the case of the 40% SC fault. As shown in Figures 6-5 and 6-6, the maximum and minimum threshold levels for the two parameters can be chosen.

Table 6-4 The 11 extracted features of 10 kVA transformer's LV winding SC faults

Feature		Fault level					
		1%	2%	3%	4%	5%	40%
Invariant moment	1(Φ_1)	0.4881	0.4916	0.4934	0.4966	0.5067	0.5512
	2(Φ_2)	0.0000	0.0000	0.0000	0.0000	0.0000	0.0000
	3(Φ_3)	0.0016	0.0015	0.0014	0.0013	0.0012	0.0008
	4(Φ_4)	-0.0074	-0.0075	-0.0074	-0.0073	-0.0072	-0.0063
	5(Φ_5)	1.7372	1.7374	1.7375	1.7378	1.7379	1.8154
	6(Φ_6)	0.4428	0.4436	0.4452	0.4463	0.4471	0.5652
	7(Φ_7)	1.4431	1.4429	1.4427	1.4426	1.4425	1.2151
Texture analysis	8(τ_1)	0.0609	0.0607	0.0606	0.0605	0.0604	0.0512
	9(τ_2)	1.9901	1.9905	1.9906	1.9912	1.9919	2.6527
	10(τ_3)	1.8592	1.8593	1.8595	1.8597	1.8599	2.4621
	11(τ_4)	0.5078	0.5079	0.5082	0.5083	0.5085	0.6134
RMS		1.096004	1.096265	1.096447	1.096784	1.097390	1.309861
IED		0.025059	0.027559	0.029095	0.031932	0.040158	0.960447

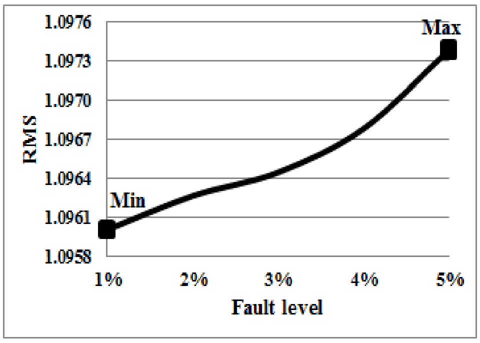

Figure 6-5 RMS trend for various SC fault levels on the 10 kVA transformer's LV winding

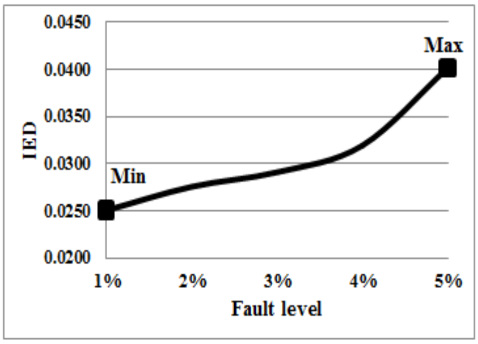

Figure 6-6 IED trend for various SC fault levels on the 10 kVA transformer's LV winding

6:4:2 HV Winding (10 kVA Transformer)

As shown in Figure 6-7, the FRA polar plot signatures for phase A of the 10 kVA's transformer's HV winding are obtained when SC faults of various levels (1% to 5%, and 40%) occur in the top disk (Disk 1), middle disk (Disk 3) and bottom disk (Disk 6). The proposed DIP technique is applied to the measured polar plot signatures to extract four features using the geometric dimension technique, and 11 features using the invariant moment and textures analysis techniques, as listed in Tables 6-5 through 6-10, respectively.

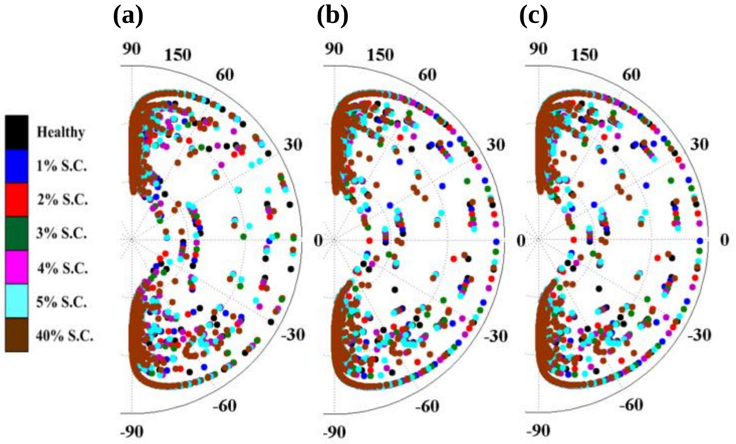

Figure 6-7 Impact of 10 kVA transformer's HV winding SC faults on phase A of polar plot signature (a) top (Disk 1), (b) middle (Disk 3), and (c) bottom (Disk 6)

Table 6-5 Geometric dimension features of 10 kVA transformer's HV winding SC faults (Disk 1)

Feature		Fault level					
		1%	2%	3%	4%	5%	40%
g1		30440	30433	30425	30412	30408	30098
g2		876.60	876.11	875.79	875.23	874.90	787.20
g3	X-axis	358.91	358.83	358.84	358.85	358.82	353.42
	Y-axis	289.74	289.80	289.87	289.76	289.70	287.73
g4	Major	375.12	374.79	374.84	374.79	374.77	237.43
	Minor	109.39	109.38	109.35	109.35	109.31	106.78
CBD		5.59	12.78	21	34.71	39.19	584.13

As in the case of the LV winding and as shown in Figure 6-8, the geometrical features and calculated CBD value increase with the increase in fault level. The increase is, however, not as significant as in the LV winding. This may be attributed to the type of winding.

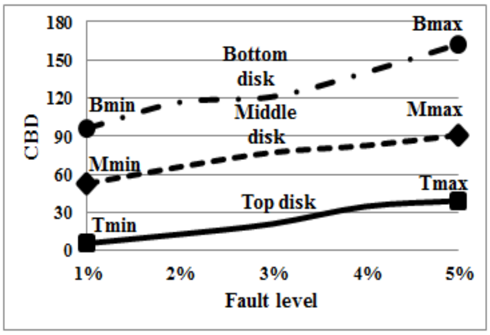

Figure 6-8 CBD trend for various SC fault levels at different locations on the 10 kVA transformer's HV winding

Table 6-6 Geometric dimension features of 10 kVA transformer's HV winding SC faults (Disk 3)

Feature		Fault level					
		1%	2%	3%	4%	5%	40%
g1		30395	30382	30371	30366	30358	30067
g2		874.47	874.13	873.90	873.56	873.26	763.96
g3	X-axis	358.80	358.83	358.88	358.92	358.87	352.82
	Y-axis	289.82	290.01	289.73	289.65	289.73	286.31
g4	Major	374.63	374.82	374.96	374.86	374.90	235.61
	Minor	109.30	109.30	109.29	109.29	109.29	105.78
CBD		52.67	65.86	77.21	82.57	90.78	643.21

Table 6-7 Geometric dimension features of 10 kVA transformer's HV winding SC faults (Disk 6)

Feature		Fault level					
		1%	2%	3%	4%	5%	40%
g1		30353	30333	30329	30310	30288	30021
g2		872.96	872.60	872.37	872.11	871.87	742.91
g3	X-axis	358.89	358.90	358.90	358.89	358.85	351.11
	Y-axis	289.84	289.77	289.75	289.86	289.80	285.22
g4	Major	374.75	375.03	375.08	374.90	374.90	233.92
	Minor	109.28	109.17	109.15	109.10	109.01	104.29
CBD		96.05	116.68	121	140.01	162.36	716.24

Table 6-8 The 11 extracted features of 10 kVA transformer’s HV winding SC faults (Disk 1)

Feature		Fault level					
		1%	2%	3%	4%	5%	40%
Invariant moment	1(Φ_1)	0.2953	0.2957	0.2959	0.2961	0.2963	0.3017
	2(Φ_2)	0.0000	0.0000	0.0000	0.0000	0.0000	0.0000
	3(Φ_3)	0.0015	0.0014	0.0012	0.0011	0.0010	0.0008
	4(Φ_4)	-0.0047	-0.0046	-0.0045	-0.0043	-0.0041	-0.0032
	5(Φ_5)	0.6715	0.6737	0.6748	0.6761	0.6782	0.7026
	6(Φ_6)	0.0977	0.0978	0.0979	0.0980	0.0981	0.1015
	7(Φ_7)	0.5405	0.5402	0.5397	0.5396	0.5393	0.5262
Texture analysis	8(τ_1)	0.0769	0.0767	0.0766	0.0764	0.0762	0.0735
	9(τ_2)	1.9613	1.9615	1.9616	1.9618	1.9619	2.0025
	10(τ_3)	1.8547	1.8548	1.8549	1.8551	1.8552	1.9017
	11(τ_4)	0.4932	0.4944	0.4966	0.4987	0.4999	0.5623
RMS		0.872592	0.872863	0.873072	0.873352	0.873590	0.895439
IED		0.048710	0.050597	0.051866	0.053401	0.055358	0.135846

Table 6-9 The 11 extracted features of 10 kVA transformer’s HV winding SC faults (Disk 3)

Feature		Fault level					
		1%	2%	3%	4%	5%	40%
Invariant moment	1(Φ_1)	0.2964	0.2966	0.2967	0.2969	0.2972	0.3029
	2(Φ_2)	0.0000	0.0000	0.0000	0.0000	0.0000	0.0000
	3(Φ_3)	0.0014	0.0012	0.0011	0.0010	0.0009	0.0006
	4(Φ_4)	-0.0039	-0.0037	-0.0036	-0.0035	-0.0032	-0.0022
	5(Φ_5)	0.6825	0.6847	0.6852	0.6875	0.6896	0.7053
	6(Φ_6)	0.0983	0.0984	0.0986	0.0987	0.0989	0.1017
	7(Φ_7)	0.5389	0.5387	0.5386	0.5385	0.5384	0.5243
Texture analysis	8(τ_1)	0.0758	0.0757	0.0756	0.0755	0.0753	0.0728
	9(τ_2)	1.9622	1.9624	1.9625	1.9626	1.9629	2.0037
	10(τ_3)	1.8553	1.8554	1.8556	1.8557	1.8558	1.9024
	11(τ_4)	0.5023	0.5034	0.5047	0.5068	0.5087	0.5679
RMS		0.874080	0.874349	0.87451	0.874825	0.875160	0.896264
IED		0.059371	0.061483	0.062357	0.064866	0.067228	0.141436

For all fault locations, the RMS and IED values increase with the increase in the short circuit fault level as shown in Figures 6-9 and 6-10. The three metrics show the ability of the proposed approach to identify the SC fault’s level and location within the transformer winding.

Table 6-10 The 11 extracted features of 10 kVA transformer's HV winding SC faults (Disk)

Feature		Fault level					
		1%	2%	3%	4%	5%	40%
Invariant moment	1(Φ_1)	0.2973	0.2974	0.2977	0.2978	0.2979	0.3032
	2(Φ_2)	0.0000	0.0000	0.0000	0.0000	0.0000	0.0000
	3(Φ_3)	0.0013	0.0012	0.0011	0.0009	0.0007	0.0005
	4(Φ_4)	-0.0029	-0.0027	-0.0025	-0.0023	-0.0021	-0.0011
	5(Φ_5)	0.6918	0.6941	0.6952	0.6975	0.6986	0.7095
	6(Φ_6)	0.0991	0.0992	0.0994	0.0996	0.0998	0.1019
	7(Φ_7)	0.5381	0.5379	0.5377	0.5375	0.5374	0.5233
Texture analysis	8(τ_1)	0.0749	0.0748	0.0746	0.0743	0.0741	0.0720
	9(τ_2)	1.9631	1.9633	1.9635	1.9636	1.9638	2.0058
	10(τ_3)	1.8561	1.8562	1.8563	1.8565	1.8567	1.9031
	11(τ_4)	0.5121	0.5132	0.5144	0.5167	0.5188	0.5691
RMS		0.875582	0.875858	0.87606	0.8764	0.876669	0.897149
IED		0.070316	0.072627	0.074044	0.076883	0.078710	0.145453

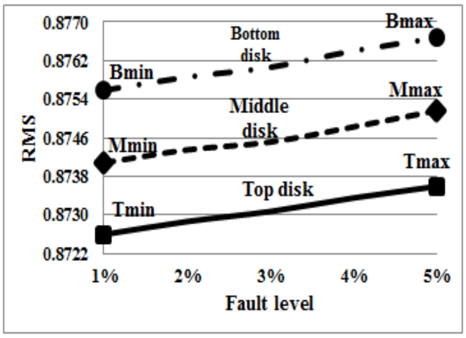

Figure 6-9 RMS trend for various SC fault levels at different locations on the 10 kVA transformer's HV winding

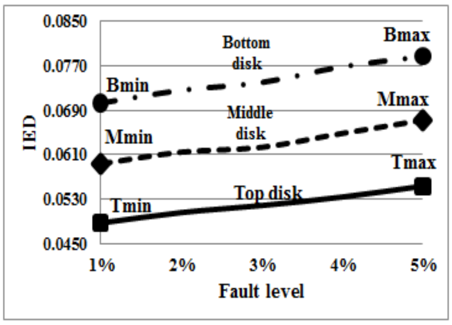

Figure 6-10 IED trend for various SC fault levels at different locations on the 10 kVA transformer's HV winding

As shown in Figures 6-9 and 6-10, different threshold levels can be chosen to simulate different SC fault levels. These thresholds indicate the minimum and maximum limits of the minor SC fault level at each location without any overlapping between the limits.

6:4:3 LV Winding (40 MVA Transformer)

In the 40 MVA transformer, SC faults of minor levels (1% to 5%) and one exaggerated level (40%) are applied on phase A of the LV winding. The polar plot for each fault level is obtained and processed using the proposed application to extract the proposed image features as listed in Tables 6-11 and 6-12. As can be seen in these two tables, the impact of various SC faults on the extracted features of the LV winding is similar to the previous case study; however, the magnitudes of the 40 MVA transformer's features are larger than the corresponding features of the 10 kVA transformer. On the other hand, the calculated values for CBD, RMS and IED reveal a similar trend to the corresponding values of the 10 kVA transformer as shown in Figures 6-11, 6-12 and 6-13. These figures also show the proposed threshold levels for this case study.

Table 6-11 Geometric dimension features of the 40 MVA transformer's LV winding SC faults

Feature		**Fault level**					
		1%	**2%**	**3%**	**4%**	**5%**	**40%**
g1		**47685**	**47665**	**47652**	**47643**	**47631**	**46210**
g2		**1471.88**	**1470.76**	**1468.62**	**1465.54**	**1462.42**	**1429.41**
g3	**X-axis**	**672.85**	**672.77**	**672.64**	**672.57**	**672.34**	**668.32**
	Y-axis	**559.68**	**559.5**	**559.46**	**559.32**	**559.12**	**539.52**
g4	**Major**	**642.67**	**642.67**	**642.52**	**642.43**	**642.33**	**641.85**
	Minor	**125.67**	**124.32**	**122.72**	**120.98**	**119.63**	**112.37**
CBD		**11.53**	**34.26**	**60.32**	**77.44**	**82.44**	**1567.81**

Table 6-12 The 11 extracted features of the 40 MVA transformer’s LV winding SC faults

Feature		Fault level					
		1%	2%	3%	4%	5%	40%
Invariant moment	1(Φ_1)	0.8234	0.8428	0.8587	0.8694	0.8721	0.9103
	2(Φ_2)	0.0000	0.0000	0.0000	0.0000	0.0000	0.0000
	3(Φ_3)	0.0057	0.0053	0.0045	0.0042	0.0039	0.0021
	4(Φ_4)	-0.0465	-0.0482	-0.0518	-0.0534	-0.0564	-0.0582
	5(Φ_5)	5.5237	5.5357	5.5526	5.5617	5.5829	5.6147
	6(Φ_6)	2.3528	2.3542	2.3565	2.3571	2.3588	2.3614
	7(Φ_7)	4.3169	4.3143	4.3132	4.3124	4.3115	4.2889
Texture analysis	8(τ_1)	0.0518	0.0512	0.0496	0.0492	0.0488	0.0413
	9(τ_2)	1.9770	1.9752	1.9762	1.9774	1.9786	1.9852
	10(τ_3)	1.8818	1.8812	1.8833	1.8842	1.8865	1.8947
	11(τ_4)	0.5341	0.5385	0.5419	0.5465	0.5548	0.5632
RMS		2.395078	2.397821	2.402206	2.404642	2.409629	2.415435
IED		0.225213	0.239225	0.258882	0.270315	0.292433	0.335456

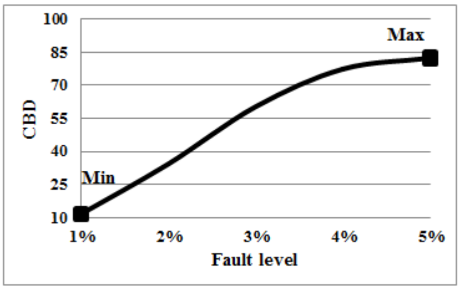

Figure 6-11 CBD trend for various SC fault levels on the 40 MVA transformer’s LV winding

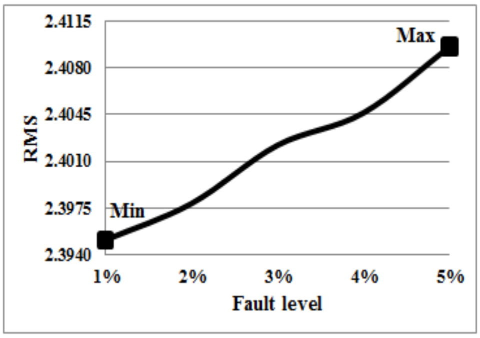

Figure 6-12 RMS trend for various SC fault levels on the 40 MVA transformer’s LV winding

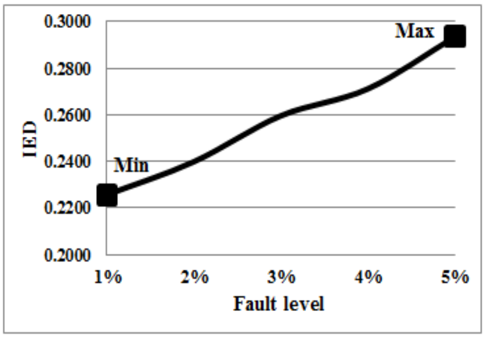

Figure 6-13 IED trend for various SC fault levels on the 40 MVA transformer's LV winding

6:4:4 HV Winding (40 MVA Transformer)

As the HV winding of the 40 MVA transformer consists of 10 disks per phase, SC faults of various levels are applied to the windings on the top disk (Disk 1), the middle disk (Disk 5) and the bottom disk (Disk 10). The proposed DIP application is used to obtain the polar plot signatures of all studied cases. The signatures are then processed to extract geometric dimension, invariant moment and texture analysis features as listed in Tables 6-13 through 6-18, respectively. Values of CBD, RMS and IED are calculated for each fault level and location as given in Figures 6-14, 6-15 and 6-16.

Table 6-13 Geometric dimension features of the 40 MVA transformer's HV winding SC faults (Disk 1)

Feature		Fault level					
		1%	2%	3%	4%	5%	40%
g1		65995	65981	65972	65961	65949	65284
g2		1822.72	1819.84	1813.84	1806.97	1802.02	1743.95
g3	X-axis	671.82	671.51	671.14	671.08	671.02	594.32
	Y-axis	609.95	609.11	608.82	608.25	608.03	601.85
g4	Major	831.91	831.78	831.52	831.43	831.18	825.01
	Minor	197.32	197.28	196.85	196.62	196.14	191.67
CBD		120.1	138.3	154.65	173.47	191.43	1008.02

Table 6-14 Geometric dimension features of the 40 MVA transformer's HV winding SC faults (Disk 5)

Feature		Fault level					
		1%	2%	3%	4%	5%	40%
g1		65688	65667	65651	65632	65604	65113
g2		1796.35	1794.76	1792.57	1791.61	1790.94	1735.21
g3	X-axis	670.92	670.71	670.58	670.41	670.27	593.49
	Y-axis	606.72	606.54	606.11	605.92	605.61	601.31
g4	Major	830.96	830.81	830.67	830.51	830.32	823.11
	Minor	195.93	195.81	195.65	195.42	195.15	191.22
CBD		459.94	483.19	502.24	522.95	552.53	1191.48

Table 6-15 Geometric dimension features of the 40 MVA transformer's HV winding SC faults (Disk 10)

Feature		Fault level					
		1%	2%	3%	4%	5%	40%
g1		65482	65461	65449	65434	65408	65034
g2		1779.18	1776.27	1775.55	1773.73	1771.91	1719.37
g3	X-axis	669.83	669.75	669.58	669.41	669.26	592.95
	Y-axis	603.82	603.54	603.13	602.83	602.41	601.24
g4	Major	828.83	828.52	828.13	827.78	827.56	822.02
	Minor	193.95	193.76	193.52	193.37	193.12	189.63
CBD		691.21	715.98	729.91	747.70	776.56	1289.61

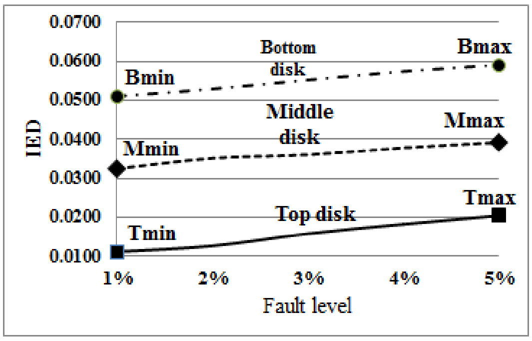

Figure 6-14 CBD trend for various SC fault levels at different locations on the 40 MVA transformer's HV winding

As shown in these tables and figures, the CBD of the geometric dimension features, the RMS, and the IED of the 11 invariant moment and texture analysis techniques increase along with the increase in fault level. On the other hand, when the short circuit fault moves toward the bottom of the HV winding, the CBD, RMS and IED values consistently increase.

Table 6-16 The 11 extracted features of the 40 MVA transformer's HV winding SC faults (Disk 1)

Feature		Fault level					
		1%	2%	3%	4%	5%	40%
Invariant moment	1(Φ_1)	0.6215	0.6222	0.6228	0.6231	0.6237	0.6915
	2(Φ_2)	0.0000	0.0000	0.0000	0.0000	0.0000	0.0000
	3(Φ_3)	0.0069	0.0068	0.0065	0.0064	0.0063	0.0038
	4(Φ_4)	-0.0324	-0.0325	-0.0326	-0.0327	-0.0328	-0.0825
	5(Φ_5)	3.1912	3.1914	3.1915	3.1917	3.1918	3.4196
	6(Φ_6)	1.0952	1.0954	1.0955	1.0957	1.0958	1.1014
	7(Φ_7)	2.5682	2.5676	2.5653	2.5636	2.5628	2.3521
Texture analysis	8(τ_1)	0.0568	0.0566	0.0564	0.0563	0.0562	0.0537
	9(τ_2)	1.9722	1.9737	1.9754	1.9767	1.9783	2.0004
	10(τ_3)	1.8711	1.8725	1.8743	1.8756	1.8774	1.9002
	11(τ_4)	0.5301	0.5308	0.5312	0.5317	0.5322	0.5623
RMS		1.538625	1.538962	1.53907	1.539185	1.539514	1.562502
IED		0.011122	0.012646	0.015784	0.018224	0.020432	0.340019

Table 6-17 The 11 extracted features of the 40 MVA transformer's HV winding SC faults (Disk 5)

Feature		Fault level					
		1%	2%	3%	4%	5%	40%
Invariant moment	1(Φ_1)	0.6406	0.6412	0.6417	0.6425	0.6434	0.6929
	2(Φ_2)	0.0000	0.0000	0.0000	0.0000	0.0000	0.0000
	3(Φ_3)	0.0058	0.0056	0.0054	0.0052	0.0051	0.0036
	4(Φ_4)	-0.0421	-0.0435	-0.0439	-0.0441	-0.0448	-0.0854
	5(Φ_5)	3.2105	3.2112	3.2119	3.2121	3.2124	3.5215
	6(Φ_6)	1.0961	1.0963	1.0964	1.0966	1.0967	1.1026
	7(Φ_7)	2.5479	2.5462	2.5457	2.5451	2.5447	2.3401
Texture analysis	8(τ_1)	0.0558	0.0556	0.0555	0.0553	0.0552	0.0534
	9(τ_2)	1.9802	1.9838	1.9841	1.9862	1.9879	2.0006
	10(τ_3)	1.8805	1.8809	1.8812	1.8819	1.8821	1.9011
	11(τ_4)	0.5411	0.5416	0.5421	0.5426	0.5432	0.5641
RMS		1.542315	1.542711	1.542879	1.543209	1.543488	1.581651
IED		0.048348	0.051277	0.052494	0.054192	0.055787	0.424005

Table 6-18 The 11 extracted features of the 40 MVA transformer's HV winding SC faults (Disk 10)

Feature		Fault level					
		1%	2%	3%	4%	5%	40%
Invariant moment	1(Φ_1)	0.6611	0.6617	0.6621	0.6627	0.6633	0.6946
	2(Φ_2)	0.0000	0.0000	0.0000	0.0000	0.0000	0.0000
	3(Φ_3)	0.0047	0.0046	0.0045	0.0043	0.0042	0.0022
	4(Φ_4)	-0.0631	-0.0637	-0.0642	-0.0645	-0.0648	-0.0877
	5(Φ_5)	3.3201	3.3208	3.3213	3.3218	3.322	3.6407
	6(Φ_6)	1.0973	1.0974	1.0975	1.0977	1.0979	1.1031
	7(Φ_7)	2.5386	2.5371	2.5359	2.5348	2.5342	2.3321
Texture analysis	8(τ_1)	0.0549	0.0547	0.0546	0.0543	0.0542	0.0531
	9(τ_2)	1.9911	1.9925	1.9948	1.9971	1.9985	2.0008
	10(τ_3)	1.8901	1.8906	1.891	1.8919	1.8922	1.9014
	11(τ_4)	0.5507	0.5510	0.5513	0.5518	0.5525	0.5664
RMS		1.565419	1.565591	1.565853	1.566205	1.56641	1.605177
IED		0.152844	0.15443	0.155825	0.157359	0.158306	0.527682

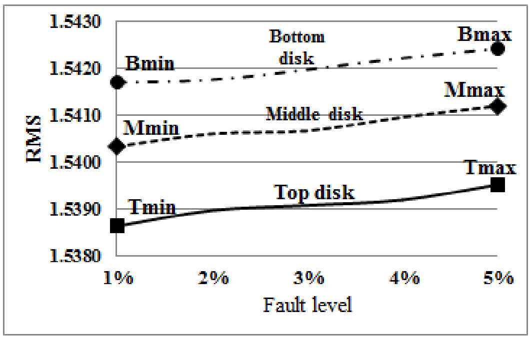

Figure 6-15 RMS trend for various SC fault levels at different locations on the 40 MVA transformer's HV winding

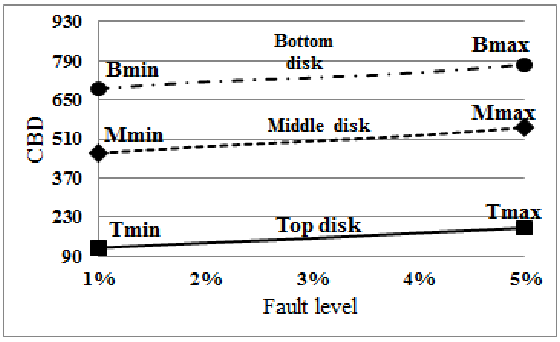

Figure 6-16 IED trend for various SC fault levels at different locations on the 40 MVA transformer's HV winding

6:5 Case Study 2: Radial Faults

In this section, radial faults are investigated using the proposed DIP application by re-examining the same fault's case studies simulated in Chapter 5, which were previously examined using the conventional FRA signature.

6:5:1 Forced Radial Buckling (10 kVA Transformer)

Using the proposed approach, the impacts of five minor levels (1% to 5%) and one exaggerated level (40%) of forced radial buckling on the polar plot signatures are investigated within phase A of the 10 kVA transformer's LV winding. The 15 extracted features of the obtained polar plots are measured and listed in Tables 6-19 and 6-20. These include four features using the geometric dimension technique and 11 features using the invariant moment and textures analysis techniques, respectively. The results reveal that all geometric dimension features decrease along with the increase in fault level. In the case of the 40% fault level, the decrement is significant. The geometric features are also used to calculate the CBD metric. As can be seen in Table 6-19 and Figure 6-17, the CBD value increases along with the increase in fault level.

Table 6-19 Geometric dimension features of the 10 kVA transformer's LV winding forced buckling

Feature		Fault level					
		1%	2%	3%	4%	5%	40%
g1		9387	9362	9359	9344	9336	8793
g2		486.82	486.43	486.11	485.79	485.63	472.73
g3	X-axis	338.86	338.59	338.52	338.47	338.28	337.12
	Y-axis	288.96	288.78	288.57	288.44	288.38	288.07
g4	Major	220.18	219.54	218.63	217.82	216.91	214.21
	Minor	59.22	59.21	59.19	59.18	59.16	58.44
CBD		222.8	249.29	253.82	270.14	279.48	617.47

Table 6-20 The 11 extracted features of the 10 kVA transformer's LV winding forced buckling

Feature		Fault level					
		1%	2%	3%	4%	5%	40%
Invariant moment	1(Φ_1)	0.4751	0.4754	0.4758	0.4761	0.4767	0.4801
	2(Φ_2)	0.0000	0.0000	0.0000	0.0000	0.0000	0.0000
	3(Φ_3)	0.0016	0.0014	0.0013	0.0012	0.0011	0.0008
	4(Φ_4)	-0.0074	-0.0071	-0.0067	-0.0061	-0.0058	-0.0033
	5(Φ_5)	1.7428	1.7431	1.7438	1.7452	1.7464	1.7892
	6(Φ_6)	0.4427	0.4438	0.4453	0.4466	0.4482	0.4816
	7(Φ_7)	1.4322	1.4317	1.4311	1.4309	1.4305	1.4293
Texture analysis	8(τ_1)	0.0605	0.0601	0.0597	0.0592	0.0586	0.0580
	9(τ_2)	1.9725	1.9736	1.9757	1.9778	1.9789	1.9806
	10(τ_3)	1.8627	1.8633	1.8667	1.8679	1.8681	1.8723
	11(τ_4)	0.5086	0.5094	0.5103	0.5118	0.5129	0.5174
RMS		1.092663	1.093005	1.094014	1.094845	1.095310	1.103955
IED		0.014615	0.015973	0.019156	0.021878	0.024046	0.026640

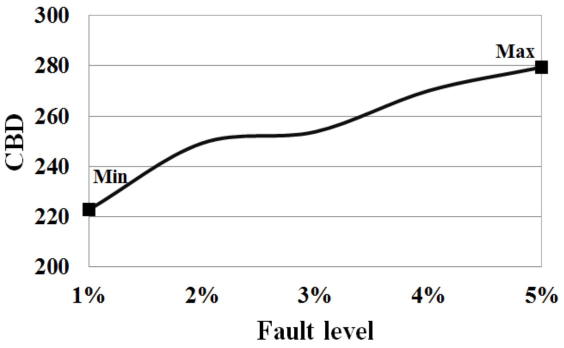

Figure 6-17 CBD trend for the 10 kVA transformer's LV winding forced buckling

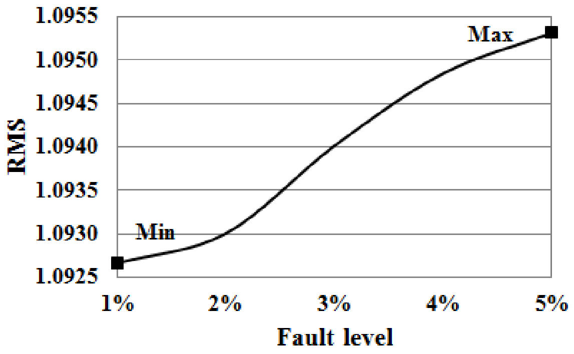

Figure 6-18 RMS trend for the 10 kVA transformer's LV winding forced buckling

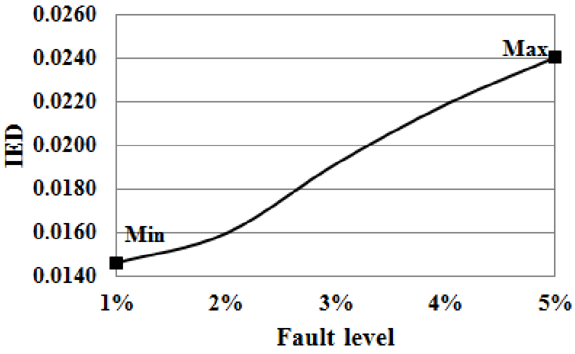

Figure 6-19 IED trend for the 10 kVA transformer's LV winding forced buckling

Table 6-20 shows that while features Φ_1, Φ_5, Φ_6, τ_2, τ_3, and τ_4 increase along with the increase in fault level, features Φ_3, Φ_4, Φ_7, and τ_1 decrease, and feature Φ_2 is maintained at zero. The 11 combined features in Table 6-20 are used to calculate the RMS and IED. As can be seen in Figures 6-18 and 6-19, both RMS and IED values increase along with the increase in fault level.

6:5:2 Free Radial Buckling (10 kVA Transformer)

When a free radial buckling fault takes place on phase A of the 10 kVA transformer's HV winding, the impacts of various fault levels (1% to 5%, and 40%) and locations (top disk (Disk 1), middle disk (Disk 3), and bottom disk (Disk 6)) are obtained. The polar plot signatures of the case studies are manipulated using the developed DIP code to extract 15 geometric dimension, invariant moment and textures analysis features as listed in Tables 6-21 through 6-26, respectively. In all of these tables, the trend of all features is found to be similar to that of the forced radial buckling case study.

The 15 extracted features are used to calculate the three metrics (CBD, RMS and IED). Similar to the case study mentioned above, results show that the three metrics increase along with the increase in fault level. Figures 6-20, 6-21 and 6-22 reveal that the three metrics also increase when the fault moves toward the bottom of the HV winding.

Table 6-21 Geometric dimension features of 10 kVA transformer's HV winding free buckling (Disk 1)

Feature		Fault level					
		1%	2%	3%	4%	5%	40%
g1		30278	30265	30259	30251	30249	30232
g2		871.46	871.29	871.11	870.98	870.72	870.21
g3	X-axis	357.75	357.59	357.37	357.24	357.19	356.92
	Y-axis	288.83	288.79	288.64	288.56	288.47	288.31
g4	Major	373.98	373.81	373.75	373.63	373.54	373.42
	Minor	109.32	109.29	109.17	109.11	109.08	108.81
CBD		175.35	188.92	195.65	204.17	206.69	225.02

Table 6-22 Geometric dimension features of 10 kVA transformer's HV winding free buckling (Disk 3)

Feature		Fault level					
		1%	2%	3%	4%	5%	40%
g1		30226	30221	30217	30210	30205	30197
g2		870.53	870.24	870.06	869.96	869.78	869.53
g3	X-axis	356.97	356.92	356.88	356.83	356.79	356.69
	Y-axis	288.40	288.38	288.34	288.29	288.25	288.03
g4	Major	373.50	373.48	373.41	373.37	373.32	373.12
	Minor	108.87	108.81	108.79	108.72	108.68	108.63
CBD		230.42	235.86	240.21	247.52	252.87	261.69

Table 6-23 Geometric dimension features of 10 kVA transformer's HV winding free buckling (Disk 6)

Feature		Fault level					
		1%	2%	3%	4%	5%	40%
g1		30190	30184	30175	30163	30157	30149
g2		869.43	869.28	869.03	868.86	868.65	868.31
g3	X-axis	356.64	356.41	356.35	356.28	356.15	364.96
	Y-axis	287.83	287.64	287.42	287.35	287.22	287.01
g4	Major	372.93	372.78	372.62	372.53	372.11	371.96
	Minor	108.60	108.52	108.43	108.35	108.11	107.98
CBD		269.26	276.06	285.84	298.32	305.45	317.69

Table 6-24 The 11 extracted features of 10 kVA transformer’s HV winding free buckling (Disk 1)

Feature		Fault level					
		1%	2%	3%	4%	5%	40%
Invariant moment	1(Φ1)	0.2949	0.2951	0.2954	0.2957	0.2962	0.2965
	2(Φ2)	0.0000	0.0000	0.0000	0.0000	0.0000	0.0000
	3(Φ3)	0.0015	0.0014	0.0013	0.0012	0.0011	0.0007
	4(Φ4)	-0.0048	-0.0046	-0.0044	-0.0043	-0.0041	-0.0040
	5(Φ5)	0.6461	0.6463	0.6464	0.6465	0.6468	0.6484
	6(Φ6)	0.0976	0.0977	0.0980	0.0982	0.0983	0.0984
	7(Φ7)	0.5319	0.5317	0.5315	0.5313	0.5311	0.5310
Texture analysis	8(τ_1)	0.0768	0.0765	0.0763	0.0762	0.0761	0.0760
	9(τ_2)	1.9622	1.9627	1.9635	1.9637	1.9641	1.9642
	10(τ_3)	1.8412	1.8413	1.8415	1.8417	1.8419	1.8420
	11(τ_4)	0.4881	0.4883	0.4884	0.4886	0.4887	0.4889
RMS		0.867664	0.867804	0.868018	0.868114	0.868265	0.868428
IED		0.024130	0.024453	0.024860	0.025220	0.025718	0.026645

Table 6-25 The 11 extracted features of 10 kVA transformer’s HV winding free buckling (Disk 3)

Feature		Fault level					
		1%	2%	3%	4%	5%	40%
Invariant moment	1(Φ1)	0.2967	0.2972	0.2975	0.2977	0.2979	0.2980
	2(Φ2)	0.0000	0.0000	0.0000	0.0000	0.0000	0.0000
	3(Φ3)	0.0013	0.0011	0.0009	0.0007	0.0005	0.0003
	4(Φ4)	-0.0039	-0.0037	-0.0035	-0.0033	-0.0032	-0.0030
	5(Φ5)	0.6571	0.6575	0.6577	0.6578	0.6579	0.6580
	6(Φ6)	0.0985	0.0987	0.0988	0.0991	0.0993	0.0991
	7(Φ7)	0.5298	0.5297	0.5296	0.5295	0.5291	0.5286
Texture analysis	8(τ_1)	0.0759	0.0757	0.0755	0.0754	0.0752	0.0750
	9(τ_2)	1.9648	1.9652	1.9658	1.9663	1.9667	1.9669
	10(τ_3)	1.8422	1.8425	1.8426	1.8428	1.8429	1.8430
	11(τ_4)	0.4893	0.4894	0.4895	0.4897	0.4899	0.4901
RMS		0.869144	0.869327	0.869492	0.869653	0.869756	0.869806
IED		0.032377	0.033010	0.033398	0.033774	0.034196	0.034605

Table 6-26 The 11 extracted of 10 kVA transformer's HV winding free buckling (Disk 6)

Feature		Fault level					
		1%	2%	3%	4%	5%	40%
Invariant moment	1(Φ1)	0.2981	0.2982	0.2984	0.2986	0.2988	0.2990
	2(Φ2)	0.0000	0.0000	0.0000	0.0000	0.0000	0.0000
	3(Φ3)	0.0012	0.001	0.0007	0.0006	0.0003	0.0002
	4(Φ4)	-0.0027	-0.0026	-0.0025	-0.0022	-0.0021	-0.0019
	5(Φ5)	0.6682	0.6684	0.6685	0.6687	0.6689	0.6691
	6(Φ6)	0.0993	0.0994	0.0996	0.0997	0.0999	0.1000
	7(Φ7)	0.5187	0.5182	0.5179	0.5175	0.5171	0.5167
Texture analysis	8(τ_1)	0.0748	0.0745	0.0744	0.0743	0.0741	0.0740
	9(τ_2)	1.9673	1.9679	1.9682	1.9686	1.9691	1.9692
	10(τ_3)	1.8431	1.8433	1.8434	1.8437	1.8439	1.8441
	11(τ_4)	0.4904	0.4911	0.4915	0.4917	0.4922	0.4925
RMS		0.870091	0.870277	0.870377	0.870526	0.870692	0.870765
IED		0.046231	0.046895	0.047286	0.047905	0.048521	0.049063

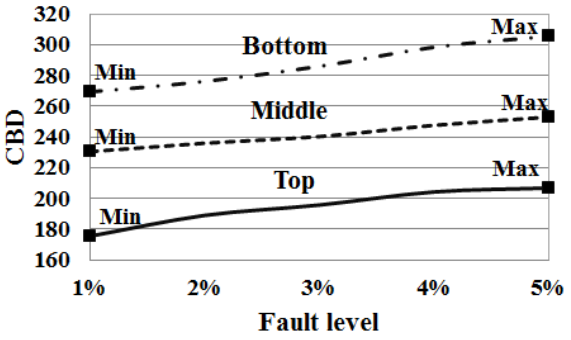

Figure 6-20 CBD trend for the 10 kVA transformer's HV winding free buckling

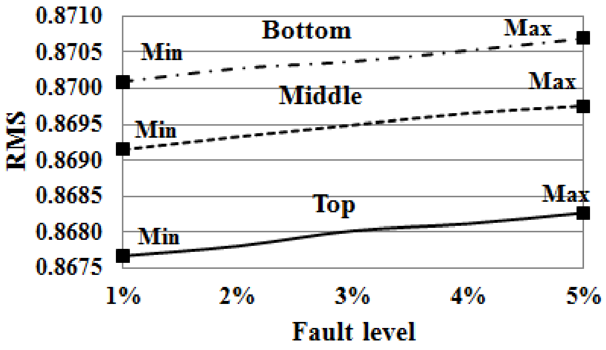

Figure 6-21 RMS trend for the 10 kVA transformer's HV winding free buckling

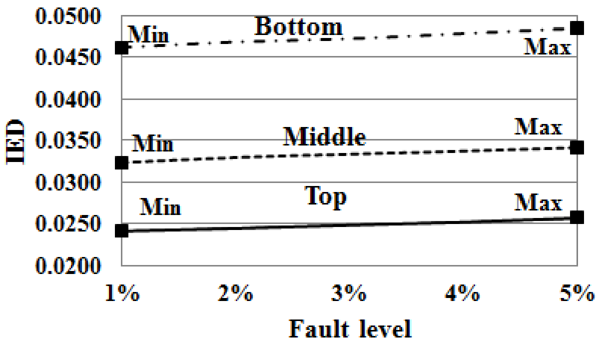

Figure 6-22 IED trend for the 10 kVA transformer's HV winding free buckling

6:5:3 Forced Radial Buckling (40 MVA Transformer)

As listed in Tables 6-27 and 6-28, the impacts of forced radial buckling with fault levels of 1% to 5% and 40% on the polar plots of phase A of the 40 MVA transformer's LV winding are obtained and processed to extract the features, using the DIP techniques employed in this thesis.

As observed in the previous case study, the trend of all features is found to be similar to the trend of all features in the 10 kVA transformer. It can also be seen that the value of the extracted features is larger in the case of the 40 MVA transformer than in the case of the 10 kVA transformer. As shown in Tables 6-27 and 6-28 as well as Figures 6-23, 6-24 and 6-25, the three metrics, CBD, RMS and IED, increase along with the increase in fault level, displaying values higher than those obtained from the 10 kVA transformer.

Table 6-27 Geometric dimension features of 40 MVA transformer's LV winding forced buckling

Feature		Fault level					
		1%	2%	3%	4%	5%	40%
g1		45989	45975	45964	45948	45932	45325
g2		1419.82	1418.63	1417.24	1416.53	1414.77	1393.29
g3	X-axis	659.73	659.61	659.56	659.52	659.43	638.24
	Y-axis	528.73	528.66	528.57	528.53	528.48	513.91
g4	Major	640.71	640.63	640.55	640.39	640.24	638.82
	Minor	109.24	108.62	107.53	106.71	105.38	101.45
CBD		1820.93	1837.01	1850.71	1868.48	1887.86	2557.45

Table 6-28 The 11 extracted features of 40 MVA transformer’s LV winding forced buckling

Feature		Fault level					
		1%	2%	3%	4%	5%	40%
Invariant moment	1(Φ1)	0.9382	0.9423	0.9462	0.9517	0.9578	0.9736
	2(Φ2)	0.0000	0.0000	0.0000	0.0000	0.0000	0.0000
	3(Φ3)	0.0019	0.0018	0.0017	0.0016	0.0015	0.0009
	4(Φ4)	-0.0604	-0.0612	-0.0635	-0.0657	-0.0663	-0.0689
	5(Φ5)	5.6224	5.6237	5.6255	5.6269	5.6283	5.6426
	6(Φ6)	2.3627	2.3641	2.3659	2.3676	2.3683	2.3742
	7(Φ7)	4.2668	4.2666	4.2665	4.2663	4.2662	4.2444
Texture analysis	8(τ_1)	0.041	0.0408	0.0407	0.0405	0.0404	0.0398
	9(τ_2)	2.0005	2.0007	2.0009	2.0011	2.0013	2.0047
	10(τ_3)	1.9002	1.9004	1.9006	1.9008	1.9011	1.9052
	11(τ_4)	0.5661	0.5663	0.5664	0.5666	0.5668	0.5683
RMS		2.416197	2.416745	2.417445	2.418095	2.418698	2.419927
IED		0.355873	0.35875	0.36214	0.36584	0.36964	0.393519

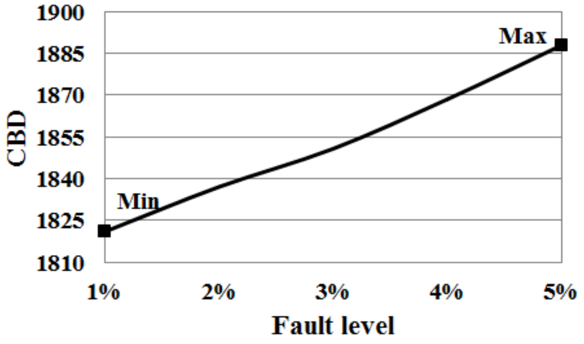

Figure 6-23 CBD trend for the 40 MVA transformer’s LV winding forced buckling

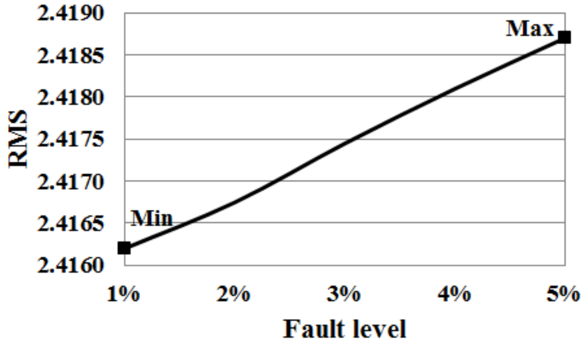

Figure 6-24 RMS trend for the 40 MVA transformer’s LV winding forced buckling

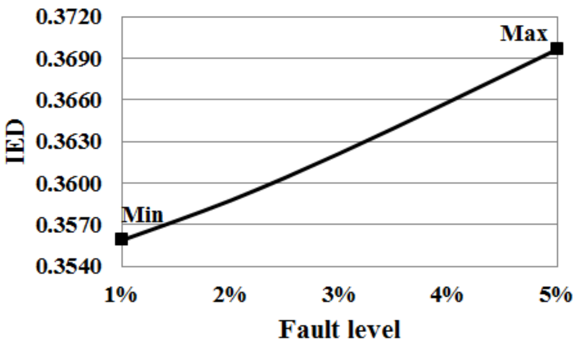

Figure 6-25 IED trend for the 40 MVA transformer's LV winding forced buckling

6:5:4 Free Radial Buckling (40 MVA Transformer)

Table 6-29 Geometric dimension features of 40 MVA transformer's HV winding free buckling (Disk 1)

Feature		Fault level					
		1%	2%	3%	4%	5%	40%
g1		65287	65266	65253	65248	65234	64983
g2		1758.76	1756.31	1755.21	1753.84	1751.45	1721.88
g3	X-axis	643.82	643.67	643.52	643.38	643.21	593.41
	Y-axis	599.83	599.64	599.42	599.37	599.11	596.82
g4	Major	824.81	824.64	824.52	824.37	824.19	819.41
	Minor	192.76	192.59	192.42	192.34	192.17	189.81
CBD		941.84	965.97	980.73	987.52	1004.69	1344.49

Table 6-30 Geometric dimension features of 40 MVA transformer's HV winding free buckling (Disk 5)

Feature		Fault level					
		1%	2%	3%	4%	5%	40%
g1		65192	65173	65160	65145	65123	64732
g2		1748.31	1746.47	1744.82	1742.26	1740.91	1720.76
g3	X-axis	642.76	642.61	642.52	642.38	642.19	592.37
	Y-axis	598.76	598.53	598.48	598.31	598.71	596.42
g4	Major	823.76	823.58	823.41	823.33	823.12	818.25
	Minor	191.84	191.63	191.54	191.41	191.29	189.53
CBD		1051.39	1073	1088.05	1106.13	1129.6	1599.49

Table 6-31 Geometric dimension features of 40 MVA transformer's HV winding free buckling (Disk 10)

Feature		Fault level					
		1%	2%	3%	4%	5%	40%
g1		65086	65062	65045	65027	65018	64598
g2		1737.89	1736.37	1735.62	1733.45	1731.92	1719.83
g3	X-axis	641.92	641.75	641.61	641.43	641.22	591.21
	Y-axis	597.94	597.78	597.63	597.45	597.32	596.13
g4	Major	822.86	822.65	822.48	822.22	822.09	817.17
	Minor	190.91	190.84	190.67	190.51	191.32	189.22
CBD		1171.3	1197.43	1215.81	1236.76	1246.95	1737.26

Free radial buckling faults with five minor fault levels (1% to 5%) and one exaggerated fault level (40%) are simulated on the top disk (Disk 1), middle disk (Disk 5) and bottom disk (Disk 10) of the 40 MVA transformer's HV winding in order to investigate their impact on the proposed polar plot signatures. The polar plots of each fault level and location are processed, and the 15 image features are extracted to calculate the proposed three metrics as listed in Tables 6-29 through 6-34. These are plotted in Figures 6-26, 6-27 and 6-28.

Table 6-32 The 11 extracted features of 40 MVA transformer's HV winding free buckling (Disk 1)

Feature		Fault level					
		1%	2%	3%	4%	5%	40%
Invariant moment	1(Φ1)	0.6723	0.6745	0.6767	0.6783	0.6791	0.7015
	2(Φ2)	0.0000	0.0000	0.0000	0.0000	0.0000	0.0000
	3(Φ3)	0.0038	0.0036	0.0035	0.0032	0.0031	0.0013
	4(Φ4)	-0.0712	-0.0719	-0.0723	-0.0728	-0.0734	-0.0816
	5(Φ5)	3.4179	3.4267	3.4376	3.4496	3.4576	3.6175
	6(Φ6)	1.0983	1.0985	1.0986	1.0987	1.0989	1.1064
	7(Φ7)	2.4389	2.4371	2.4363	2.4354	2.4322	2.4087
Texture analysis	8(τ_1)	0.0539	0.0537	0.0535	0.0534	0.0531	0.0498
	9(τ_2)	2.0002	2.0005	2.0008	2.0011	2.0016	2.0053
	10(τ_3)	1.8934	1.8938	1.8955	1.8967	1.8989	1.9682
	11(τ_4)	0.5531	0.5549	0.5562	0.5571	0.5578	0.5889
RMS		1.57215	1.573873	1.576275	1.578795	1.580303	1.619634
IED		0.281049	0.28993	0.300165	0.311271	0.320055	0.488266

Table 6-33 The 11 extracted features of 40 MVA transformer’s HV winding free buckling (Disk 5)

Feature		Fault level					
		1%	2%	3%	4%	5%	40%
Invariant moment	1(Φ1)	0.6827	0.6834	0.6858	0.6878	0.6892	0.7045
	2(Φ2)	0.0000	0.0000	0.0000	0.0000	0.0000	0.0000
	3(Φ3)	0.0029	0.0027	0.0026	0.0023	0.0022	0.0012
	4(Φ4)	-0.0735	-0.0741	-0.0748	-0.0752	-0.0758	-0.0837
	5(Φ5)	3.4672	3.4762	3.4873	3.4969	3.5173	3.6375
	6(Φ6)	1.0992	1.0994	1.0995	1.0997	1.0999	1.1073
	7(Φ7)	2.4276	2.4255	2.4249	2.4235	2.4217	2.4054
Texture analysis	8(τ_1)	0.0528	0.0526	0.0524	0.0523	0.0522	0.0483
	9(τ_2)	2.0023	2.0025	2.0026	2.0027	2.0029	2.0061
	10(τ_3)	1.9012	1.9024	1.9056	1.9067	1.9089	1.9782
	11(τ_4)	0.5619	0.5635	0.5649	0.5669	0.5685	0.5929
RMS		1.582195	1.583944	1.586586	1.5886	1.592824	1.624762
IED		0.331635	0.340728	0.351494	0.361095	0.380253	0.510495

Table 6-34 The 11 extracted features of 40 MVA transformer’s HV winding free buckling (Disk 10)

Feature		Fault level					
		1%	2%	3%	4%	5%	40%
Invariant moment	1(Φ1)	0.6909	0.6928	0.6943	0.6962	0.6987	0.7078
	2(Φ2)	0.0000	0.0000	0.0000	0.0000	0.0000	0.0000
	3(Φ3)	0.0019	0.0018	0.0017	0.0015	0.0014	0.0011
	4(Φ4)	-0.0761	-0.0767	-0.0772	-0.0779	-0.0784	-0.0854
	5(Φ5)	3.5274	3.5371	3.5483	3.5567	3.5696	3.6482
	6(Φ6)	1.1002	1.1004	1.1005	1.1006	1.1009	1.1085
	7(Φ7)	2.4191	2.4176	2.4158	2.4142	2.4126	2.4026
Texture analysis	8(τ_1)	0.0517	0.0516	0.0515	0.0513	0.0511	0.0475
	9(τ_2)	2.0032	2.0034	2.0036	2.0037	2.0035	2.0068
	10(τ_3)	1.9162	1.9167	1.9179	1.9181	1.9182	1.9882
	11(τ_4)	0.5736	0.5736	0.5765	0.5772	0.5791	0.5978
RMS		1.595576	1.597488	1.599812	1.601428	1.603986	1.628125
IED		0.391897	0.401446	0.412775	0.421305	0.434006	0.52456

As observed in the previous case study, the three parameters increase along with the increase in fault level. They also increase when the fault moves toward the bottom of the windings. The results reveal that the fault level and location can be identified and quantified using the proposed approach.

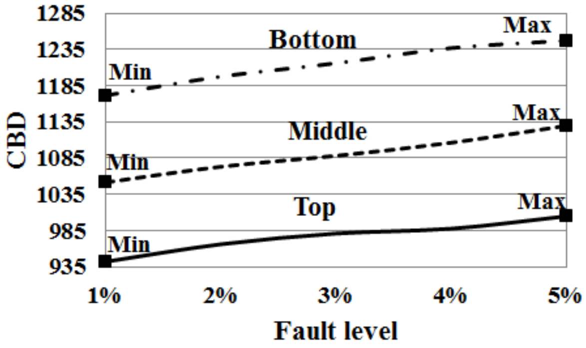

Figure 6-26 CBD trend for the 40 MVA transformer’s HV winding free buckling

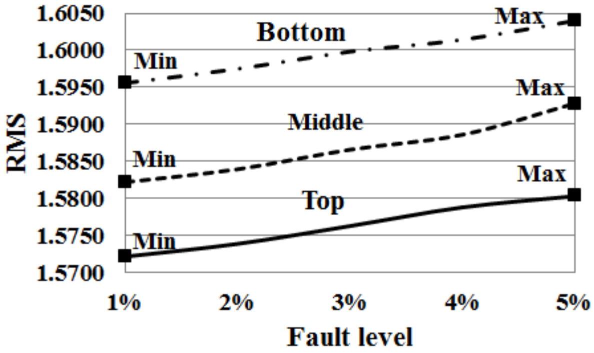

Figure 6-27 RMS trend for the 40 MVA transformer’s HV winding free buckling

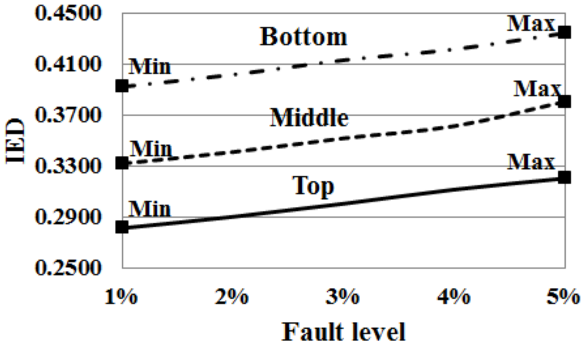

Figure 6-28 IED trend for the 40 MVA transformer’s HV winding free buckling

6:6 Case Study 3: Axial Displacement Fault

Using the FRA technique, this section investigates the impact of axial displacement at minor levels and is based on the proposed DIP application.

6:6:1 Axial Displacement (10 kVA Transformer)

The impact of axial displacement is obtained at 1% to 5% fault levels on the FRA polar plot signature of the 10 kVA transformer's HV and LV windings. For all minor levels of axial displacement, polar plots are analysed using the developed DIP techniques to extract various image features as given in Tables 6-35, 6-36, 6-37 and 6-38.

Table 6-35 Geometric dimension features of 10 kVA transformer's HV winding axial displacement

Feature		**Fault level**				
		1%	**2%**	**3%**	**4%**	**5%**
g1		**30514**	**30534**	**30548**	**30557**	**30568**
g2		**881.06**	**881.15**	**881.27**	**881.39**	**881.48**
g3	**X-axis**	**361.21**	**361.75**	**362.34**	**362.83**	**363.24**
	Y-axis	**291.03**	**291.14**	**291.26**	**291.35**	**291.46**
g4	**Major**	**377.13**	**377.84**	**378.26**	**378.92**	**379.73**
	Minor	**110.32**	**110.37**	**110.41**	**110.49**	**110.55**
CBD		**80.06**	**101.56**	**116.85**	**127.29**	**139.77**

Table 6-36 Geometric dimension features of 10 kVA transformer's LV winding axial displacement

Feature		**Fault level**				
		1%	**2%**	**3%**	**4%**	**5%**
g1		**9784**	**9813**	**9846**	**9886**	**9916**
g2		**494.71**	**495.08**	**495.66**	**496.29**	**496.71**
g3	**X-axis**	**340.07**	**340.25**	**340.38**	**340.46**	**340.68**
	Y-axis	**291.21**	**291.84**	**292.06**	**292.52**	**292.93**
g4	**Major**	**222.03**	**222.31**	**222.45**	**222.67**	**222.89**
	Minor	**60.76**	**60.92**	**61.09**	**61.21**	**61.34**
CBD		**188.94**	**219.56**	**253.8**	**295.31**	**326.71**

Tables 6-35 and 6-36 show that the four geometric dimension features increase along with the increase in fault level. Tables 6-37 and 6-38 show that, along with the increase in fault level, Features 1, 5, 6, 9, 10 and 11 decrease and Features 3, 4, 7, and 8 increase. Feature 2 is maintained at a constant zero value.

Table 6-37 The 11 extracted features of 10 kVA transformer's HV winding axial displacement

Feature		Fault level				
		1%	2%	3%	4%	5%
Invariant moment	1(Φ1)	0.2684	0.2651	0.2627	0.2594	0.2563
	2(Φ2)	0.0000	0.0000	0.0000	0.0000	0.0000
	3(Φ3)	0.0018	0.0022	0.0023	0.0024	0.0025
	4(Φ4)	-0.0083	-0.0085	-0.0087	-0.0088	-0.0089
	5(Φ5)	0.6195	0.6186	0.6172	0.6161	0.6153
	6(Φ6)	0.0948	0.0934	0.0921	0.0913	0.0905
	7(Φ7)	0.5481	0.5483	0.5485	0.5487	0.5489
Texture analysis	8(τ_1)	0.0824	0.0829	0.0835	0.0838	0.0844
	9(τ_2)	1.9282	1.9275	1.9261	1.9253	1.9226
	10(τ_3)	1.7895	1.7883	1.7872	1.7864	1.7851
	11(τ_4)	0.4683	0.4675	0.4655	0.4646	0.4631
RMS		0.848081	0.847514	0.846757	0.846234	0.845222
IED		0.058820	0.061957	0.065626	0.068768	0.073257

Table 6-38 The 11 extracted features of 10 kVA transformer's LV winding axial displacement

Feature		Fault level				
		1%	2%	3%	4%	5%
Invariant moment	1(Φ1)	0.4679	0.4661	0.4572	0.4537	0.4513
	2(Φ2)	0.0000	0.0000	0.0000	0.0000	0.0000
	3(Φ3)	0.0018	0.0020	0.0021	0.0022	0.0023
	4(Φ4)	-0.0078	-0.0079	-0.0081	-0.0082	-0.0084
	5(Φ5)	1.6813	1.6673	1.6446	1.6371	1.6257
	6(Φ6)	0.4182	0.4172	0.4158	0.4143	0.4127
	7(Φ7)	1.4529	1.4545	1.4572	1.4584	1.4595
Texture analysis	8(τ_1)	0.0621	0.0624	0.0629	0.0631	0.0634
	9(τ_2)	1.9689	1.9673	1.9666	1.9651	1.9637
	10(τ_3)	1.8568	1.8557	1.8535	1.8522	1.8513
	11(τ_4)	0.5058	0.5043	0.5022	0.5010	0.5004
RMS		1.083577	1.081200	1.077424	1.075844	1.073861
IED		0.060020	0.073880	0.097497	0.105916	0.117762

The CBD, RMS and IED values are calculated based on the extracted features and are depicted in Figures 6-29 through 6-34. As can be seen in these figures, the CBD and IED metrics increase, while the RMS metric decreases, along with the increase in the axial displacement level, which can be used to quantify the fault level. The figures also show the proposed threshold limits for the three metrics in which a minor axial displacement is considered only if at least one of the three metrics lies between its designated minimum and maximum limits. If any metric exceeds its designated maximum limit, a major AD may be reported. All calculated metrics should be less than the minimum limit to report an insignificant fault level.

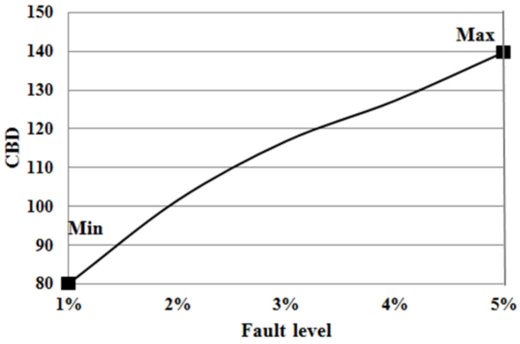

Figure 6-29 CBD trend for the 10 kVA transformer's HV winding AD

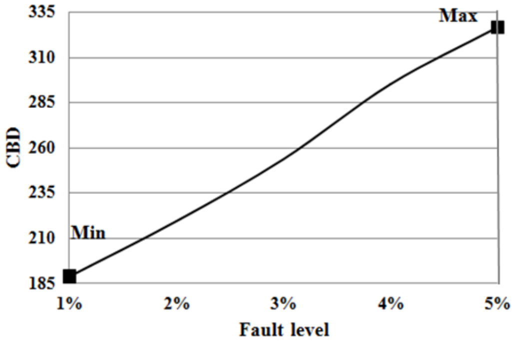

Figure 6-30 CBD trend for the 10 kVA transformer's LV winding AD

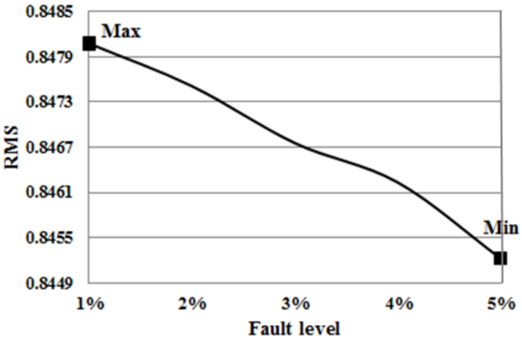

Figure 6-31 RMS trend for the 10 kVA transformer's HV winding AD

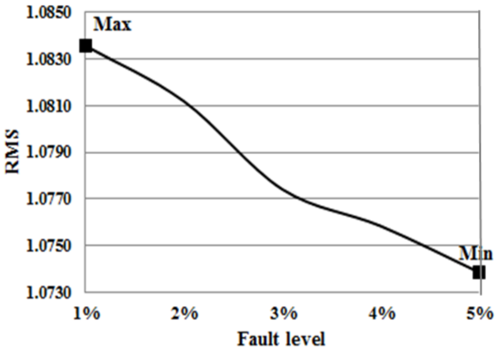

Figure 6-32 RMS trend for the 10 kVA transformer’s LV winding AD

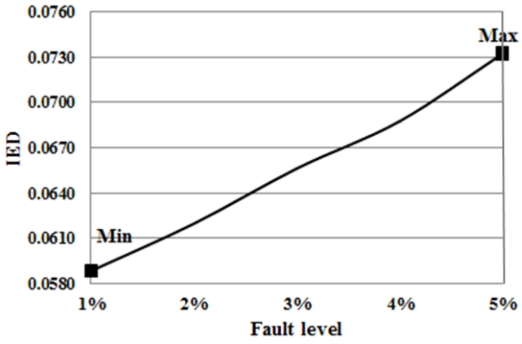

Figure 6-33 IED trend for the 10 kVA transformer’s HV winding AD

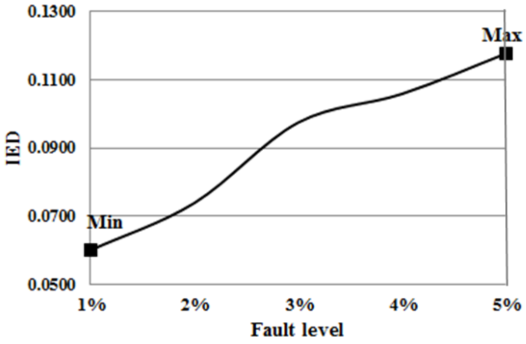

Figure 6-34 IED trend for the 10 kVA transformer’s LV winding AD

6:6:2 Axial Displacement (40 MVA Transformer)

An AD fault with five minor levels (1% to 5%) is simulated using FEA on phase A of the 40 MVA transformer’s HV and LV windings, and the corresponding FRA polar plot signature for each investigated fault is obtained.

Table 6-39 Geometric dimension features of 40 transformer's MVA HV winding AD

Feature		Fault level				
		1%	2%	3%	4%	5%
g1		67226	67432	67588	67694	67791
g2		1895.09	1895.28	1895.37	1895.64	1895.75
g3	X-axis	745.34	746.52	747.67	748.28	749.73
	Y-axis	622.76	623.86	624.37	625.18	626.59
g4	Major	846.28	846.46	846.69	847.22	847.57
	Minor	210.14	210.39	210.58	210.74	210.96
CBD		1296.79	1505.69	1663.86	1772.24	1872.78

Table 6-40 Geometric dimension features of 40 MVA transformer's LV winding AD

Feature		Fault level				
		1%	2%	3%	4%	5%
g1		48854	48886	48917	48967	48993
g2		1476.13	1476.32	1476.48	1476.67	1476.92
g3	X-axis	675.07	675.48	675.83	676.27	676.85
	Y-axis	565.41	565.52	565.63	565.77	565.94
g4	Major	645.34	646.27	647.15	648.52	649.86
	Minor	129.16	129.37	129.46	129.71	129.83
CBD		1176.95	1210.8	1243.39	1295.78	1324.24

Table 6-41 The 11 extracted features of 40 MVA transformer's HV winding AD

Feature		Fault level				
		1%	2%	3%	4%	5%
Invariant moment	1(Φ_1)	0.5992	0.5974	0.5958	0.5931	0.5907
	2(Φ2)	0.0000	0.0000	0.0000	0.0000	0.0000
	3(Φ_3)	0.0124	0.0176	0.0226	0.0289	0.0319
	4(Φ_4)	-0.0458	-0.0468	-0.0473	-0.0482	-0.0494
	5(Φ_5)	3.1684	3.1675	3.1664	3.1652	3.1638
	6(Φ_6)	1.0895	1.0884	1.0876	1.0861	1.0838
	7(Φ_7)	2.5952	2.5968	2.5976	2.5985	2.5992
Texture analysis	8(τ_1)	0.0643	0.0657	0.0662	0.0673	0.0684
	9(τ_2)	1.9624	1.9622	1.9617	1.9611	1.9605
	10(τ_3)	1.8625	1.8621	1.8618	1.8615	1.8611
	11(τ_4)	0.5121	0.5118	0.5116	0.5114	0.5111
RMS		1.534702	1.534581	1.534301	1.533930	1.533434
IED		0.042565	0.046361	0.049857	0.055179	0.059580

Table 6-42 The 11 extracted features of 40 MVA transformer's LV winding AD

Feature		Fault level				
		1%	2%	3%	4%	5%
Invariant moment	1(Φ_1)	0.8076	0.8012	0.7986	0.7932	0.7907
	2(Φ2)	0.0000	0.0000	0.0000	0.0000	0.0000
	3(Φ_3)	0.0157	0.0189	0.0208	0.0235	0.0276
	4(Φ_4)	-0.0414	-0.0422	-0.0445	-0.0457	-0.0467
	5(Φ_5)	5.2764	5.2742	5.2731	5.2722	5.2708
	6(Φ_6)	2.3386	2.3375	2.3364	2.3342	2.3321
	7(Φ_7)	4.3237	4.3256	4.3282	4.3327	4.3358
Texture analysis	8(τ_1)	0.0559	0.0589	0.0612	0.0656	0.0687
	9(τ_2)	1.9592	1.9581	1.9573	1.9555	1.9524
	10(τ_3)	1.8679	1.8663	1.8658	1.8631	1.8617
	11(τ_4)	0.5287	0.5276	0.5252	0.5245	0.5231
RMS		2.340710	2.340067	2.339962	2.339837	2.339454
IED		0.032238	0.038028	0.042318	0.050006	0.057177

The signatures are analysed using the developed DIP techniques to extract 15 features of the polar plot image as given in Tables 6-39, 6-40, 6-41 and 6-42. The trend of the 40 MVA transformer's extracted features is similar to the trend of the 10 kVA transformer's extracted features, however, the extracted features are larger in the case of the 40 MVA transformer. The threshold minimum and maximum levels of the three calculated metrics are illustrated in Figures 6-35 through 6-40. These figures show that while the CBD and IED metrics increase along with the increase in fault level, the RMS metric decreases. This is similar to the trend seen in the case of 10 kVA transformer.

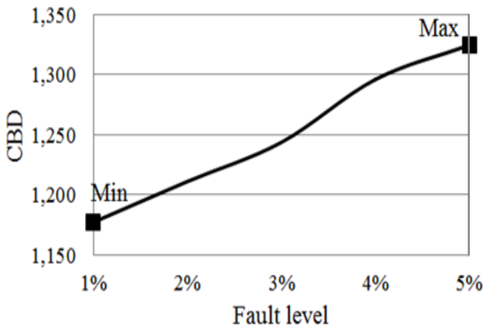

Figure 6-35 CBD trend for the 40 MVA transformer's HV winding AD

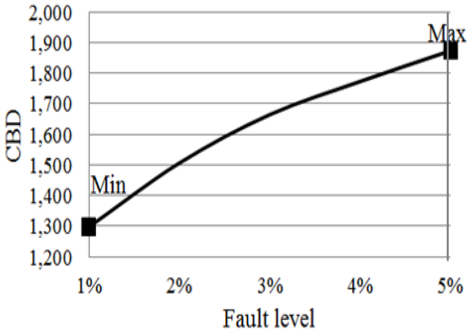

Figure 6-36 CBD trend for the 40 MVA transformer’s LV winding AD

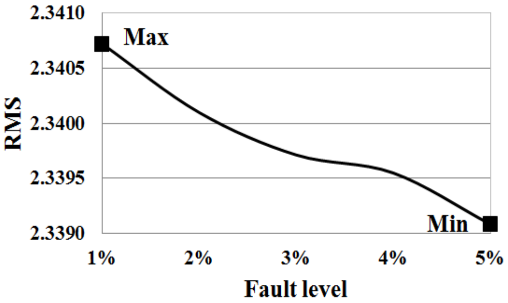

Figure 6-37 RMS trend for the 40 MVA transformer’s HV winding AD

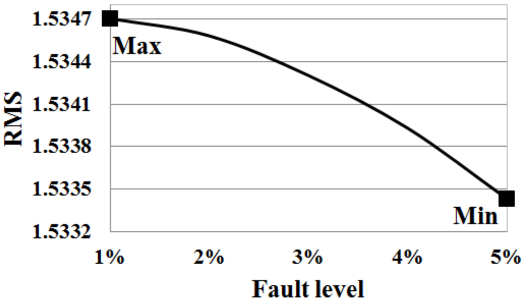

Figure 6-38 RMS trend for the 40 MVA transformer’s LV winding AD

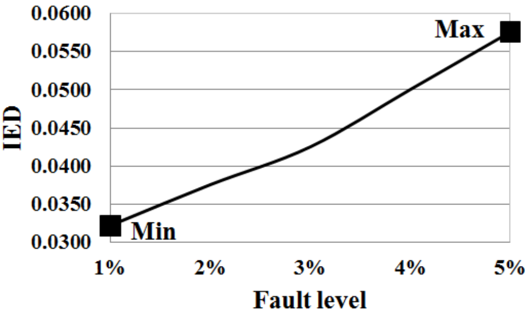

Figure 6-39 IED trend for the 40 MVA transformer’s HV winding AD

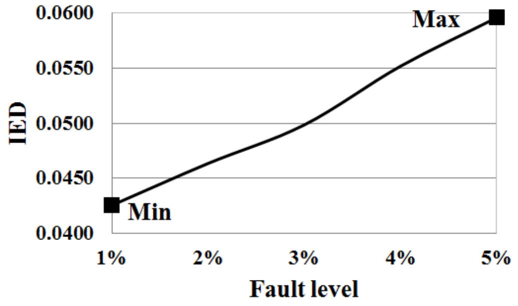

Figure 6-40 IED trend for the 40 MVA transformer's LV winding AD

6:6:3 Disk Space Variation (10 kVA Transformer)

Table 6-43 Geometric dimension features of 10 kVA transformer's HV winding DSV (Disk 1)

Feature		Fault level				
		1%	2%	3%	4%	5%
g1		30450	30453	30455	30457	30458
g2		879.02	879.04	879.05	879.06	879.08
g3	X-axis	358.92	358.94	358.95	358.97	358.98
	Y-axis	290.02	290.03	290.05	290.07	290.08
g4	Major	375.14	375.16	375.17	375.19	375.2
	Minor	109.42	109.43	109.45	109.47	109.48
CBD		7.83	10.91	12.98	15.07	16.13

Table 6-44 Geometric dimension features of 10 kVA transformer's HV winding DSV (Disk 3)

Feature		Fault level				
		1%	2%	3%	4%	5%
g1		30462	30464	30465	30467	30469
g2		879.13	879.14	879.16	879.18	879.19
g3	X-axis	359.02	359.03	359.05	359.06	359.08
	Y-axis	290.10	290.13	290.15	290.17	290.19
g4	Major	375.23	375.25	375.26	375.28	375.29
	Minor	109.51	109.52	109.54	109.56	109.58
CBD		20.3	22.38	23.47	25.56	27.64

The impacts of a disk space variation fault of the same levels and locations as in Chapter 5 are obtained from the proposed polar plot signature. Using the developed

DIP techniques, the geometric dimension features and the 11 combined features of invariant moment and texture analysis techniques are extracted as shown in Tables 6-43 through 6-48. These tables indicate that the extracted features in this case study follow a similar trend to that of the AD fault where CBD and IED values increase and the RMS metric decreases along with the increase in DSV fault level.

Table 6-45 Geometric dimension features of 10 kVA transformer's HV winding DSV (Disk 6)

Feature		Fault level				
		1%	2%	3%	4%	5%
g1		30471	30473	30475	30478	30479
g2		879.23	879.24	879.25	879.27	879.29
g3	X-axis	359.11	359.12	359.15	359.17	359.19
	Y-axis	290.22	290.24	290.25	290.28	290.29
g4	Major	375.31	375.33	375.35	375.37	375.38
	Minor	109.60	109.62	109.64	109.66	109.69
CBD		29.78	31.86	33.95	37.06	38.15

Table 6-46 The 11 extracted features of 10 kVA transformer's HV winding DSV (Disk 1)

Feature		Fault level				
		1%	2%	3%	4%	5%
Invariant moment	1(Φ_1)	0.2921	0.2919	0.2918	0.2917	0.2916
	2(Φ2)	0.0000	0.0000	0.0000	0.0000	0.0000
	3(Φ_3)	0.0017	0.0019	0.0021	0.0022	0.0023
	4(Φ_4)	-0.0052	-0.0055	-0.0056	-0.0058	-0.0059
	5(Φ_5)	0.6357	0.6356	0.6355	0.6354	0.6353
	6(Φ_6)	0.0978	0.0976	0.0975	0.0973	0.0972
	7(Φ_7)	0.5424	0.5426	0.5428	0.5429	0.5431
Texture analysis	8(τ_1)	0.0781	0.0783	0.0784	0.0786	0.0788
	9(τ_2)	1.9608	1.9607	1.9605	1.9603	1.9602
	10(τ_3)	1.8220	1.8219	1.8217	1.8216	1.8215
	11(τ_4)	0.4863	0.4859	0.4855	0.4847	0.4842
RMS		0.863410	0.863348	0.863249	0.863143	0.863081
IED		0.001631	0.002131	0.002666	0.003524	0.004133

Table 6-47 The 11 extracted features of 10 kVA transformer’s HV winding DSV (Disk 3)

Feature		Fault level				
		1%	2%	3%	4%	5%
Invariant moment	1(Φ_1)	0.2897	0.2892	0.2886	0.2881	0.2877
	2(Φ2)	0.0000	0.0000	0.0000	0.0000	0.0000
	3(Φ_3)	0.0025	0.0026	0.0027	0.0028	0.0029
	4(Φ_4)	-0.0061	-0.0062	-0.0064	-0.0065	-0.0066
	5(Φ_5)	0.6348	0.6346	0.6345	0.6344	0.6341
	6(Φ_6)	0.0969	0.0968	0.0966	0.0965	0.0963
	7(Φ_7)	0.5434	0.5436	0.5437	0.5439	0.5442
Texture analysis	8(τ_1)	0.0793	0.0794	0.0797	0.0798	0.0799
	9(τ_2)	1.9598	1.9596	1.9595	1.9593	1.9592
	10(τ_3)	1.8212	1.821	1.8208	1.8206	1.8202
	11(τ_4)	0.4839	0.4837	0.4836	0.4834	0.4832
RMS		0.862852	0.862745	0.862662	0.862562	0.862438
IED		0.005696	0.006332	0.006994	0.007633	0.008311

Table 6-48 The 11 extracted features of 10 kVA transformer’s HV winding DSV (Disk 6)

Feature		Fault level				
		1%	2%	3%	4%	5%
Invariant moment	1(Φ_1)	0.2865	0.2854	0.2837	0.2831	0.2819
	2(Φ2)	0.0000	0.0000	0.0000	0.0000	0.0000
	3(Φ_3)	0.0031	0.0032	0.0034	0.0035	0.0036
	4(Φ_4)	-0.0068	-0.0069	-0.0071	-0.0072	-0.0074
	5(Φ_5)	0.6337	0.6335	0.6334	0.6332	0.6330
	6(Φ_6)	0.0957	0.0956	0.0954	0.0952	0.0951
	7(Φ_7)	0.5446	0.5447	0.5449	0.5452	0.5453
Texture analysis	8(τ_1)	0.0803	0.0805	0.0806	0.0809	0.0811
	9(τ_2)	1.9587	1.9586	1.9584	1.9582	1.9581
	10(τ_3)	1.8197	1.8196	1.8194	1.8193	1.8191
	11(τ_4)	0.4829	0.4827	0.4826	0.4824	0.4821
RMS		0.862181	0.862091	0.861959	0.861875	0.861758
IED		0.009898	0.010932	0.012455	0.013274	0.014516

As shown in Figures 6-41, 6-42 and 6-43, the value of the CBD and IED metrics increase, while RMS decreases, when the fault moves toward the bottom of the winding. These figures also show the proposed threshold limits that can be used to identify the location and level of minor DSV faults, and reveal the ability of the proposed approach to identify the DSV fault location within the HV winding without any overlapping among the obtained metric trends. The results of the DIP technique show the same trend for the two investigated fault types (AD and DSV). However for the same fault level, the value of the CBD and IED is higher for the AD fault than for the DSV fault, and the RMS value is less for the AD fault. This is a key factor for distinguishing the two fault types.

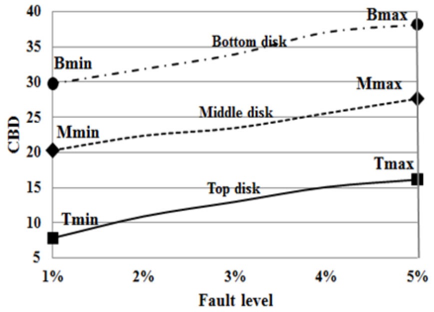

Figure 6-41 CBD trend for the 10 kVA transformer’s HV winding DSV

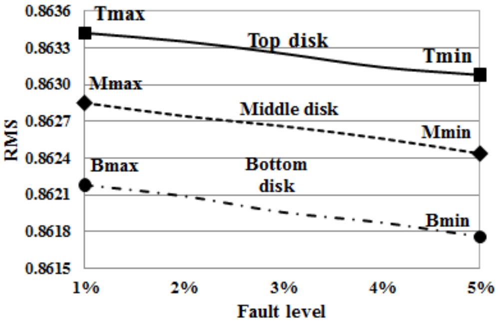

Figure 6-42 RMS trend for the 10 kVA transformer’s HV winding DSV

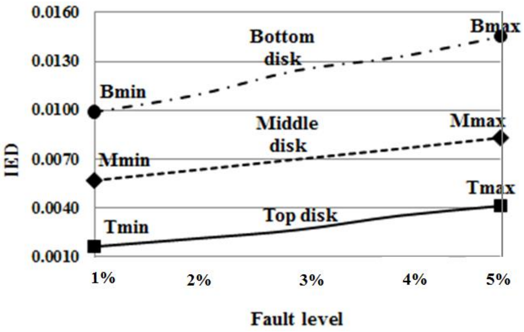

Figure 6-43 IED trend for the 10 kVA transformer’s HV winding DSV

6:6:4 Disk Space Variation (40 MVA Transformer)

The polar plot signatures of the DSV fault are obtained from five minor fault levels (1% to 5%) and at various locations including the top disk (Disk 1), the middle disk (Disk 5), and the bottom (Disk 10) of the 40 MVA transformer's HV winding. These signatures are then processed to extract the features for this case study as given in Tables 6-49 through 6-54. As shown in Figures 6-44, 6-45 and 6-46, the three metrics (CBD, RMS and IED) are calculated to identify the minimum and maximum threshold limits for each level/location of the DSV fault within the HV winding.

Table 6-49 Geometric dimension features of 40 MVA transformer's HV winding DSV (Disk 1)

Feature		Fault level				
		1%	2%	3%	4%	5%
g1		66101	66103	66105	66106	66108
g2		1838.21	1838.74	1839.17	1839.58	1839.93
g3	X-axis	674.82	675.82	676.82	677.82	678.82
	Y-axis	613.01	613.24	613.35	613.63	613.75
g4	Major	835.11	835.56	835.87	836.24	836.86
	Minor	200.04	200.28	200.37	200.45	200.52
CBD		13.37	17.82	21.76	24.9	29.06

Table 6-50 Geometric dimension features of 40 MVA transformer's HV winding DSV (Disk 5)

Feature		Fault level				
		1%	2%	3%	4%	5%
g1		66110	66113	66116	66117	66119
g2		1840.03	1840.57	1840.86	1842.12	1842.78
g3	X-axis	680.65	681.65	682.65	683.65	684.65
	Y-axis	614.14	614.26	614.43	614.57	614.82
g4	Major	837.19	837.77	838.05	838.63	838.97
	Minor	200.63	200.83	201.12	201.47	201.69
CBD		33.82	39.26	44.29	48.62	53.09

Table 6-51 Geometric dimension features of 40 MVA transformer's HV winding DSV (Disk 10)

Feature		Fault level				
		1%	2%	3%	4%	5%
g1		66122	66124	66125	66128	66129
g2		1843.1	1843.64	1844.89	1844.07	1844.62
g3	X-axis	691.65	692.65	694.65	695.65	698.65
	Y-axis	615.13	615.32	615.46	615.68	615.91
g4	Major	839.07	839.18	839.34	839.49	839.82
	Minor	201.73	201.96	202.17	202.23	202.55
CBD		63.86	67.93	72.69	76.3	81.73

Table 6-52 The 11 extracted features of 40 MVA transformer's HV winding DSV (Disk 1)

Feature		Fault level				
		1%	2%	3%	4%	5%
Invariant moment	1(Φ_1)	0.6205	0.6204	0.6203	0.6202	0.6201
	2(Φ2)	0.0000	0.0000	0.0000	0.0000	0.0000
	3(Φ_3)	0.0072	0.0073	0.0074	0.0075	0.0076
	4(Φ_4)	-0.0351	-0.0352	-0.0353	-0.0355	-0.0356
	5(Φ_5)	3.1859	3.1858	3.1856	3.1854	3.1853
	6(Φ_6)	1.0938	1.0937	1.0935	1.0933	1.0931
	7(Φ_7)	2.5772	2.5774	2.5775	2.5776	2.5778
Texture analysis	8(τ_1)	0.0575	0.0576	0.0577	0.0578	0.0579
	9(τ_2)	1.9712	1.9711	1.9709	1.9708	1.9707
	10(τ_3)	1.8662	1.8661	1.866	1.8659	1.8658
	11(τ_4)	0.5293	0.5292	0.5291	0.529	0.5289
RMS		1.538193	1.538169	1.538093	1.538029	1.537999
IED		0.003231	0.003428	0.003685	0.004044	0.004326

This confirms the ability of the proposed approach to detect the level and location of the DSV fault without overlapping the proposed limits. Similar to the analysis of the DSV fault for the 10 kVA transformer, the same trend for the calculated metrics is observed for each level and location, with larger values in the case of the 40 MVA transformer.

(b)

Table 6-53 The 11 extracted features of 40 MVA transformer's HV winding DSV (Disk 5)

Feature		Fault level				
		1%	2%	3%	4%	5%
Invariant moment	$1(\Phi_1)$	0.6199	0.6198	0.6197	0.6196	0.6195
	2(Φ2)	0.0000	0.0000	0.0000	0.0000	0.0000
	$3(\Phi_3)$	0.0081	0.0082	0.0084	0.0085	0.0087
	$4(\Phi_4)$	-0.0362	-0.0363	-0.0364	-0.0366	-0.0368
	$5(\Phi_5)$	3.1848	3.1847	3.1845	3.1844	3.1842
	$6(\Phi_6)$	1.0928	1.0926	1.0925	1.0924	1.0922
	$7(\Phi_7)$	2.5782	2.5784	2.5785	2.5787	2.5789
Texture analysis	$8(\tau_1)$	0.0581	0.0583	0.0584	0.0586	0.0587
	$9(\tau_2)$	1.9699	1.9698	1.9696	1.9695	1.9693
	$10(\tau_3)$	1.8656	1.8655	1.8654	1.8653	1.8652
	$11(\tau_4)$	0.5287	0.5286	0.5284	0.5283	0.5282
RMS		1.53782	1.53779	1.537718	1.537695	1.537635
IED		0.005492	0.005827	0.006196	0.006589	0.007080

Table 6-54 The 11 extracted features of 40 MVA transformer's HV winding DSV (Disk 10)

Feature		Fault level				
		1%	2%	3%	4%	5%
Invariant moment	$1(\Phi_1)$	0.6188	0.6187	0.6186	0.6184	0.6182
	2(Φ2)	0.0000	0.0000	0.0000	0.0000	0.0000
	$3(\Phi_3)$	0.0093	0.0095	0.0096	0.0097	0.0098
	$4(\Phi_4)$	-0.0372	-0.0374	-0.0375	-0.0376	-0.0377
	$5(\Phi_5)$	3.1839	3.1838	3.1837	3.1835	3.1834
	$6(\Phi_6)$	1.0917	1.0916	1.0915	1.0914	1.0912
	$7(\Phi_7)$	2.5793	2.5795	2.5796	2.5797	2.5799
Texture analysis	$8(\tau_1)$	0.0592	0.0593	0.0594	0.0596	0.0597
	$9(\tau_2)$	1.9688	1.9686	1.9685	1.9684	1.9683
	$10(\tau_3)$	1.8649	1.8648	1.8647	1.8645	1.8644
	$11(\tau_4)$	0.5279	0.5278	0.5276	0.5275	0.5273
RMS		1.537483	1.537448	1.537407	1.537335	1.537298
IED		0.008360	0.008804	0.009119	0.009513	0.009920

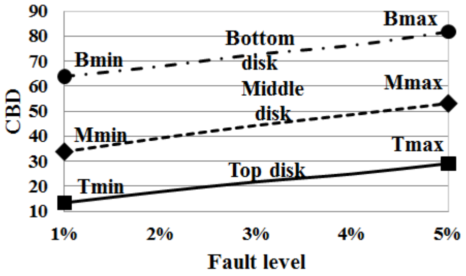

Figure 6-44 CBD trend for the 40 MVA transformer’s HV winding DSV

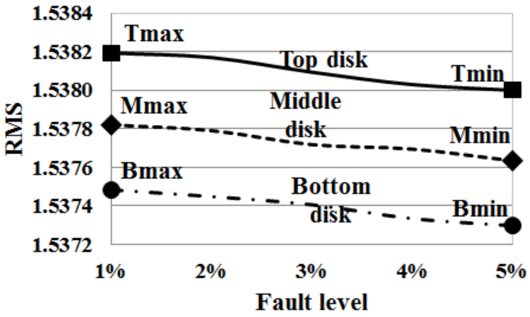

Figure 6-45 RMS trend for the 40 MVA transformer’s HV winding DSV

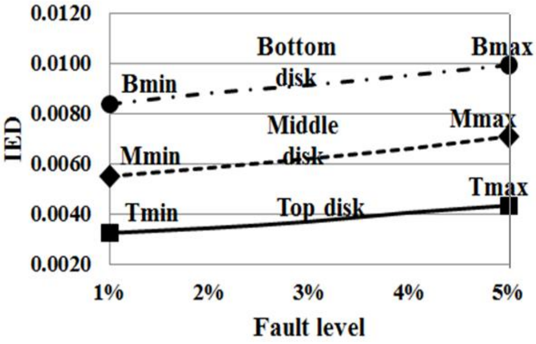

Figure 6-46 IED trend for the 40 MVA transformer’s HV winding DSV

In the case of overlapped values in any of the calculated metrics, the DSV fault location can be still identified as within the top, middle or bottom section of the winding. The chance of error when identifying the exact faulty disk within the winding is very small, because the height of each winding is also relatively small (14.14 x 3 cm in the case of the 10 kVA transformer and 40 x 3 cm in the case of the 40 MVA transformer).

6:7 Case Study 4: Bushing Fault

The previous case studies in Chapter 5, which investigated the impact of bushing faults within the 10 kVA and 40 MVA simulated transformer models using current FRA practice, are re-examined using the proposed DIP application. The FRA polar plot signatures for the same case studies are obtained and manipulated using the developed techniques to extract the proposed 15 image features as listed in Tables 6-55, 6-56, 6-57 and 6-58.

Table 6-55 Geometric dimension features of the10 kVA HV winding with bushings failure

Feature		Fault level				
		1%	2%	3%	4%	5%
g1		30671	30673	30675	30677	30678
g2		925.84	926.03	926.37	926.68	926.97
g3	X-axis	368.56	368.89	369.05	369.48	369.81
	Y-axis	297.46	297.79	298.12	298.56	298.93
g4	Major	397.14	397.32	397.48	397.61	397.78
	Minor	120.78	121.09	121.24	121.56	121.83
CBD		7.95	11.29	14.43	18.06	20.49

Table 6-56 Geometric dimension features of the 40 MVA HV winding with bushings failure

Feature		Fault level				
		1%	2%	3%	4%	5%
g1		66465	66467	66469	66472	66474
g2		2043.45	2043.89	2044.31	2044.62	2044.97
g3	X-axis	702.81	703.04	703.24	703.57	703.76
	Y-axis	644.88	645.11	645.34	645.57	645.71
g4	Major	882.12	882.33	882.46	882.58	882.71
	Minor	235.06	235.31	235.52	235.74	235.92
CBD		41.42	44.78	47.97	52.18	55.17

As can be seen in these tables, when complex permittivity and electrical conductivity increase from 1% to 5%, the four geometric features and seven invariant moment features for the two investigated transformers increase, while the four texture analysis features decrease.

Table 6-57 The 11 extracted features of the 10 kVA HV winding with bushings failure

Feature		Fault level				
		1%	2%	3%	4%	5%
Invariant moment	1(Φ_1)	0.3062	0.3069	0.3073	0.3077	0.3085
	2(Φ2)	0.0000	0.0000	0.0000	0.0000	0.0000
	3(Φ_3)	0.0031	0.0032	0.0034	0.0036	0.0037
	4(Φ_4)	-0.0111	-0.0114	-0.0115	-0.0116	-0.0118
	5(Φ_5)	1.1031	1.1045	1.1057	1.1069	1.1077
	6(Φ_6)	0.1012	0.1013	0.1015	0.1017	0.1018
	7(Φ_7)	1.0006	1.0009	1.0012	1.0013	1.0017
Texture analysis	8(τ_1)	0.0755	0.0751	0.0748	0.0746	0.0745
	9(τ_2)	1.9539	1.9538	1.9536	1.9533	1.9532
	10(τ_3)	1.8178	1.8176	1.8174	1.8173	1.8171
	11(τ_4)	0.4795	0.4794	0.4793	0.4792	0.4791
RMS		0.938078	0.938217	0.938309	0.938381	0.938471
IED		0.506414	0.507839	0.509076	0.510227	0.511152

Table 6-58 The 11 extracted features of the 40 MVA HV winding with bushings failure

Feature		Fault level				
		1%	2%	3%	4%	5%
Invariant moment	1(Φ_1)	0.6232	0.6234	0.6235	0.6237	0.6239
	2(Φ2)	0.0000	0.0000	0.0000	0.0000	0.0000
	3(Φ_3)	0.0083	0.0085	0.0086	0.0087	0.0089
	4(Φ_4)	-0.0432	-0.0434	-0.0436	-0.0437	-0.0438
	5(Φ_5)	3.2005	3.2013	3.2019	3.2021	3.2022
	6(Φ_6)	1.1842	1.1856	1.1863	1.1871	1.1884
	7(Φ_7)	2.7629	2.7632	2.7638	2.7643	2.7649
Texture analysis	8(τ_1)	0.0958	0.0956	0.0955	0.0953	0.0951
	9(τ_2)	1.9626	1.9623	1.9620	1.9618	1.9615
	10(τ_3)	1.8647	1.8644	1.8643	1.8641	1.8639
	11(τ_4)	0.5277	0.5275	0.5273	0.5271	0.5269
RMS		1.574975	1.575200	1.575407	1.575535	1.575683
IED		0.207094	0.208063	0.208979	0.209820	0.210971

The three proposed metric, CBD, RMD and IED, are calculated to detect any anomaly in the fingerprint features for each transformer. As can be observed in Tables 6-55 and 6-56, the CBD metric increases almost linearly along with the increase in bushing fault level. Also, at a given fault level, the CBD metric is significantly higher in the case of the 40 MVA transformer compared to the case of the 10 kVA transformer. Tables 6-57 and 6-58 show that the two remaining metrics (RMS and IED) increase only slightly along with the increase in fault level. It can also be observed that while the RMS values are higher in the case of the 40 MVA transformer, in the case of the 10 kVA transformer, the IED values are higher. Figure 6-47 shows the individual impacts of the 10 kVA and 40 MVA transformers with bushing failures on the CBD metric, which increases with the increase of the dielectric material level.

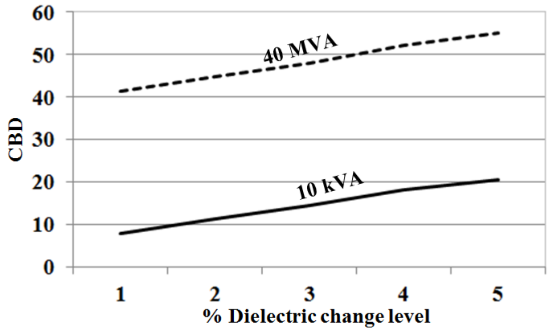

Figure 6-47 CBD metric trend for the 10 kVA and 40 MVA transformers with bushing fault levels

6:8 Case Study 5: Insulation System Degradation

As discussed in Chapter 5, the obtained FRA signature shows slight variation in the high frequency range due to insulating oil degradation. This variation, however, is extremely difficult to attribute to oil degradation, because it shows a similar trend to the impact of bushing faults in this frequency range. Using the same levels of mineral and vegetable oil degradation as Chapter 5, the proposed technique is used to manipulate the obtained polar plot signatures of the investigated transformers in order to extract the simulated 15 image features as shown in Tables 6-59 through 6-66.

Table 6-59 Geometric dimension features of the 10 kVA HV winding with mineral oil degradation

Feature		Fault level				
		1%	2%	3%	4%	5%
g1		31026	31028	31031	31033	31035
g2		947.13	948.34	949.41	950.07	951.62
g3	X-axis	377.04	377.37	377.69	378.28	378.89
	Y-axis	304.31	304.79	305.08	305.57	305.93
g4	Major	406.27	406.58	406.86	407.05	407.12
	Minor	125.03	125.19	125.27	125.38	125.51
CBD		412.95	417.44	422.48	426.52	431.24

Table 6-60 Geometric dimension features of the 40 MVA HV winding with mineral oil degradation

Feature		Fault level				
		1%	2%	3%	4%	5%
g1		67027	67031	67033	67035	67038
g2		2107.06	2108.15	2109.27	2110.43	2111.52
g3	X-axis	732.54	732.67	732.79	732.86	732.98
	Y-axis	689.07	689.46	689.88	690.11	690.36
g4	Major	906.03	906.12	906.36	906.48	906.56
	Minor	248.46	248.89	249.11	249.42	249.67
CBD		778.26	784.39	788.51	792.4	797.19

Table 6-61 The 11 extracted features of the 10 kVA HV winding with mineral oil degradation

Feature		Fault level				
		1%	2%	3%	4%	5%
Invariant moment	1(Φ_1)	0.3142	0.3152	0.3167	0.3182	0.3191
	2(Φ2)	0.0000	0.0000	0.0000	0.0000	0.0000
	3(Φ_3)	0.0051	0.0052	0.0053	0.0055	0.0057
	4(Φ_4)	-0.0189	-0.0191	-0.0193	-0.0195	-0.0197
	5(Φ_5)	1.1249	1.1256	1.1262	1.1267	1.1273
	6(Φ_6)	0.1539	0.1542	0.1544	0.1546	0.1548
	7(Φ_7)	1.0317	1.0325	1.0336	1.0349	1.0362
Texture analysis	8(τ_1)	0.0711	0.0709	0.0706	0.0704	0.0702
	9(τ_2)	1.9527	1.9525	1.9523	1.9521	1.9518
	10(τ_3)	1.8146	1.8143	1.8139	1.8137	1.8135
	11(τ_4)	0.4764	0.4762	0.476	0.4758	0.4756
RMS		0.943418	0.943508	0.943613	0.943763	0.943887
IED		0.542963	0.544035	0.545174	0.546317	0.547528

Table 6-62 The 11 extracted features of the 40 MVA HV winding with mineral oil degradation

Feature		Fault level				
		1%	2%	3%	4%	5%
Invariant moment	1(Φ_1)	0.6452	0.6468	0.6477	0.6485	0.6494
	2($\Phi2$)	0.0000	0.0000	0.0000	0.0000	0.0000
	3(Φ_3)	0.0102	0.0104	0.0105	0.0106	0.0107
	4(Φ_4)	-0.0568	-0.0572	-0.0575	-0.0579	-0.0583
	5(Φ_5)	3.3762	3.3764	3.3765	3.3767	3.3768
	6(Φ_6)	1.4351	1.4354	1.4358	1.4361	1.4366
	7(Φ_7)	2.9771	2.9773	2.9775	2.9778	2.9782
Texture analysis	8(τ_1)	0.0548	0.0546	0.0542	0.0537	0.0532
	9(τ_2)	1.9550	1.9547	1.9545	1.9542	1.9536
	10(τ_3)	1.8461	1.8458	1.8456	1.8453	1.8447
	11(τ_4)	0.5069	0.5067	0.5063	0.5058	0.5055
RMS		1.657792	1.657875	1.657936	1.657998	1.658020
IED		0.562476	0.563002	0.563541	0.564146	0.564928

Table 6-63 Geometric dimension features of the 10 kVA HV winding with vegetable oil degradation

Feature		Fault level				
		1%	2%	3%	4%	5%
g1		31334	31337	31341	31345	31348
g2		962.22	963.35	964.71	965.85	966.44
g3	X-axis	382.13	382.22	382.35	382.49	382.58
	Y-axis	306.75	306.86	307.09	307.28	307.43
g4	Major	409.62	409.75	409.92	410.15	410.34
	Minor	127.78	128.05	128.18	128.24	128.36
CBD		558.34	563.07	569.09	574.85	578.99

Table 6-64 Geometric dimension features of the 40 MVA HV winding with vegetable oil degradation

Feature		Fault level				
		1%	2%	3%	4%	5%
g1		67548	67550	67553	67555	67557
g2		2110.11	2111.28	2112.37	2113.49	2114.12
g3	X-axis	734.28	734.35	734.41	734.55	734.68
	Y-axis	690.36	690.86	691.12	691.49	691.76
g4	Major	908.56	908.83	909.04	909.34	909.68
	Minor	249.17	249.25	249.35	249.46	249.59
CBD		856.26	860.35	865.07	869.11	872.61

Table 6-65 The 11 extracted features of the 10 kVA HV winding with vegetable oil degradation

Feature		Fault level				
		1%	2%	3%	4%	5%
Invariant moment	1(Φ_1)	0.3422	0.3425	0.3428	0.3431	0.3433
	2(Φ2)	0.0000	0.0000	0.0000	0.0000	0.0000
	3(Φ_3)	0.0065	0.0066	0.0067	0.0068	0.0069
	4(Φ_4)	-0.0229	-0.0231	-0.0232	-0.0234	-0.0235
	5(Φ_5)	1.3413	1.3426	1.3435	1.3447	1.3459
	6(Φ_6)	0.2134	0.2136	0.2137	0.2138	0.2139
	7(Φ_7)	1.1013	1.1015	1.1016	1.1018	1.1019
Texture analysis	8(τ_1)	0.0656	0.0655	0.0653	0.0652	0.0651
	9(τ_2)	1.9219	1.9212	1.9209	1.9206	1.9202
	10(τ_3)	1.7978	1.7976	1.7974	1.7972	1.7969
	11(τ_4)	0.4427	0.4426	0.4425	0.4423	0.4422
RMS		0.967716	0.967750	0.967792	0.967880	0.967923
IED		0.105856	0.107295	0.108286	0.109588	0.110880

Table 6-66 The 11 extracted features of the 40 MVA HV winding with vegetable oil degradation

Feature		Fault level				
		1%	2%	3%	4%	5%
Invariant moment	1(Φ_1)	0.6717	0.6722	0.6728	0.6731	0.6734
	2(Φ2)	0.0000	0.0000	0.0000	0.0000	0.0000
	3(Φ_3)	0.0153	0.0155	0.0156	0.0157	0.0159
	4(Φ_4)	-0.0846	-0.0849	-0.0852	-0.0854	-0.0857
	5(Φ_5)	3.6472	3.6475	3.6478	3.6481	3.6483
	6(Φ_6)	1.8501	1.8504	1.8511	1.8518	1.8521
	7(Φ_7)	3.2163	3.2164	3.2166	3.2169	3.2171
Texture analysis	8(τ_1)	0.0115	0.0114	0.0112	0.0109	0.0107
	9(τ_2)	1.9262	1.9256	1.9244	1.9232	1.9225
	10(τ_3)	1.8276	1.8275	1.8273	1.8271	1.8269
	11(τ_4)	0.4848	0.4846	0.4845	0.4844	0.4842
RMS		1.779009	1.779055	1.779093	1.779136	1.779154
IED		0.182957	0.183576	0.184646	0.185776	0.186443

As can be observed from the above tables, the trend of the geometric features is similar to the case of the bushing faults. However, the values of the four geometric features are higher in the case of oil deterioration than in the corresponding features obtained for bushing failure. The results also show that while a slight increase can be observed in the invariant moment features, when the oil degradation level increases, there is a decrease in the texture analysis features. The values of the 11 texture analysis and invariant moment features are higher than the corresponding features of the bushing failure. In order to investigate the effect of oil type on the proposed polar plot technique, the impact of insulating vegetable oil degradation based on the obtained correlation in Chapter 4 (Figure 4-5) is implemented using FEA on both investigated transformers. The impact of various mineral and vegetable oil degradation levels (1% to 5%) on the 15 features extracted from the polar plot images is found to have a similar trend to the case of mineral oil degradation, except with higher values in all features. The three metrics (CBD, RMS and IED) are calculated using the extracted features to assist with the classification of oil degradation as listed in Tables 6-59 through 6-66. These tables show that the increase in oil degradation level results in an observable increase in the CBD value, and a slight increase in the RMS and IED values. The increasing range of these parameters is higher in the case of vegetable oil degradation than that of mineral oil.

To distinguish the impact of bushing failure from insulating oil degradation on the proposed polar plot, the two case studies investigated above can be compared. The extracted features show that the geometric dimensions and invariant moment features are higher in the case of oil degradation than the corresponding features obtained in the case of bushing failure. Vegetable oil degradation is recognised by the higher value of the extracted features from the geometric dimension and invariant moment analyses. On the other hand, the four texture features are found to be highest in the case of bushing failure, followed by mineral oil degradation, then vegetable oil degradation. Figure 6-48 shows the individual impacts of mineral and vegetable oil degradation on the CBD metric. At the same fault level, the CBD value for vegetable oil degradation is much higher than the corresponding value of mineral oil degradation.

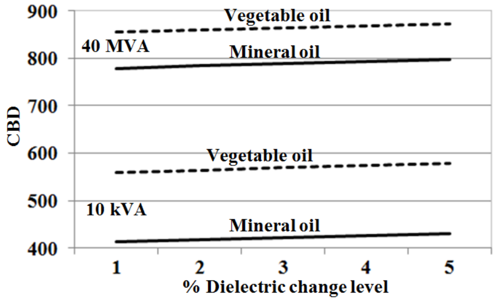

Figure 6-48 CBD metric trend for the 10 kVA and 40 MVA transformers with mineral and vegetable oil degradation levels

6:9 Case Study 6: Practical Validation

To investigate the feasibility of the proposed approach and validate the above simulation results, several practical measurements, based on the required test, fault type and availability, are conducted in the laboratory using different power transformers as illustrated below.

6:9:1 Practical Validation for Short Circuit Turns

A three-phase 7 kVA, 440/55V, 50Hz dry-type test transformer, which has several winding tap positions to facilitate a short circuiting portion of the winding, is simulated using finite element modelling and used for experimental measurements. A turn-to-turn short circuit is created at levels 1%, 3% and 5% within the low-voltage winding. A frequency response analyser is used to measure the healthy FRA signature along with the signature for each investigated short circuit fault level. Figure 6-49 shows the measured FRA signatures along with the FRA signatures obtained from the finite element model of the healthy investigated transformer when three short circuit levels (1% to 3%) take place within the LV winding. It can be seen that the practical and simulated results are in agreement. The slight difference between the practical and simulated results in both the mid and high frequency range is attributed to the inaccuracy of the transformer's parameters used in the FEA simulation.

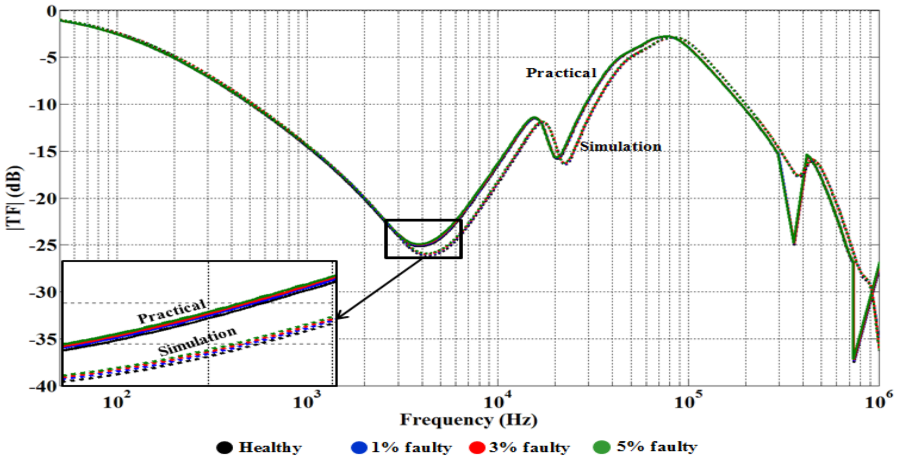

Figure 6-49 Impact of LV winding SC faults on conventional FRA signature (practical and simulated results of 7 kVA dry-type transformer)

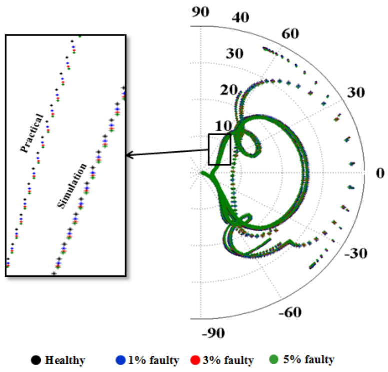

Figure 50 Impact of LV winding SC faults on polar plot signature (practical and simulated results of 7 kVA dry-type transformer)

As can be observed in Figure 6-49, it is extremely difficult to visually distinguish between the healthy and faulty signatures. Polar plot signatures (Figure 6-50) have been obtained and processed using the developed DIP code to extract image features. The geometric dimensions along with the 11 features of the invariant moment and texture analysis are extracted for experimental measurements and simulation analysis. They are respectively shown in Tables 6-67, 6-68, 6-69, and 6-70. Analysis of the extracted features indicates that the trend of the three metrics (CBD, RMS and IED) is similar to that of the two simulation case studies discussed above (Case Study 6.4).

Table 6-67 Geometric dimension features of the 7 kVA dry-type transformer's LV winding (practical)

Feature		Healthy	Fault level		
			1%	3%	5%
g1		5635	5614	5601	5572
g2		392.84	391.87	389.31	387.21
g3	X-axis	339.83	339.21	339.12	339.04
	Y-axis	284.84	283.47	282.41	281.86
g4	Major	152.16	151.78	150.32	149.63
	Minor	48.5	47.45	46.64	45.21
CBD		------	25.39	44.37	78.22

Table 6-68 Geometric dimension features of the 7 kVA dry-type transformer's LV winding (simulated)

Feature		Healthy	Fault level		
			1%	3%	5%
g1		5382	5373	5358	5337
g2		378.87	377.17	375.76	373.24
g3	X-axis	339.29	338.94	338.72	338.46
	Y-axis	281.37	280.74	280.67	280.63
g4	Major	148.64	146.06	144.23	142.13
	Minor	47.13	46.18	44.91	43.35
CBD		------	15.21	35.01	62.49

Table 6-69 The 11 extracted features of the 7 kVA dry-type transformer's LV winding (practical)

Feature		Healthy	Fault level		
			1%	3%	5%
Invariant moment	$1(\Phi_1)$	0.9585	0.9613	0.9629	0.9659
	$2(\Phi_2)$	0.0000	0.0000	0.0000	0.0000
	$3(\Phi_3)$	0.0012	0.0011	0.0008	0.0006
	$4(\Phi_4)$	-0.0105	-0.0103	-0.0101	-0.0090
	$5(\Phi_5)$	6.5234	6.5235	6.5237	6.5239
	$6(\Phi_6)$	3.1971	3.1972	3.1974	3.1977
	$7(\Phi_7)$	5.6516	5.6514	5.6510	5.6507
Texture analysis	$8(\tau_1)$	0.0505	0.0499	0.0496	0.0491
	$9(\tau_2)$	1.9747	1.9750	1.9755	1.9757
	$10(\tau_3)$	1.8813	1.8815	1.8819	1.8821
	$11(\tau_4)$	0.5449	0.5452	0.5458	0.5461
RMS		2.913508	2.913621	2.913723	2.913859
IED		------	0.002921	0.004779	0.007989

Table 6-70 The 11 extracted features of the 7 kVA dry-type transformer's LV winding (simulated)

Feature		Healthy	Fault level		
			1%	3%	5%
Invariant moment	1(Φ_1)	0.9819	0.9822	0.9861	0.9883
	2(Φ_2)	0.0000	0.0000	0.0000	0.0000
	3(Φ_3)	0.0013	0.0012	0.0007	0.0003
	4(Φ_4)	-0.0100	-0.0099	-0.0092	-0.0085
	5(Φ_5)	6.9486	6.9492	6.9494	6.9497
	6(Φ_6)	3.5143	3.5146	3.5149	3.5154
	7(Φ_7)	6.0362	6.0358	6.0356	6.0352
Texture analysis	8(τ_1)	0.0498	0.0496	0.0493	0.0490
	9(τ_2)	1.9751	1.9754	1.9758	1.9762
	10(τ_3)	1.8828	1.8831	1.8836	1.8838
	11(τ_4)	0.5494	0.5502	0.5504	0.5506
RMS		3.101078	3.101216	3.101418	3.10156
IED		------	0.001257	0.004731	0.007206

6:9:2 Practical Validation for Radial Deformation

The proposed approach is validated through experimental measurements on a 50Hz single phase 2 kVA, 250/120V dry type transformer. The transformer is also subjected to a practical forced radial buckling at fault levels of 3% and 8%.

A commercial sweep frequency response analyser is used to measure the FRA signatures both prior to and after the staging of investigated faults. Furthermore, a 3D-model of the investigated transformer is simulated using FEA to compare the simulated and practical results. Using practical measurements and FEA simulation, Figure 6-51 shows the FRA signatures of the investigated transformer in a healthy condition and when 3% and 8% levels of radial buckling take place within the LV winding. This figure also shows agreement between the practical and simulated measurements. The results also reveal the difficulty of identifying the fault using the current FRA approach. The polar plot signatures are obtained and processed using the proposed DIP code. The 15 features of the practical measured and simulation analysis signatures are obtained and used to calculate the three proposed metrics as listed in Tables 6-71 and 6-72.

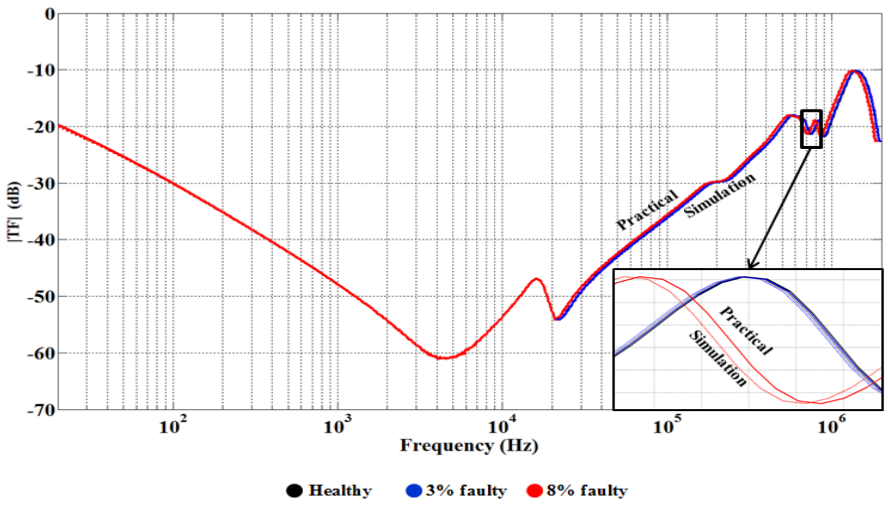

Figure 6-51 Conventional FRA signature using practical measurement and simulation analysis for the 2 kVA dry type transformer

Similar to the previous case study (Case Study 6.5), these metrics are increase when the radial buckling level increases. It can also be observed that the metrics values using practical measurement and simulation analysis are very close, revealing the feasibility of the proposed approach.

Table 6-71 Geometric dimension features of the 2 kVA dry type transformer's LV winding radial buckling (practical and simulated)

Feature		Practical			Simulated		
		Healthy	3%	8%	Healthy	3%	8%
g1		3246	3240	3159	3267	3261	3182
g2		231.21	230.31	224.55	238.36	237.25	231.32
g3	X-axis	248.69	247.21	241.03	252.21	251.71	245.44
	Y-axis	193.44	192.74	187.92	197.64	196.66	191.75
g4	Major	108.31	107.64	104.95	112.42	111.41	108.69
	Minor	32.32	31.41	30.62	36.64	35.12	34.23
CBD		------	10.66	111.9	------	11.12	110.84

Table 6-72 The 11 extracted features of the 2 kVA dry type transformer's LV winding radial buckling (practical and simulated)

Feature		Practical			Simulated		
		Healthy	3%	8%	Healthy	3%	8%
Invariant moment	1(Φ1)	0.2453	0.2492	0.2511	0.2481	0.2547	0.2593
	2(Φ_2)	0.0000	0.0000	0.0000	0.0000	0.0000	0.0000
	3(Φ_3)	0.0038	0.0033	0.0021	0.0042	0.0035	0.0023
	4(Φ_4)	-0.0566	-0.0452	-0.0404	-0.0578	-0.0541	-0.0504
	5(Φ_5)	2.4636	2.4654	2.4692	2.4721	2.4743	2.4787
	6(Φ_6)	1.8947	1.8961	1.9004	1.9071	1.9089	1.9109
	7(Φ_7)	3.2856	3.2841	3.2801	3.3356	3.3333	3.3312
Texture analysis	8(τ_1)	0.0732	0.0702	0.0652	0.0786	0.0752	0.0714
	9(τ_2)	2.1209	2.1217	2.1278	2.1311	2.1331	2.1362
	10(τ_3)	1.9062	1.9085	1.9143	1.9145	1.9216	1.9315
	11(τ_4)	0.5621	0.5628	0.5682	0.5927	0.5932	0.5989
RMS		1.62287344	1.62336673	0.012972664	1.637731718	1.638873316	1.640952876
IED		------	1.62512635	0.024647515	------	0.011718788	0.025815887

6:9:3 Practical Validation for Axial Deformation

To investigate the practical feasibility of the proposed approach and validate the simulation results of Case Study 6-6, a practical 5% AD fault is implemented on phase A of the LV winding of a scaled-down three phase delta-wye 7 kVA, 440/55V, 50Hz dry type transformer. The FRA polar plot signature is measured using a commercial frequency response analyser in both healthy and faulty winding conditions. The hardware transformer model is also simulated using FEA to compare the practical and simulated results. The obtained polar plots, using practical measurement and simulation analysis, are processed using the DIP code to extract the proposed 15 image features. These features are used to calculate the three proposed classification metrics. As can be observed in Tables 6-73 and 6-74, the trend of the three metrics (CBD, RMS and IED) is found to be similar to that of the 10 kVA and 40 MVA transformers investigated in Case Study 6-6.

Table 6-73 Geometric dimension features of the 7 kVA dry type transformer's LV winding AD (practical and simulated)

Feature		Practical		Simulated	
		Healthy	5%	Healthy	5%
g1		5635	5641	5382	5388
g2		392.84	393.75	378.87	379.54
g3	X-axis	339.83	340.21	339.29	339.95
	Y-axis	284.84	285.65	281.37	282.17
g4	Major	152.16	152.87	148.64	149.02
	Minor	48.5	48.91	47.13	47.87
CBD		------	9.22	------	9.25

Table 6-74 The 11 extracted features of the 7 kVA dry type transformer's LV winding AD (practical and simulated)

Feature		Practical		Simulated	
		Healthy	5%	Healthy	5%
Invariant moment	1(Φ_1)	0.9585	0.9579	0.9819	0.9811
	2(Φ_2)	0.0000	0.0000	0.0000	0.0000
	3(Φ_3)	0.0012	0.0016	0.0013	0.0019
	4(Φ_4)	-0.0105	-0.0113	-0.01	-0.0108
	5(Φ_5)	6.5234	6.5225	6.9486	6.9475
	6(Φ_6)	3.1971	3.1965	3.5143	3.5134
	7(Φ_7)	5.6516	5.6521	6.0362	6.0368
Texture analysis	8(τ_1)	0.0505	0.0512	0.0498	0.0508
	9(τ_2)	1.9747	1.9741	1.9751	1.9748
	10(τ_3)	1.8813	1.8808	1.8828	1.8822
	11(τ_4)	0.5449	0.5445	0.5494	0.5488
RMS		2.913507859	2.913263348	3.101078441	3.10078643
IED		------	0.001959592	------	0.00241454

6:9:4 Practical Validation for Bushing Oil Degradation

Moisture distribution within the transformer's insulation is of a dynamic nature because of the continuous water migration process between solid insulation and oil. This means that it is difficult to develop a consistent mathematical correlation between moisture content in insulating oil and moisture content in its dielectric permittivity [23]. To prove that by increasing the relative permittivity of insulating oil causes various oil degradation levels, practical measurements have been conducted. The measurements study the correlation between moisture and permittivity of transformer oil over 5 years as shown in Figure 6-52 [23]. The figure shows that the correlation between moisture content and oil relative permittivity is almost linear, and simulating moisture in oil by increasing its relative permittivity is an acceptable assumption.

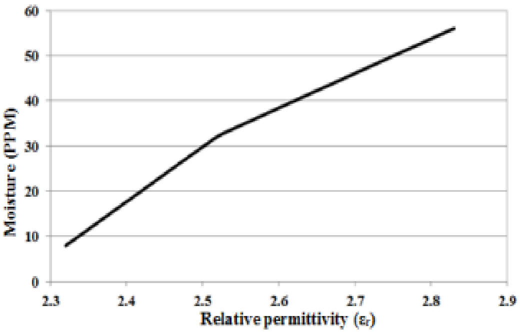

Figure 6-52 Practical measurement of the correlation between moisture and oil relative permittivity [12]

To validate the simulation results, obtained using the proposed polar plot signature, practical FRA measurement is conducted on a three-phase 132 kV, 35 MVA power transformer at an ambient temperature of 25^{o}C. The transformer bushing’s insulating oil is tested, and a 3% moisture content is detected in the HV bushing of phase A. As shown in Figure 6-52, FRA measurement is conducted on this phase and compared with the FRA signature of the same phase but with new oil.

Figure 6-53 reveals, where resonance peaks are slightly shifted to the left, that the impact of the bushing oil’s moisture content on the conventional FRA signature is obvious in the high frequency range. The shift is attributed to the increase in insulation capacitance, due to the existence of moisture. Consequently, all resonance frequencies in the high frequency range decrease where the capacitive components dominate the FRA characteristic. The practical measurements, shown in Figure 6-52, agree with the simulated results shown in Case Study 6-7. The proposed healthy and faulty (3% moisture content in HV bushing) polar plot signatures for the 35 MVA transformer are obtained from practical FRA measurements.

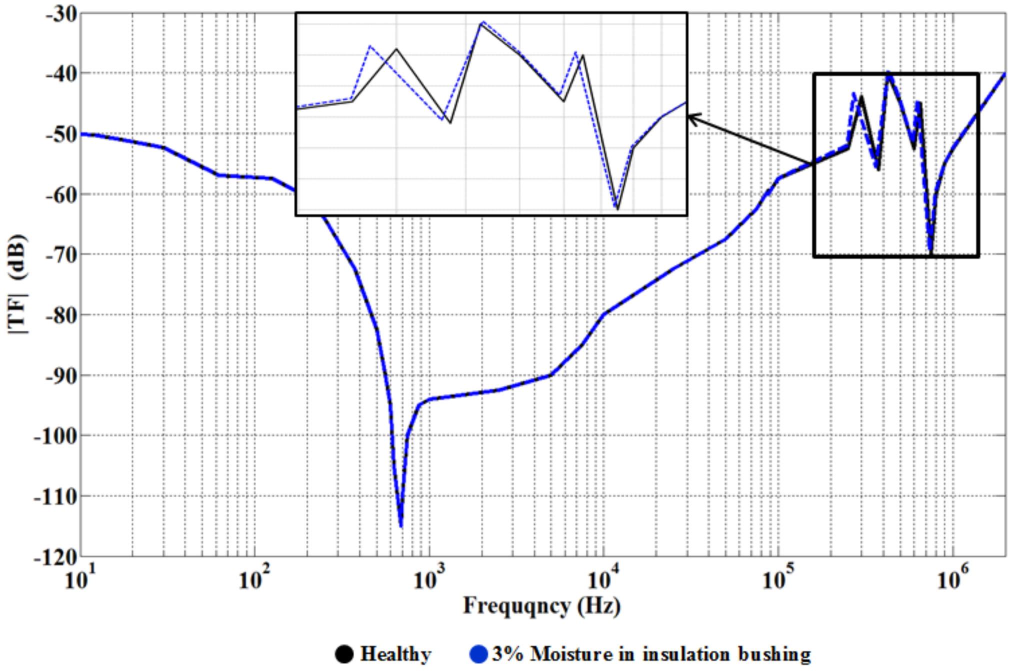

Figure 6-53 Impact of 3% moisture content in the HV bushing oil of 35 MVA transformer

The polar plots are then manipulated using the developed DIP codes to extract the proposed 15 image features. Similar to the simulation analysis, the same trend is observed in all features extracted from the practical signatures. These features are then used to calculate the three metrics (CBD, RMS and IED). The trend of these metrics is also similar to that of the modelled 10 kVA and 40 MVA transformers (Case Study 6-7) as can be seen in Figure 6-54.

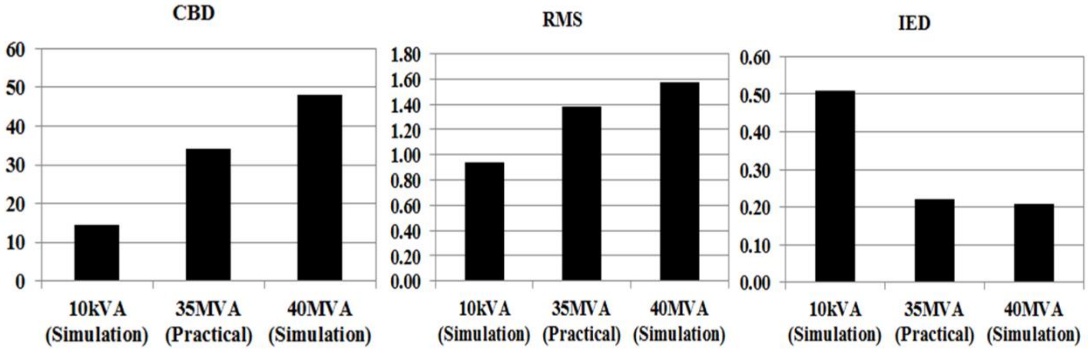

Figure 6-54 CBD, RMS and IED metrics for 3% moisture content in the bushing oil of 10 kVA, 35 MVA and 40 MVA transformers

6:10 Comparison Analysis

The threshold levels for the three classification metrics (CBD, RMS and IED) in all fault cases investigated in this thesis are proposed in the above sections where:

***Healthy signature*:** reported only if all three measured metrics are less than the minimum threshold of the minor fault level, which is 1%.

Minor fault: reported if at least one metric is located between the proposed minimum and maximum threshold limits.

Major fault: reported if at least one metric violates the maximum threshold level.

The following tables compare the threshold levels proposed for all investigated case studies for the LV and HV windings of the 10 kVA and 40 MVA transformers. As shown in these tables, there is no overlapping between the threshold bands of the three metrics within each case study. In some cases, the metrics of faults overlap, so in order to correctly identify and quantify the various faults, the three metrics should be combined. However, as discussed above, various faults can be distinguished by looking at the extracted features individually.

Table 6-75 Threshold levels for minor SC faults levels (1% to 5%) in 10 kVA and 40 MVA transformers

Fault location		Short circuit turns faults					
		CBD		RMS		IED	
		Min	Max	Min	Max	Min	Max
10 kVA	LV	7.76	154.23	1.096004	1.097390	0.025059	0.040158
	HV/Top	5.59	39.19	0.872592	0.873590	0.048710	0.055358
	HV/Middle	52.67	90.78	0.874080	0.875160	0.059371	0.067228
	HV/Bottom	96.05	162.36	0.875582	0.875160	0.070316	0.078710
40 MVA	LV	11.53	82.44	2.395078	2.409629	0.225213	0.292433
	HV/Top	120.10	191.43	1.538625	1.539514	0.011122	0.020432
	HV/Middle	459.94	552.53	1.542315	1.543488	0.048348	0.055787
	HV/Bottom	691.21	776.56	1.565419	1.097390	0.152844	0.158306

Table 6-76 Threshold levels for minor AD and DSV faults levels (1% to 5%) in 10 kVA and 40 MVA transformers

Fault location		AD					
		CBD		RMS		IED	
		Min	Max	Min	Max	Min	Max
10 kVA	LV	188.94	326.71	1.083577	1.073861	0.060020	0.117762
	HV	80.06	139.77	0.848081	0.845222	0.058820	0.073257
40 MVA	LV	1176.95	1324.24	2.340710	2.339454	1.534702	1.533434
	HV	1296.79	1872.78	0.032238	0.057177	0.042565	0.059580
Fault location		DSV					
		CBD		RMS		IED	
		Min	Max	Min	Max	Min	Max
10 kVA	HV/Top	7.83	16.13	0.863410	0.863081	0.001631	0.004133
	HV/Middle	20.30	27.64	0.862852	0.862438	0.005696	0.008311
	HV/Bottom	29.78	38.15	0.862181	0.861758	0.009898	0.014516
40 MVA	HV/Top	13.37	29.06	1.538193	1.537999	0.003231	0.004326
	HV/Middle	33.82	53.09	1.537820	1.537635	0.005492	0.007080
	HV/Bottom	63.86	81.73	1.537483	1.537298	0.008360	0.009920

Table 6-77 Threshold levels for minor forced and free radial buckling faults levels (1% to 5%) in 10 kVA and 40 MVA transformers

Fault location		Radial buckling					
		CBD		RMS		IED	
		Min	Max	Min	Max	Min	Max
10 kVA	LV	222.80	617.47	1.092663	1.103955	0.014615	0.026640
	HV/Top	175.35	206.69	0.867664	0.868265	0.024130	0.025718
	HV/Middle	230.42	252.87	0.869144	0.869756	0.032377	0.034196
	HV/Bottom	269.26	305.45	0.870091	0.870692	0.046231	0.048521
40 MVA	LV	1820.93	1887.86	2.416197	2.418698	0.355873	0.369640
	HV/Top	941.84	1004.69	1.572150	1.580303	0.281049	0.320055
	HV/Middle	1051.39	1129.60	1.582195	1.592824	0.331635	0.380253
	HV/Bottom	1171.30	1246.95	1.595576	1.603986	0.391897	0.434006

Table 6-78 Threshold levels for minor insulation faults levels (1% to 5%) in 10 kVA and 40 MVA transformers

Fault location		Non-mechanical faults on HV winding					
		CBD		RMS		IED	
		Min	Max	Min	Max	Min	Max
10 kVA	Bushing faults	7.95	20.49	0.938078	0.938471	0.506414	0.511150
	Mineral oil	412.95	431.24	0.943418	0.943887	0.542963	0.547528
	Vegetable oil	558.34	578.99	0.967716	0.967923	0.105856	0.110880
40 MVA	Bushing faults	41.42	55.17	1.574975	1.575683	0.207094	0.210971
	Mineral oil	778.26	797.19	1.657792	1.658020	0.562476	0.564928
	Vegetable oil	856.26	872.61	1.779009	1.779154	0.182957	0.186443

Chapter 7 Conclusions and Future Works

7:1 Summary

This thesis presents a new, automated and cost effective approach for detecting mechanical and non-mechanical faults within the power transformer. This proposed approach is based on Digital Image Processing (DIP) techniques that are applied to a simulated power transformer’s FRA signature. As previously discussed, current FRA practice relies predominantly on the measured FRA signature’s magnitude plot with little to no attention given to the phase angle plot. The new proposed signature, however, uses a commercial response analyser to integrate the magnitude and phase angle plots into one polar plot.

7:2 Main Conclusions

The key conclusions drawn from this thesis are summarised below:

- Finite element analysis is an effective software tool for simulation of the real operation of the power transformer. It can also be used effectively to simulate the impacts of real faults on the FRA signatures of transformer windings, which are extremely hard to stage on real operating transformers
- Variation in the FRA signature is not always attributed to mechanical deformations within the transformer. Both simulation and practical results show that the signature is also impacted by non-mechanical faults, such as transformer oil degradation and bushing faults, in particular in the high frequency range.
- The main drawbacks of current FRA practice are its requirement to be used offline and its inability to detect minor fault levels. Also, because an acceptable interpretation code for fault identification and quantification is not yet available, it can lead to inconsistent interpretation of the same FRA signature.
- To date, there is no real application taking advantage of the rapid advancement in DIP technology to automate, enhance and standardise the interpretation process of the FRA signature. The results presented in this thesis demonstrate a step towards that goal.
- The key motivation behind the proposed polar plot, as a new FRA fingerprint for power transformers, is to facilitate the application of DIP and, by integrating all measured features in one plot, increase detection accuracy.
- Both the simulated and practical results of the proposed approach show its ability to detect minor fault levels. Fault type and location can be identified by extracting certain DIP features from the proposed polar plot. These features include geometric features, invariant moment and texture analysis, which are then used to calculate three unique classification metrics: CBD, RMS and IED. The trend of these metrics is found to systematically increase or decrease, depending on the fault type, level, and location.

- Results show that short circuit turn faults at minor levels lead to a slight increase in the area and perimeter features of the geometric dimension values, and the calculated CBD metric increases along with the increase in fault level. On the other hand, the invariant moment and texture analysis features show no consistent trend; some features increase, some features decrease, and two features are maintained at zero values. The RMS and IED metrics also increase along with the increase in fault level. As the fault moves toward the bottom of the winding, the three DIP metrics of short circuit turn faults increase without any overlapping between the proposed maximum and minimum threshold limits.
- In contrast to short circuit turn faults, radial buckling faults at minor levels lead to a slight decrease in all geometric features along with the increase in fault level. The calculated CBD, however, increases along with the increase in fault level. Similar to the SC case, there is no consistent trend in the other 11 features. The increase in fault level leads to an increase in the calculated RMS and IED metrics. When a radial buckling fault moves toward the bottom of the windings, the values of CBD, RMS and IED increase.
- When the level of an axial displacement and disk space variation fault increases, there is also an increase in the four geometric dimension features. The calculated CBD also increases along with the increase in fault level. The RMS metric decreases, while the IED metric increases, along with the increase in fault level. The same trend is observed in the DSV fault except with less magnitude than in the AD fault. When the DSV fault moves toward the bottom of the windings, the RMS decreases while the CBD and IED increase.
- In the case of transformer oil degradation and bushing faults, there is an increase in the 15 features of the geometric dimension, invariant moment and texture analysis techniques when the insulation dialectic properties increase. The three DIP metrics increase along with the increase in fault level. In the case of oil degradation, the extracted features are higher than the corresponding features of a bushing failure. Vegetable oil degradation shows

the highest extracted features using geometric dimension and invariant moment analyses. In the case of bushing failure, the four texture features are found to be the highest, followed by the mineral oil degradation features, then the vegetable oil degradation features.

- The transformer’s rating and physical dimensions lead to the same trend as in the proposed classification metrics at different magnitudes.
- Implementation of the proposed DIP application is readily achievable using any commercial FRA analyser and will improve the performance of the apparatus by automating and standardising the power transformer’s interpretation process.

7:3 Future Works

The proposed DIP application in this thesis can be extended for future study as follows:

- To improve the performance of other CMD techniques, such as partial discharge detection, taking advantage of the rapid advancement in DIP application and based on the research work presented in this thesis.
- To implement a new online technique for detecting mechanical deformation within operating transformers without causing interruption to the electricity chain.
- To extend the application for the FRA technique to detect mechanical faults within rotating machines (such as doubly fed induction generator broken bars), misalignment, eccentricity, drivetrain stresses, broken teeth, or contaminated lubricant oil within the gear box.
- To adopt more classification features to improve the accuracy of the developed DIP technique.
- To build the developed technique within a commercial response analyser and test it on operating transformers.

LIST OF REFERENCES

[1] A. Abu-Siada and S. Islam, "A novel online technique to detect power transformer winding faults," *Power Delivery, IEEE Transactions on,* vol. 27, pp. 849-857, 2012.

[2] A. Jahromi, R. Piercy, S. Cress, J. Service, and W. Fan, "An approach to power transformer asset management using health index," *IEEE Electrical Insulation Magazine,* vol. 25, pp. 20-34, 2009.

[3] R. Smeets, L. Paske, P. Leufkens, and T. Fogelberg, "Thirteen years test experience with short-circuit withstand capability of large power transformers," in *6th Southern Africa Regional Conf. CIGRÉ, Cape Town, South Africa, Paper,* 2009.

[4] T. Fogelberg, "Surviving a short-circuit," *ABB Review,* pp. 24-28, 2008.

[5] M. Tsuchie, M. Kozako, M. Hikita, and E. Sasaki, "Modeling of early stage partial discharge and overheating degradation of paper-oil insulation," *IEEE Transactions on Dielectrics and Electrical Insulation,* vol. 21, pp. 1342-1349, 2014.

[6] A. Bakshi and S. V. Kulkarni, "Eigenvalue Analysis for Investigation of Tilting of Transformer Winding Conductors Under Axial Short-Circuit Forces," *IEEE Transactions on Power Delivery,* vol. 26, pp. 2505-2512, 2011.

[7] Bi, Y. en, F. Aras, and H. Kirkici, "Lifetime estimation and monitoring of power transformer considering annual load factors," *Dielectrics and Electrical Insulation, IEEE Transactions on,* vol. 21, pp. 1360-1367, 2014.

[8] A. Abu-Siada, N. Hashemnia, S. Islam, and M. A. S. Masoum, "Understanding power transformer frequency response analysis signatures," *Electrical Insulation Magazine, IEEE,* vol. 29, pp. 48-56, 2013.

[9] E. P. Dick and C. C. Erven, "Transformer Diagnostic Testing by Frequuency Response Analysis," *IEEE Transactions on Power Apparatus and Systems,* vol. PAS-97, pp. 2144-2153, 1978.

[10] N. D. R. B. Rohitkumar, "Mechanical Condition Diagnosis of Power Transformer by FRA using AI Technique," *IJSRD,* vol. 3, p. 5, 2015.

[11] D. A. K. Pham, T. M. T. Pham, H. Borsi, and E. Gockenbach, "A new method for purposes of failure diagnostics and FRA interpretation applicable to power transformers," *Dielectrics and Electrical Insulation, IEEE Transactions on,* vol. 20, pp. 2026-2034, 2013.

[12] J. L. P. Picher, T. Noonan, and J. Christian, "Mechanical condition assessment of transformer windings using frequency response analysis," CIGER, Patrick Picher, CanadaApr. 2008.

[13] K. Gawrylczyk and S. Banaszak, "Modeling of frequency response of transformer winding with axial deformations," *Archives of Electrical Engineering,* vol. 63, pp. 5-17, 2014.

[14] S. Liu, Y. Liu, H. Li, and F. Lin, "Diagnosis of transformer winding faults based on FEM simulation and on-site experiments," *IEEE Transactions on Dielectrics and Electrical Insulation,* vol. 23, pp. 3752-3760, 2016.

[15] Z. W. Zhang, W. H. Tang, T. Y. Ji, and Q. H. Wu, "Finite-Element Modeling for Analysis of Radial Deformations Within Transformer Windings," *IEEE Transactions on Power Delivery,* vol. 29, pp. 2297-2305, 2014.

[16] S. Maulik and L. Satish, "Localization and estimation of severity of a discrete and localized mechanical damage in transformer windings: Analytical approach," *IEEE Transactions on Dielectrics and Electrical Insulation,* vol. 23, pp. 1266-1274, 2016.

[17] E. Rahimpour, M. Jabbari, and S. Tenbohlen, "Mathematical Comparison Methods to Assess Transfer Functions of Transformers to Detect Different Types of Mechanical Faults," *IEEE Transactions on Power Delivery,* vol. 25, pp. 2544-2555, 2010.

[18] J. A. S. B. Jayasinghe, Z. d. Wang, P. N. Jarman, and A. W. Darwin, "Winding movement in power transformers: a comparison of FRA measurement connection methods," *IEEE Transactions on Dielectrics and Electrical Insulation,* vol. 13, pp. 1342-1349, 2006.

[19] J. Singh, Y. R. Sood, and R. K. Jarial, "Condition Monitoring of Power Transformers - Bibliography Survey," *IEEE Electrical Insulation Magazine,* vol. 24, pp. 11-25, 2008.

[20] D. A. K. Pham and E. Gockenbach, "Analysis of physical transformer circuits for frequency response interpretation and mechanical failure diagnosis," *IEEE Transactions on Dielectrics and Electrical Insulation,* vol. 23, pp. 1491-1499, 2016.

[21] D. A. K. Pham, T. M. T. Pham, H. Borsi, and E. Gockenbach, "A new diagnostic method to support standard frequency response analysis assessments for diagnostics of transformer winding mechanical failures," *IEEE Electrical Insulation Magazine,* vol. 30, pp. 34-41, 2014.

[22] M. Bagheri, B. T. Phung, and T. Blackburn, "Influence of temperature and moisture content on frequency response analysis of transformer winding," *IEEE Transactions on Dielectrics and Electrical Insulation,* vol. 21, pp. 1393-1404, 2014.

[23] N. Hashemnia, A. Abu-Siada, and S. Islam, "Detection of power transformer bushing faults and oil degradation using frequency response analysis," *IEEE Transactions on Dielectrics and Electrical Insulation,* vol. 23, pp. 222-229, 2016.

[24] M. F. M. Yousof, C. Ekanayake, and T. K. Saha, "Examining the ageing of transformer insulation using FRA and FDS techniques," *IEEE Transactions on Dielectrics and Electrical Insulation,* vol. 22, pp. 1258-1265, 2015.

[25] M. Faifer, R. Ottoboni, L. Cristaldi, and S. Toscani, "On-line analysis of power transformer bushings," in *Instrumentation and Measurement Technology Conference (I2MTC), 2011 IEEE*, 2011, pp. 1-6.

[26] A. K. Mehta, R. N. Sharma, S. Chauhan, and S. D. Agnihotri, "Study and diagnosis of the power transformer bushing insulation system," in *2011 IEEE Pulsed Power Conference,* 2011, pp. 700-705.

[27] G. C. P. B. S. M. Gubanski, V. Der Houhanessian, J. Filippini, P., U. G. Guuinic, V. Karius, J. Lapworth, G. Urbani, P. Werelius and, and W. Zaengl,

"Dielectric Response Methods for Diagnostics of PowerTransformers," *Paris: CIGRE Technical Brochure,* vol. 254, 2004.

[28] Pinterst, "Power transformer parts," *Electrical Engineering Books,* 2016.

[29] T. S. JAGERS J, "Different approaches for the acquisition of reliability statistics," *6th Southern Africa Regiona,* 2009.

[30] S. Wang, H. Zhang, S. Wang, H. Li, and D. Yuan, "Cumulative deformation analysis for transformer winding under short-circuit fault using magnetic structural coupling model," *IEEE Transactions on Applied Superconductivity,* vol. 26, pp. 0-5, 2016.

[31] B. P. E. William H. , "Analysis of Transformer Failures," *The Hartford Steam Boiler Inspection & Insurance Co.,* p. 12, 2003.

[32] H. M. Wilhelm, C. C. Santos, and G. B. Stocco, "Dissolved gas analysis (DGA) of natural ester insulating fluids with different chemical compositions," *IEEE Transactions on Dielectrics and Electrical Insulation,* vol. 21, pp. 1071-1078, 2014.

[33] A. Abu-Siada, S. Hmood, and S. Islam, "A new fuzzy logic approach for consistent interpretation of dissolved gas-in-oil analysis," *IEEE Transactions on Dielectrics and Electrical Insulation,* vol. 20, pp. 2343-2349, 2013.

[34] A. Abu-Siada and S. Islam, "A new approach to identify power transformer criticality and asset management decision based on dissolved gas-in-oil analysis," *Dielectrics and Electrical Insulation, IEEE Transactions on,* vol. 19, pp. 1007-1012, 2012.

[35] H. Malik and S. Mishra, "Application of Gene Expression Programming (GEP) in Power Transformers Fault Diagnosis Using DGA," *IEEE Transactions on Industry Applications,* vol. 52, pp. 4556-4565, 2016.

[36] E. Rivas, J. C. Burgos, and J. C. Garcia-Prada, "Vibration Analysis Using Envelope Wavelet for Detecting Faults in the OLTC Tap Selector," *IEEE Transactions on Power Delivery,* vol. 25, pp. 1629-1636, 2010.

[37] K. Hong, H. Huang, and J. Zhou, "Winding Condition Assessment of Power Transformers Based on Vibration Correlation," *IEEE Transactions on Power Delivery,* vol. 30, pp. 1735-1742, 2015.

[38] S. Ji, Y. Luo, and Y. Li, "Research on extraction technique of transformer core fundamental frequency vibration based on OLCM," *IEEE Transactions on Power Delivery,* vol. 21, pp. 1981-1988, 2006.

[39] B. Garcia, J. C. Burgos, and A. M. Alonso, "Transformer tank vibration modeling as a method of detecting winding deformations-part I: theoretical foundation," *IEEE Transactions on Power Delivery,* vol. 21, pp. 157-163, 2006.

[40] E. Gulski, H. P. Burger, G. H. Vaillancourt, and R. Brooks, "PD pattern analysis during induced test of large power transformers," *IEEE Transactions on Dielectrics and Electrical Insulation,* vol. 7, pp. 95-101, 2000.

[41] J. Bolhuis, E. Gulski, and J. Smit, "Monitoring and diagnostic of transformer solid insulation," *IEEE Transactions on Power Delivery,* vol. 17, pp. 528-536, 2002.

[42] W. Mang-Hui, "Partial discharge pattern recognition of current transformers using an ENN," *IEEE Transactions on Power Delivery,* vol. 20, pp. 1984-1990, 2005.

[43] A. Cavallini, G. C. Montanari, F. Puletti, and A. Contin, "A new methodology for the identification of PD in electrical apparatus: properties and applications," *IEEE Transactions on Dielectrics and Electrical Insulation,* vol. 12, pp. 203-215, 2005.

[44] A. Cavallini, M. Conti, A. Contin, and G. C. Montanari, "Advanced PD inference in on-field measurements. II. Identification of defects in solid insulation systems," *IEEE Transactions on Dielectrics and Electrical Insulation,* vol. 10, pp. 528-538, 2003.

[45] R. Bartnikas, "Partial discharges. Their mechanism, detection and measurement," *IEEE Transactions on Dielectrics and Electrical Insulation,* vol. 9, pp. 763-808, 2002.

[46] P. Sun, W. Sima, M. Yang, and J. Wu, "Influence of thermal aging on the breakdown characteristics of transformer oil impregnated paper," *IEEE Transactions on Dielectrics and Electrical Insulation,* vol. 23, pp. 3373-3381, 2016.

[47] M. K. Pradhan and T. S. Ramu, "Estimation of the hottest spot temperature (HST) in power transformers considering thermal inhomogeniety of the windings," *IEEE Transactions on Power Delivery,* vol. 19, pp. 1704-1712, 2004.

[48] M. K. Pradhan and T. S. Ramu, "Prediction of hottest spot temperature (HST) in power and station transformers," *IEEE Transactions on Power Delivery,* vol. 18, pp. 1275-1283, 2003.

[49] Y. Cui, H. Ma, T. Saha, C. Ekanayake, and D. Martin, "Moisture-Dependent Thermal Modelling of Power Transformer," *IEEE Transactions on Power Delivery,* vol. 31, pp. 2140-2150, 2016.

[50] O. A. Amoda, D. J. Tylavsky, G. A. McCulla, and W. A. Knuth, "Acceptability of Three Transformer Hottest-Spot Temperature Models," *IEEE Transactions on Power Delivery,* vol. 27, pp. 13-22, 2012.

[51] N. L. Harrison, "Resistivity of transformer oil at low and medium field strengths," *Electrical Engineers, Proceedings of the Institution of,* vol. 115, pp. 736-741, 1968.

[52] J. S. Forrest, "An electrical resistance test for insulating oils," *Electrical Engineers - Part II: Power Engineering, Journal of the Institution of,* vol. 95, pp. 337-342, 1948.

[53] C. T. Forc, "Dielectric response methods for diagnostics of power transformers," *IEEE Electrical Insulation Magazine*, vol. 19, pp. 12-18, 2003.

[54] A. Betie, F. Meghnefi, I. Fofana, Z. Yeo, and H. Ezzaidi, "Neural network approach to separate aging and moisture from the dielectric response of oil impregnated paper insulation," *IEEE Transactions on Dielectrics and Electrical Insulation,* vol. 22, pp. 2176-2184, 2015.

[55] W. S. Zaengl, "Applications of dielectric spectroscopy in time and frequency domain for HV power equipment," *IEEE Electrical Insulation Magazine,* vol. 19, pp. 9-22, 2003.

[56] A. Setayeshmehr, I. Fofana, C. Eichler, A. Akbari, H. Borsi, and E. Gockenbach, "Dielectric spectroscopic measurements on transformer oil-paper insulation under controlled laboratory conditions," *IEEE Transactions on Dielectrics and Electrical Insulation,* vol. 15, pp. 1100-1111, 2008.

[57] M. Bagheri, B. T. Phung, and T. Blackburn, "Transformer frequency response analysis: mathematical and practical approach to interpret mid-frequency oscillations," *IEEE Transactions on Dielectrics and Electrical Insulation,* vol. 20, pp. 1962-1970, 2013.

[58] M. Wang, A. J. Vandermaar, and K. D. Srivastava, "Improved detection of power transformer winding movement by extending the FRA high frequency range," *IEEE Transactions on Power Delivery,* vol. 20, pp. 1930-1938, 2005.

[59] Z. Zhao, C. Yao, N. Hashemnia, and S. Islam, "Determination of nanosecond pulse parameters on transfer function measurement for power transformer winding deformation," *IEEE Transactions on Dielectrics and Electrical Insulation,* vol. 23, pp. 3761-3770, 2016.

[60] M. Bagheri, M. S. Naderi, T. Blackburn, and T. Phung, "Frequency response analysis and short-circuit impedance measurement in detection of winding deformation within power transformers," *IEEE Electrical Insulation Magazine,* vol. 29, pp. 33-40, 2013.

[61] C. Yao, Z. Zhao, Y. Chen, X. Zhao, Z. Li, Y. Wang, *et al.*, "Transformer winding deformation diagnostic system using online high frequency signal injection by capacitive coupling," *IEEE Transactions on Dielectrics and Electrical Insulation,* vol. 21, pp. 1486-1492, 2014.

[62] C. Yao, Z. Zhao, Y. Mi, C. Li, Y. Liao, and G. Qian, "Improved Online Monitoring Method for Transformer Winding Deformations Based on the Lissajous Graphical Analysis of Voltage and Current," *IEEE Transactions on Power Delivery,* vol. 30, pp. 1965-1973, 2015.

[63] Z. Haijun, Y. Bin, X. Weijie, W. Shuhong, W. Guolin, H. Youpeng, *et al.*, "Dynamic deformation analysis of power transformer windings in short-circuit fault by FEM," *Applied Superconductivity, IEEE Transactions on,* vol. 24, pp. 1-4, 2014.

[64] G. Bertagnolli, "The ABB Approach to Short-circuit Duty of Power Transformers," *Zurich, Switzerland: ABB Ltd,* vol. 3rd, 1996.

[65] E. S. T. Lindquis, M. Slivestre, W. Hoffman, "Transportation Issues of Power Transformers," presented at the IEEE TC Metting, San Diego, 2004.

[66] E. B. a. C. Hernandez., "Power Transformer Manufacturer's Experience with Transportation Mishandling," in *7th Annual WEIDMANN Diagnostic Solutions Technical Conference*, New Orleans, LA, USA, 2009.

[67] A. Islam, S. I. Khan, and A. Hoque, "Detection of mechanical deformation in old aged power transformer using cross correlation co-efficient analysis method," *Energy and Power Engineering,* vol. 3, p. 585, 2011.

[68] M. Wang, A. J. Vandermaar, and K. D. Srivastava, "Review of condition assessment of power transformers in service," *IEEE Electrical Insulation Magazine,* vol. 18, pp. 12-25, 2002.

[69] *Transformers: Basic, maintenance, and diagnostics* vol. 45. United States: Hydroelectric Research and Technical Services Group, 2007.

[70] N. Hashemnia, A. Abu-Siada, and S. Islam, "Improved power transformer winding fault detection using FRA diagnostics part 1: axial displacement simulation," *Dielectrics and Electrical Insulation, IEEE Transactions on,* vol. 22, pp. 556-563, 2015.

[71] A. Hyun-Mo, L. Ji-Yeon, K. Joong-Kyoung, O. Yeon-Ho, J. Sang-Yong, and H. Sung-Chin, "Finite-Element Analysis of Short-Circuit Electromagnetic Force in Power Transformer," *Industry Applications, IEEE Transactions on,* vol. 47, pp. 1267-1272, 2011.

[72] G. Bertagnolli, *Short-circuit Duty of Power Transformers*. Zurich, Switzerland: ABB Ltd, 2007.

[73] C. W. T. McLyman, *Transformer and Inductor Design Handbook, Fourth Edition*. New York: Taylor & Francis, 2011.

[74] S. Kulkarni and S. Khaparde, "Transformer Engineering: Design and Practice," vol. 1, ed. New York: Marcel Dekker Inc, 2004.

[75] D. B. J. Foldi, P. Riffon,, "Recent Achievements in Performing Short circuit Withstand Tests on Large Power Transformers in Canada," *CIGRE, Canada,* p. 12, 2000.

[76] N. Hashemnia, A. Abu-Siada, and S. Islam, "Improved power transformer winding fault detection using FRA diagnostics part 2: radial deformation simulation," *Dielectrics and Electrical Insulation, IEEE Transactions on,* vol. 22, pp. 564-570, 2015.

[77] V. M. Montsinger and G. H. Halsey, "Transformer heating under short-circuit conditions," *Electrical Engineering,* vol. 69, pp. 117-117, 1950.

[78] M. Mahvi and V. Behjat, "Localising low-level short-circuit faults on the windings of power transformers based on low-frequency response measurement of the transformer windings," *IET Electric Power Applications,* vol. 9, pp. 533-539, 2015.

[79] E. Rahimpour, J. Christian, K. Feser, and H. Mohseni, "Transfer function method to diagnose axial displacement and radial deformation of transformer windings," *IEEE Transactions on Power Delivery,* vol. 18, pp. 493-505, 2003.

[80] M. Bagheri, M. S. Naderi, T. Blackburn, and T. Phung, "FRA vs. short circuit impedance measurement in detection of mechanical defects within large power transformer," in *2012 IEEE International Symposium on Electrical Insulation*, 2012, pp. 301-305.

[81] J. Christian and K. Feser, "Procedures for detecting winding displacements in power transformers by the transfer function method," *IEEE Transactions on Power Delivery,* vol. 19, pp. 214-220, 2004.

[82] T. Leibfried and K. Feser, "Monitoring of power transformers using the transfer function method," *IEEE Transactions on Power Delivery,* vol. 14, pp. 1333-1341, 1999.

[83] S. D. Mitchell and J. S. Welsh, "Modeling Power Transformers to Support the Interpretation of Frequency-Response Analysis," *IEEE Transactions on Power Delivery,* vol. 26, pp. 2705-2717, 2011.

[84] V. Behjat and M. Mahvi, "Statistical approach for interpretation of power transformers frequency response analysis results," *IET Science, Measurement & Technology,* vol. 9, pp. 367-375, 2015.

[85] S. A. Ryder, "Methods for comparing frequency response analysis measurements," in *Electrical Insulation, 2002. Conference Record of the 2002 IEEE International Symposium on*, 2002, pp. 187-190.

[86] K. Jong-Wook, P. ByungKoo, J. Seung Cheol, K. Sang Woo, and P. PooGyeon, "Fault diagnosis of a power transformer using an improved frequency-response analysis," *IEEE Transactions on Power Delivery,* vol. 20, pp. 169-178, 2005.

[87] V. Behjat, M. Mahvi, and E. Rahimpour, "New statistical approach to interpret power transformer frequency response analysis: non-parametric statistical methods," *IET Science, Measurement & Technology,* vol. 10, pp. 364-369, 2016.

[88] K. P. Badgujar, M. Maoyafikuddin, and S. V. Kulkarni, "Alternative statistical techniques for aiding SFRA diagnostics in transformers," *IET Generation, Transmission & Distribution,* vol. 6, pp. 189-198, 2012.

[89] M. F. M. Yousof, C. Ekanayake, and T. K. Saha, "Frequency response analysis to investigate deformation of transformer winding," *IEEE Transactions on Dielectrics and Electrical Insulation,* vol. 22, pp. 2359-2367, 2015.

[90] IEC, ""Power transformer: Measurement of frequency response," 2012.

[91] M. R. Feyzi and M. Sabahi, "Finite element analyses of short circuit forces in power transformers with asymmetric conditions," in *Industrial Electronics, 2008. ISIE 2008. IEEE International Symposium on*, 2008, pp. 576-581.

[92] J. Faiz, B. M. Ebrahimi, and T. Noori, "Three- and Two-Dimensional Finite-Element Computation of Inrush Current and Short-Circuit Electromagnetic Forces on Windings of a Three-Phase Core-Type Power Transformer," *Magnetics, IEEE Transactions on,* vol. 44, pp. 590-597, 2008.

[93] H. Wang and K. L. Butler, "Finite element analysis of internal winding faults in distribution transformers," *IEEE Transactions on Power Delivery,* vol. 16, pp. 422-428, 2001.

[94] N. Abeywickrama, Y. V. Serdyuk, and S. M. Gubanski, "High-Frequency Modeling of Power Transformers for Use in Frequency Response Analysis (FRA)," *Power Delivery, IEEE Transactions on,* vol. 23, pp. 2042-2049, 2008.

[95] S. Bouissou, F. Piriou, C. Kieny, and G. Tanneau, "Numerical simulation of a power transformer using 3D finite element method coupled to circuit equation," *IEEE Transactions on Magnetics*, vol. 30, pp. 3224-3227, 1994.

[96] M. R. Barzegaran, M. Mirzaie, and A. S. Akmal, "Investigating short-circuit in power transformer winding with quasi-static finite element analysis and circuit-based model," in *Transmission and Distribution Conference and Exposition, 2010 IEEE PES*, 2010, pp. 1-8.

[97] A. Hyun-Mo, O. Yeon-Ho, K. Joong-Kyoung, S. Jae-Sung, and H. Sung-Chin, "Experimental Verification and Finite Element Analysis of Short-

Circuit Electromagnetic Force for Dry-Type Transformer," *Magnetics, IEEE Transactions on,* vol. 48, pp. 819-822, 2012.

[98] M. Ş. VIHACENCU, A. CIURIUC, and L. Marius, "Experimental Study of Electrical Properties of Mineral and Vegetable Transformer Oils," in *International Conference on Innovation and Engineering Research*, 2013, pp. 2-4.

[99] Y. Bertrand and L. Hoang, "Vegetable Oils As Substitute For Mineral Insulating Oils In Medium-Voltage Equipment," CIGRE, France2007.

[100] T. Judendorfer, A. Pirker, and M. Muhr, "Conductivity measurements of electrical insulating oils," in *Dielectric Liquids (ICDL), 2011 IEEE International Conference on*, 2011, pp. 1-4.

[101] A. Ciuriuc, M. S. Vihacencu, L. M. Dumitran, and P. V. Notingher, "Comparative study on power transformers vegetable and mineral oil ageing," in *Applied and Theoretical Electricity (ICATE), 2012 International Conference on*, 2012, pp. 1-6.

[102] C. T. Dervos, C. D. Paraskevas, P. D. Skafidas, and P. Vassiliou, "A complex permittivity based sensor for the electrical characterization of high-voltage transformer oils," *Sensors,* vol. 5, pp. 302-316, 2005.

[103] K. Bandara, C. Ekanayake, and T. K. Saha, "Modelling the dielectric response measurements of transformer oil," *IEEE Transactions on Dielectrics and Electrical Insulation,* vol. 22, pp. 1283-1291, 2015.

[104] C. Ekanayake, S. M. Gubanski, A. Graczkowski, and K. Walczak, "Frequency response of oil impregnated pressboard and paper samples for estimating moisture in transformer insulation," *IEEE Transactions on Power Delivery,* vol. 21, pp. 1309-1317, 2006.

[105] A. Mikulecky, "Influence of temperature, moisture content and ageing on oil impregnated paper bushings insulation," *Dielectrics and Electrical Insulation, IEEE Transactions on,* vol. 20, pp. 1421-1427, 2013.

[106] L. Cristaldi, M. Faifer, C. Laurano, R. Ottoboni, and S. Toscani, "Monitoring of power transformer bushings in high voltage substations," in *Applied Measurements for Power Systems (AMPS), 2015 IEEE International Workshop on*, 2015, pp. 72-77.

[107] C. R. Paul, *Analysis of multiconductor transmission lines*: John Wiley & Sons, 2008.

[108] S. M. H. Hosseini and P. R. Baravati, "Transformer Winding Modeling based on Multi-Conductor Transmission Line Model for Partial Discharge Study," *Journal of Electrical Engineering and Technology,* vol. 9, pp. 154-161, 2014.

[109] M. Popov, L. v. d. Sluis, R. P. P. Smeets, and J. L. Roldan, "Analysis of Very Fast Transients in Layer-Type Transformer Windings," *IEEE Transactions on Power Delivery,* vol. 22, pp. 238-247, 2007.

[110] T. Y. Ji, W. H. Tang, and Q. H. Wu, "Frequency response analysis of power transformer winding deformation based on a hybrid model," in *Power Engineering and Automation Conference (PEAM), 2011 IEEE,* 2011, pp. 144-147.

[111] A. Shintemirov, W. H. Tang, and Q. H. Wu, "A Hybrid Winding Model of Disc-Type Power Transformers for Frequency Response Analysis," *IEEE Transactions on Power Delivery,* vol. 24, pp. 730-739, 2009.

[112] E. Rahimpour and S. Tenbohlen, "Experimental and theoretical investigation of disc space variation in real high-voltage windings using transfer function method," *Electric Power Applications, IET,* vol. 4, pp. 451-461, 2010.

[113] B. Kuo and F. Golnaraghi, *Automatic control systems*, 8th ed.. ed. New York: John Wiley & Sons, 2003.

[114] G. I. Redford and R. M. Clegg, "Polar plot representation for frequency-domain analysis of fluorescence lifetimes," *Journal of fluorescence,* vol. 15, pp. 805-815, 2005.

[115] T. Andresen, "A logarithmic-amplitude polar diagram," 2001.

[116] G. Thomas, D. Flores-Tapia, and S. Pistorius, "Histogram Specification: A Fast and Flexible Method to Process Digital Images," *IEEE Transactions on Instrumentation and Measurement,* vol. 60, pp. 1565-1578, 2011.

[117] R. E. W. Rafael C. Gonzalez, *Digital image processing*. Upper Saddle River, N.J.: Prentice Hall, 2008.

[118] Z. Guangwen, Y. Lei, and Z. Fan, "An integrated color and texture feature extraction algorithm," in *Computer Science and Network Technology (ICCSNT), 2012 2nd International Conference on*, 2012, pp. 733-737.

[119] R. C. G. Steven L. Eddins, Richard E. Woods, *Digital Image processing using MATLAB* 2nd ed.. ed.: [S.I.] : Gatesmark Pub., 2009.

[120] C. Liang-Wei and L. Chao-Rong, "Invariant moment features for fingerprint recognition," in *Wavelet Active Media Technology and Information Processing (ICCWAMTIP), 2013 10th International Computer Conference on*, 2013, pp. 91-94.

[121] P. Li, D. J. Lilja, W. Qian, K. Bazargan, and M. D. Riedel, "Computation on Stochastic Bit Streams Digital Image Processing Case Studies," *IEEE Transactions on Very Large Scale Integration (VLSI) Systems,* vol. 22, pp. 449-462, 2014.

[122] J. Canny, "A Computational Approach to Edge Detection," *IEEE Transactions on Pattern Analysis and Machine Intelligence,* vol. PAMI-8, pp. 679-698, 1986.

[123] W. Mokrzycki and M. Samko, "Canny edge detection algorithm modification," in *Computer Vision and Graphics*, ed: Springer, 2012, pp. 533-540.

[124] V. Chandola, A. Banerjee, and V. Kumar, "Anomaly detection: A survey," *ACM computing surveys (CSUR),* vol. 41, p. 15, 2009.

[125] G. A. Baxes, *Digital image processing: principles and applications*: Wiley New York, 1994.

[126] J. C. Russ and R. P. Woods, "The image processing handbook," ed: LWW, 1995.

[127] M. R. Teague, "Image analysis via the general theory of moments," *JOSA,* vol. 70, pp. 920-930, 1980.

[128] H. Ming-Kuei, "Visual pattern recognition by moment invariants," *IRE Transactions on Information Theory,* vol. 8, pp. 179-187, 1962.

[129] D. Guiduo, Z. Xi, C. Aiguo, and L. YueQiang, "An improved Hu moment invariants based classfication method for watermarking algorithm," in *ICINS 2014 - 2014 International Conference on Information and Network Security*, 2014, pp. 205-209.

[130] T. Chang and C.-C. Kuo, "Texture analysis and classification with tree-structured wavelet transform," *IEEE Transactions on image processing,* vol. 2, pp. 429-441, 1993.

[131] M. Sonka, V. Hlavac, and R. Boyle, *Image processing, analysis, and machine vision*: Cengage Learning, 2014.

Appendix

Table A-1 Specifications and dimensions of the 10 kVA power transformer

Parameter	Value
Phase, frequency [Hz]	3, 50
Rated power [kVA], current density [A/mm^2]	10, 1.284
Primary/secondary voltage [KV], current [A]	0.238/11.55, 13.9/0.3
Primary/secondary winding resistance [Ω]	0.194/458.95
Primary/secondary turns [Turn], Length [mm]	140/1134, 435.2/647.5
Core leg, winding height [mm]	90x90, 424.3
Distance of yoke-to-yoke, leg-to-leg [mm]	366, 340
Inner, outer diameter of HV/LV winding [mm]	130/100, 162/110.1

Table A-2 Specifications and dimensions of the 40 MVA power transformer

Parameter	Value
Phase, frequency [Hz]	3, 50
Rated power [MVA], Impedance %	40, 13.79
Primary/secondary voltage[KV],resistance [mΩ]	11/66, 12.07/123.7
Primary/secondary turns [Turn]	200/1200
Height of taps, HV winding, LV winding [mm]	912/834, 1074, 1136
Distance of taps to yoke [mm]	187/226
Distance of HV/LV to upper, lower yoke [mm]	106/75, 86/55
Core cross-section, insulation diameter [mm]	560, 579
Inner diameter of HV/LV winding/ taps [mm]	826/613/1071

Table A-3 Characteristics of insulation system for both transformers

Mineral oil	Value
Dielectric Breakdown [KV]	30/85
Relative Permittivity at 25°C	2.1/2.5
Viscosity at 0°, 40°, 100° C [mm^2.s^{-1}]	<76, 3/16, 2/2.5
Pour, flash, fire point [°C]	-30/-60, 100/170, 110/185
Density at 20°C [kg.m^3]	0.83/0.89
Thermal Conductivity [W.m^{-1}.K^{-1}]	0.11/0.16
Expansion Coefficient [10^{-4}.K^{-1}]	7/9
Electrical Conductivity [S.m^{-1}]	1.5×10^{-10}
Kraft paper	Value
Relative Permittivity at 25°C	4.4
Electrical Conductivity, S.m^{-1}	2.4×10^{-15}

Table A-4 Equivalent circuit parameters for the investigated transformers (Equivalent parameters)

Transformer parameters	10 kVA		40 MVA	
	HV	LV	HV	LV
L_s [µH], R_s [Ω]	40, 1	20, 0.5	10, 1	10.5, 0.25
C_{sh} [pF] G_{sh} [µS]	2.35 6.45	37.27 260.89	393.4 196.7	127.67 63.835
C_o [pF] G_o [µS]	20 140	718 5026	61.192 30.596	115.53 57.765
C_{HL} [pF], G_{HL} [µS]	50, 350		89.283, 44.65	

Table B-1 Samples of transfer function for the 10 kVA transformer’s HV winding

f (Hz)	|TF| (dB)	∠TF (°)
20	-78.89	-89.78
4.5k	-45.58	-02.45
11.8k	-115.14	+60.01
25.5k	-60.03	+05.00
200k	-64.70	-72.02
1000k	-46.95	+89.00

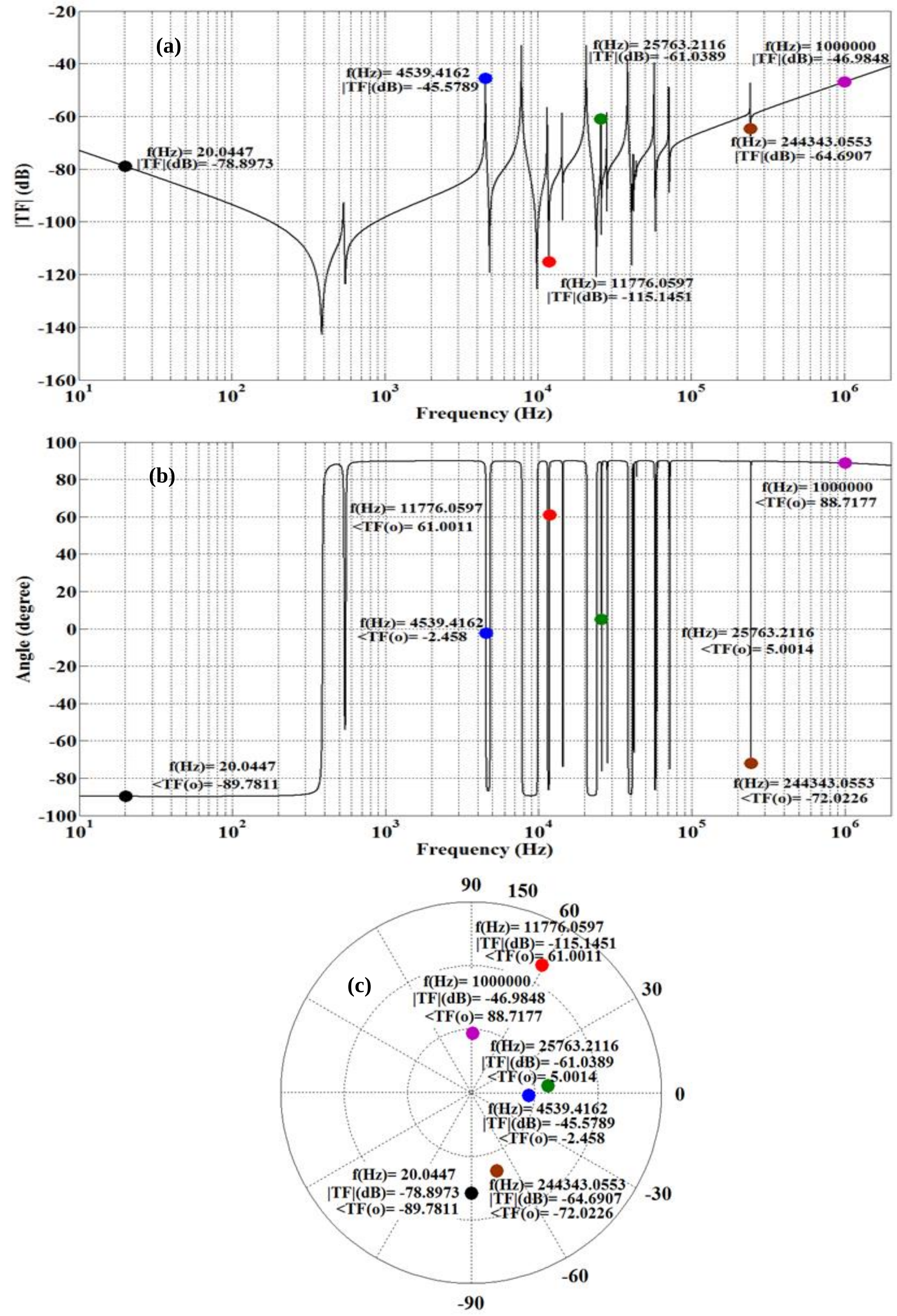

Figure B-1 Sample points of transfer function for the 10 kVA transformer's HV winding (a) magnitude plot, (b) phase angle plot, and (c) polar plot

Table C-1 Geometrical dimensions features equations

Feature	Formula
Area	$g_1 = \sum_{x=0}^{X-1} \sum_{y=0}^{Y-1} a_{FRA_{PP}}(x, y)$ $a_{FRA_{PP}}$: the processed image
Perimeter	$g_2 = \begin{cases} \sum_{x=0}^{X-1} \sum_{y=0}^{Y-1} a_{FRA_{PP}}(x, y) & if\ a_{XorY}(x, y) = 0 \\ 0 & otherwise \end{cases}$
Centroid	$g_3 = \begin{cases} \overline{x} = \frac{1}{A_{FRA\_PP}} \times \sum_{x=0}^{X-1} \sum_{y=0}^{Y-1} x \times a_{FRA_{PP}}(x, y) \\ \overline{y} = \frac{1}{A_{FRA\_PP}} \times \sum_{x=0}^{X-1} \sum_{y=0}^{Y-1} y \times a_{FRA_{PP}}(x, y) \end{cases}$ A_{FRA_PP}: the area (g_1)
Axes length	$g_4 = \begin{cases} Major = x_1 + x_2 \\ Minor = \sqrt{(x_1^2 + x_2^2) - f^2} \end{cases},$ x_{1and2}: The distance from each focus to any point f: The distance between Foci

Table C-2 Seven invariant moment features equations

Feature	Formula
Φ_1	$\eta_{20}+\eta_{02}$
Φ_2	$(\eta_{20}-\eta_{02})^2+4\eta_{11}^2$
Φ_3	$(\eta_{30}-3\eta_{12})^2+(3\eta_{21}-\eta_{03})^2$
Φ_4	$(\eta_{30}+\eta_{12})^2+(\eta_{21}+\eta_{03})^2$
Φ_5	$(\eta_{30}-3\eta_{12})(\eta_{30}+\eta_{12})[(\eta_{30}+\eta_{12})^2-3(\eta_{21}+\eta_{03})^2]+$ $(3\eta_{21}-\eta_{03})(\eta_{21}+\eta_{03})[3(\eta_{30}+\eta_{12})^2-(\eta_{21}+\eta_{03})^2]$
Φ_6	$(\eta_{20}-\eta_{02})[(\eta_{30}+\eta_{12})^2-(\eta_{21}+\eta_{03})^2]+$ $4\eta_{11}(\eta_{30}+\eta_{12})(\eta_{21}+\eta_{03})$
Φ_7	$(3\eta_{21}-\eta_{03})(\eta_{30}+\eta_{12})[(\eta_{30}+\eta_{12})^2-3(\eta_{21}+\eta_{03})^2]-$ $(\eta_{30}-3\eta_{12})(\eta_{21}+\eta_{03})[3(\eta_{30}+\eta_{12})^2-(\eta_{21}+\eta_{03})^2]$

Table C-3 Texture analysis features equations

Feature	Formula
τ_1	$\frac{\sum_{x=0}^{X-1} \sum_{y=0}^{Y-1} (x-\mu_x) \times (y-\mu_y) \times a_{FRA_{PP}}(x,y)}{\sigma_x \sigma_y}$ μ_x *and* μ_y: the means σ_x and σ_y: the standard deviation
τ_2	$\sum_{x=0}^{X-1} \sum_{y=0}^{Y-1} \frac{a_{FRA_{PP}}(x,y)}{1+\lvert x-y \rvert}$ $a_{FRA_{PP}}$: the processed image
τ_3	$\sum_{x=0}^{X-1} \sum_{y=0}^{Y-1} (x-y)^2 \times a_{FRA_{PP}}(x, y)$
τ_4	$\sum_{x=0}^{X-1} \sum_{y=0}^{Y-1} a_{FRA_{PP}}^2 (x, y)$